Stochastic Simulation of Spatial Steel Corrosion for Performance Assessment of Aging RC Structures

劣化RC構造物の性能評価に用いる鉄筋腐食の空間変動シミュレーション

2022/07

Supasit SRIVARANUN
スリヴァラヌン　スパシット

Stochastic Simulation of Spatial Steel Corrosion for Performance Assessment of Aging RC Structures

劣化RC構造物の性能評価に用いる鉄筋腐食の空間変動シミュレーション

2022/07

Waseda University Graduate School of Creative Science and Engineering

Department of Civil and Environmental Engineering, Research on Concrete Structure

Supasit SRIVARANUN
スリヴァラヌン　スパシット

Acknowledgement

Foremost, I would like to express my deep and sincere gratitude to my supervisor, Prof. Mitsuyoshi Akiyama, who supported me in finalizing this research, provided me with the most valuable instructions and gave me countless opportunities to gain priceless experiences. The five-year studying period in Japan is not long, but all given by him will always be carried with me till last.

Besides my supervisor, I would like to thank all my Ph.D. dissertation committee members: Prof. Motoi Iwanami, Prof. Yasuhiko Sato, and Prof. Kiyoshi Ono, for their deliberate comments and suggestions.

I am genuinely grateful to Japan's Ministry of Education, Culture, Sports, Science, and Technology (MEXT), which grants me the scholarship to pursue my master's and my doctorate in the best educational environment at Waseda University.

I was greatly fascinated when collaborating with several professionals from Lehigh University's Advanced Technology for Large Structural Systems (ATLSS) Engineering Research Center to complete this dissertation. First, I would like to express my appreciation to Prof. Dan M. Frangopol, who continually offers valuable comments on academic papers prepared based on this dissertation. Another special acknowledgment should be provided to Dr. Paolo Bocchini and Dr. Vasileios Christou for their constructive commentary and insightful guidance.

My great thanks go to my colleagues who relate most to this research, Hiroyuki Fukushima and Keisuke Masuda, for their profound knowledge and inspirational discussion. It was also my fortune to have tremendous support from other talented colleagues in my research team Mina Shintani, Taiki Yamada, Satoru Nakamura, Zhejun Xu, Ao Li, Zejie Jia and Akane Furuyama. I genuinely respect their practical and

analytical skills.

I would also like to express my profound thanks to other students in Prof. Akiyama's laboratory. First, my deep appreciation goes to former Ph.D. students Dr. Sopokhem Lim, Dr. Zhengshu He, Dr. Mingyang Zhang, Dr. Md. Abul Hasan, Dr. Hiroki Ishibashi, Dr. Jiyu Xin, Dr. Ramiz Ahmed Raju and Dr. Brito Benjamin for their sage guidance and thoughtful discussion. Furthermore, I want to appreciate current Ph.D. students Abdul Kadir Alhamid, Putri Syahidah Firdaus and Koki Aoki, former M.Sc. & Bachelor students Mitsuhiro Matsuda, Soichiro Nishiyama, Kengo Nanami, Hironori Sato, Kekui Yan, Lei Nie, Naoki Nishiya, Ikue Suda, Yumi Kawai, Yoshitaka Ichikawa, Zhang Cheng Zhi, Masanori Fujiwara, Keisuke Kojima, Takayuki Kojima, Hiroki Yamaguchi, Takumi Kageyama, Teresa Nadya Helen Prayogo, Chunliang Zhu, Takumi Ishida, Hiroki Kashiyama and Tatsuya Kakegawa and current M.Sc. & Bachelor students Miki Yajima, Yuzuki Fuse, Yuka Hosono, Chi Chen and Syunya Usui, for creating a warm and energetic studying environment. Also, I would like to thank to the secretary of Prof. Akiyama's laboratory Mizuho Takeuchi for her friendly assistance and the Material Engineering laboratory staff for their technical aid and kind suggestion.

Special thanks go to my partner Nanthaporn Phasuk for her care and encouragement. Last but not least, thank you for the unconditional love from my parents, Pisith Srivaranun and Napa Hemawat, for always supporting me and standing by me over this time.

Supasit Srivaranun

Waseda University, Tokyo

27th May 2022

Abstract

The deterioration of reinforced concrete (RC) structures due to chloride-induced corrosion is not spatially uniform because of the spatial variability related to material properties and environmental stressors. This variation has a substantial effect on the reliability of RC structures. However, few experimental studies have focused on the effect of the interaction of corrosion pits among tensile rebars on the reliability of RC structures. Therefore, in this dissertation, an experimental procedure that incorporates X-ray and digital image processing techniques was conducted on RC slab specimen subjected to accelerated corrosion. Using the experimental results, the parameter of the transverse correlation function of steel weight loss distributions was estimated to investigate how the corrosion pits in corroded rebars are correlated. Based on the experimentally obtained model parameters, the spatial steel weight loss distributions were simulated by spectral representation method. A three-dimensional (3D) nonlinear finite element (FE) analysis of RC structures with simulated steel weight loss distributions was conducted to obtain the ultimate bending capacity of RC structures. In an illustrative case study, the effect of the transverse correlation among steel weight loss distributions of multiple tensile rebars on the failure probability of RC girders was quantified.

Table of Contents

List of Tables

List of Figures

Chapter 1: Introduction

Reinforced concrete (RC) structures located in chloride-laden environments are subjected to corrosion, which causes a reduction in structural capacity and a decrease in their longevity. It is well documented that the cost of structural interventions (e.g., inspection, maintenance, and repair) has increased due to corrosion damage [1, 2]. Consequently, in recent decades, corrosion problems have received a substantial amount of attention from researchers and practitioners [3].

The mechanism of material corrosion in RC structures in an aggressive environment depends strongly on various parameters, such as geometrical and material properties that are associated with the structural systems, mechanical and environmental stressors, and other factors involved in the deterioration processes. All these parameters typically need to be modeled as uncertain. In such circumstances, reliability theory and assessment methods play an essential role in estimating structural safety because they consider these uncertainties [4–10]. Moreover, it has been well recognized that the uncertain parameters associated with geometric and material properties are not uniform in RC structures due to the spatial variability associated with workmanship quality, environmental exposure, and other factors [11]. This lack of uniformity causes local corrosion damage, such as corrosion cracks, concrete cover spalling, and steel corrosion [12]. Furthermore, studies confirmed that spatial variations in steel corrosion within RC structures have detrimental effects on the structural capacity [13–15]. Zhu et al. [13] noted that the cross-sectional area loss of corroded rebars in RC beams is highly related to the reduction in structural performance. Castel et al. [14, 15] indicated that the coupling between the reduction in the steel cross-sectional area and the local steel-concrete bond strength loss due to corrosion cracking has a substantial detrimental impact on the structural performance of

RC members. As a result, disregarding nonuniform corrosion can lead to overestimating of the reliability of RC structures [12, 16, 17]. Therefore, an investigation of the effect of spatial steel corrosion distributions on the reliability of RC structures is important.

To consider the spatial variability of steel corrosion in reliability analyses, some studies have discretized RC members into a series of longitudinal elements and modeled maximum corrosion pit depths for each tensile rebar in each element using Gaussian or non-Gaussian random fields [12, 17–20]. However, few studies have focused on the interaction of corrosion pits among tensile rebars in the transverse direction, which has a substantial effect on the reliability of RC structures. Kioumarsi et al. [21, 22] proposed the use of a modified cross-section for corroded tensile rebars to account for the effect of the possible interaction of localized corrosion among these rebars in the performance assessment of RC beams. However, this adjustment was made based only on an analytical approach using finite element (FE) analysis Therefore, more work is needed to experimentally investigate the influence of the interaction of corrosion pits among tensile rebars on the reliability of RC structures.

The parameter that represents the interaction of corrosion pits among tensile rebars can be experimentally obtained based on the results of steel corrosion distributions in corroded RC members. Recently, Lim et al. [23, 24] applied X-ray and digital image processing techniques to estimate the steel weight loss distributions in corroded RC beams. Their experimental results were acquired from RC beams with a single tensile rebar. Therefore, to capture the effect of the interaction of corrosion pits among multiple rebars (i.e., correlation in the transverse direction), an experimental program must be established to investigate the progression of steel weight loss distributions of RC members with multiple rebars.

This dissertation proposes a procedure for estimating the structural reliability of RC structures considering the effect of the interaction of corrosion pits among tensile rebars.

In particular, **Chapter 2** presents the literature review on the basic knowledge of steel corrosion in concrete, experimental methods for investigating corrosion of embedded rebars, and analytical approaches for determining the structural safety of RC members. The issues highlighted in this chapter have led to the improvement of the structural reliability estimation of corroded RC structures presented in the part of the dissertation. In **Chapter 3**, the experimental program to investigate the effect of the interaction of steel corrosion distributions among tensile rebars in an RC specimen is presented. The spatial steel weight loss distributions of tensile rebars in an RC specimen were monitored and quantified using the X-ray and digital image processing techniques. **Chapter 4** introduces the procedures for the stochastic simulation and structural performance assessment of corroded multiple rebars RC members. Based on the experimental results of steel weight loss distributions in the RC specimen, the interaction of corrosion pits among tensile rebars can be represented by the parameter associated with the transverse correlation of steel weight loss distributions. Subsequently, this parameter is applied to simulate the spatial steel weight loss distributions in stochastic fields using the spectral representation method (SRM). To study the influence of the (simulated) spatial steel weight loss distributions on the structural performance of corroded RC structures, three-dimensional (3D) nonlinear FE analysis is adopted to evaluate the ultimate load capacity of corroded RC structures under bending. In **Chapter 5**, as an illustrative example, the impact of the transverse correlation among the spatial steel weight loss distributions on the failure probability that is associated with the flexural failure of RC girders subjected to load demand and steel corrosion is discussed. Finally, **Chapter 6** presents the main conclusions of the dissertation and future works.

Chapter 2: Literature Review

2.1 Basic Knowledge on Steel Corrosion in RC Structures

2.1.1 Mechanism of Steel Corrosion

The reinforcing bar in RC structures is protected by a thin passive film that forms on the surface of the rebars due to the alkaline solution contained in the pores of the hydrated cement paste [25]. However, corrosion can occur when this passive film is eliminated or locally damaged. This passivating environment in the concrete can be broken down without attacking the concrete due to a couple of conditions: carbonation and chloride penetration. These are the two major causes of corrosion on reinforcing bars in RC structures. Carbonation can be commonly observed in aging and poorly constructed structures (particularly buildings). It is rare in modern civil engineering structures where water-to-cement ratios are low and cement contents are high with good compaction and curing [19]. Under specific conditions, other causes of corrosion on the reinforcing bars can be detected (e.g., sulfate attack, bacteria, stray current induced corrosion), nevertheless only chloride-induced corrosion is described herein.

Chloride ions can be found in concrete owing to several causes. Sea salt spray, seawater wetting and deicing salts are some of the most frequent sources of chloride penetration into concrete [19]. Chlorides serve as catalysts to steel corrosion and are not consumed in the process but let the corrosion process to progress rapidly. Once an amount of chloride ions exceeds a critical level at the surface of the rebars, the protective layer on the steel breaks down and a localized attack can arise. Chlorides in concrete are also prone to absorb and retain moisture, reducing concrete's electrical resistance and allowing easier transportation of ions.

Corrosion is an electrochemical mechanism consisting of anodic and cathodic half-

cell reactions [19]. At the anode, the iron in the steel is oxidized to form ferrous ions (Fe^{2+}) to the concrete pore solution based on the following half-cell reaction:

$$Fe \rightarrow Fe^{2+} + 2e^{-} \quad (1)$$

The electrons released by the anodic reaction are consumed at the cathodic sites on the steel surface to preserve electrical balance. The cathodic reaction is the oxygen reduction as:

$$O_2 + 2H_2O + 4e^{-} \rightarrow 4\left(OH^{-}\right) \quad (2)$$

Chloride ions can activate the unprotected steel surface and form an anode:

$$Fe^{2+} + 2Cl^{-} \rightarrow FeCl_2 \quad (3)$$

$$FeCl_2 + 2H_2O \rightarrow Fe(OH)_2 + 2HCl \quad (4)$$

Ferrous hydroxide $Fe(OH)_2$ can also be formed according to:

$$Fe^{2+} + 2OH^{-} \rightarrow Fe(OH)_2 \quad (5)$$

and can result in the formation of ferric hydroxide $Fe(OH)_3$:

$$4Fe(OH)_2 + O_2 + 2H_2O \rightarrow 4Fe(OH)_3 \quad (6)$$

and finally hydrated ferric oxide:

$$2Fe(OH)_3 \rightarrow Fe_2O_3 \cdot H_2O + 2H_2O \quad (7)$$

The anodic–cathodic reactions just described are presented in Figure 1. $Fe_2O_3 \cdot H_2O$ in Eq. (7) is the final corrosion product, so-called “red rust”, but the other iron oxides also exist. The corrosion product volume is 2-6 times larger than that of the steel bar [26], as shown in Figure 2. Subsequently, this significant volume expansion of rust causes

internal pressures and leads to cracking and spalling of the concrete surrounding the rebar. Consequently, the chloride ions can easily reach the rebar surface and accelerate the corrosion mechanism. The chloride-induced corrosion of steel bars therefore potentially reduces the serviceability and long-term structural performance of RC structures.

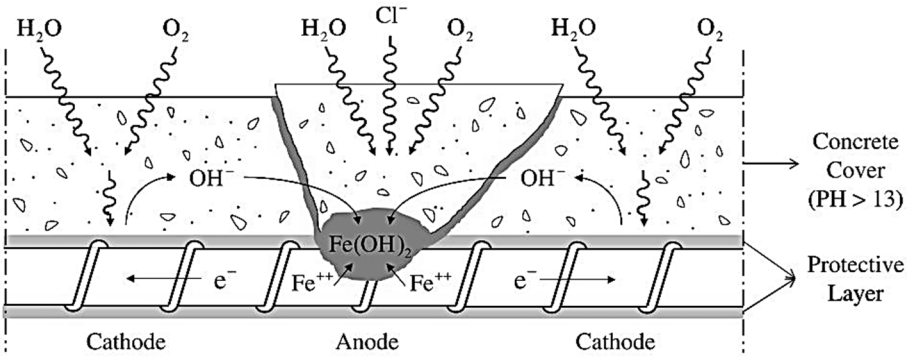

Figure 1 Schematic illustration of a chloride-induced corrosion process in concrete structures [25].

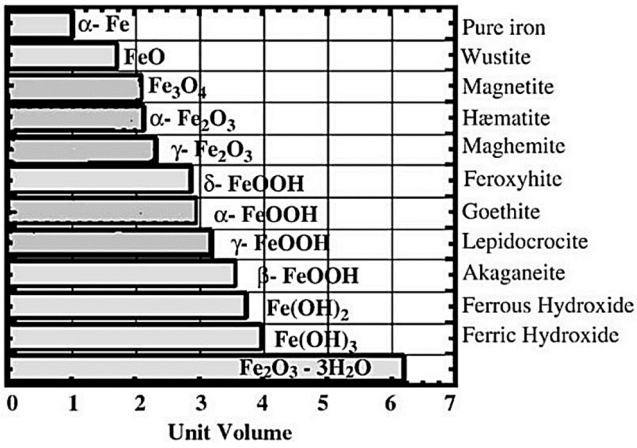

Figure 2 Corrosion products of iron [26].

2.1.2 Influences of Steel Corrosion in the Structural Degradation

Steel corrosion is one of the major causes of the structural degradation of RC structures. In recent decades, a significant number of studies have been dedicated to investigating the influences of reinforcing bar corrosion on the structural performance of RC structures.

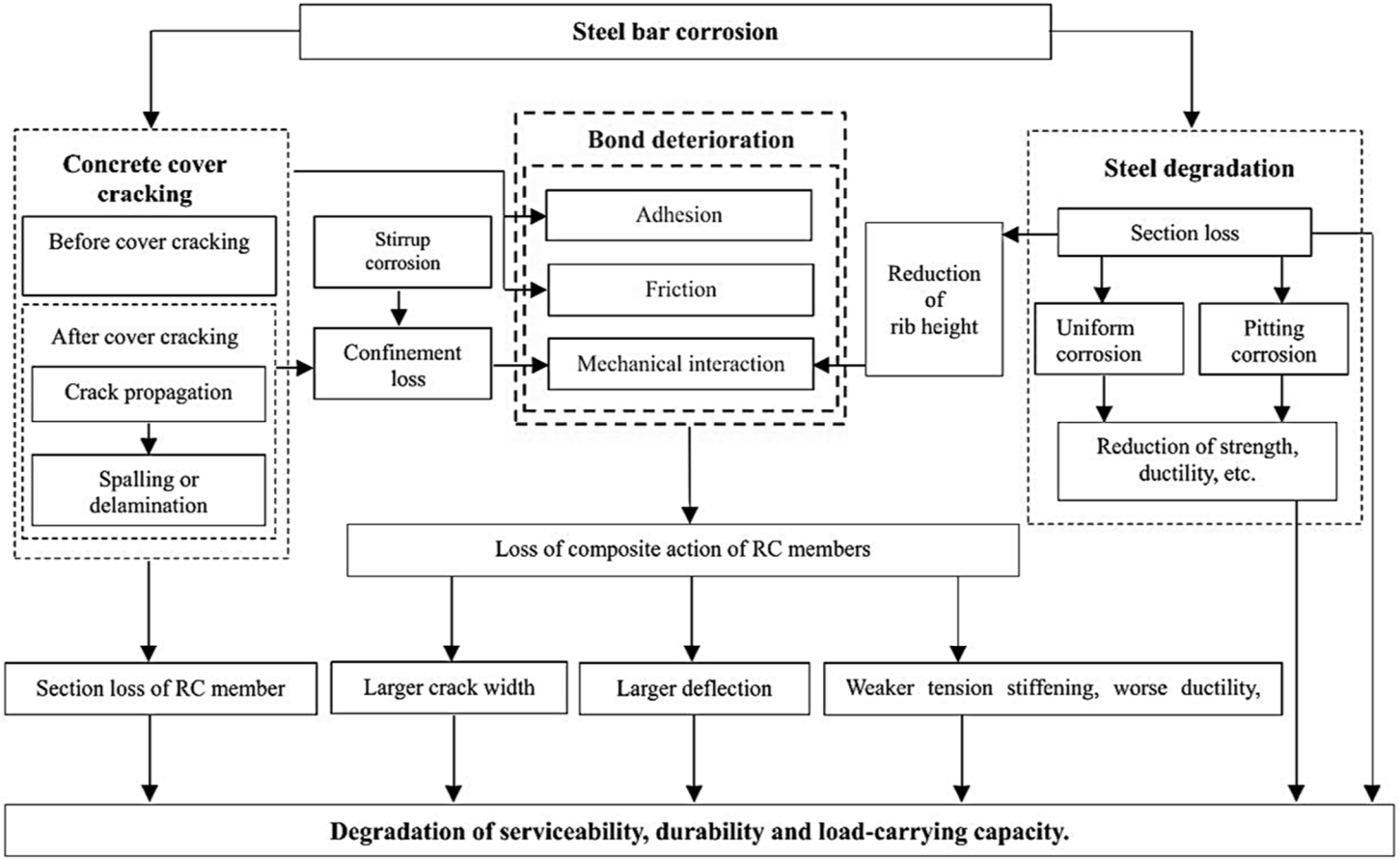

Figure 3 Influence of steel corrosion on the structural performance of RC structures [27].

The major impacts of corrosion on RC structures are: (1) concrete cover cracking, (2) reduction of strength and ductility, (3) deterioration of bonding between concrete and reinforcing bars. The consequences of each of these effects on the degradation of serviceability, durability and load-carrying capacity of RC structures are presented in Figure 3 [27].

Mangat and Elgarf [28] conducted experimental testing of flexural capacity on corroded RC beams. They indicated that loss of rebar cross-section has a significant impact on the residual flexural capacity of beams. An empirical formula was presented to assess the effect of steel corrosion on the residual capacity of corroded RC beams. Torres-Acosta et al. [29] pointed that the flexural strength of corroded RC members is significantly affected by the maximum corrosion pits rather than the average cross-sectional area loss of steel bar. The experiments conducted by Castel et al. [30] showed that a ductility reduction approximately 70% for the beam failed at the mid-span where the maximum corrosion pit occurs. This is attributed to a loss of ductility of the tensile rebar from localized damage due to corrosion. They confirmed that the loss of bonding between concrete and reinforcing rebar has no impact on the load-carrying capacity and the residual capacity can be estimated by using the cross-sectional area loss of the rebar. El Maaddawy et al. [31] conducted experiments to investigate the coupled effects of steel corrosion and sustained load on the structural capacity of RC beams. The experimental results indicated that the beam capacity reduction was relative to the cross-sectional area loss of steel bar induced by corrosion. Zhu and François [13] presented that the ductility loss of corroded RC beam was due to approximately 50% loss of the rebar cross-section at the failure location. The results also showed a 57% reduction in ultimate deflection of the corroded beam.

Kashani et al. [32] provided a comprehensive state-of-the-art review of several experimental studies on the residual capacity of RC beams affected by steel corrosion.

The ratio of residual ultimate flexural capacity (i.e., the ratio of the ultimate flexural capacity of a corroded beam to that of a sound beam) and the ratio of ultimate residual deformation (i.e., the ratio of the ultimate deflection of a corroded beam to that of a sound beam) of the collected beam data were plotted against the percentage of steel weight loss. However, the results showed large-scatter relation.

Lim et al. [22] conducted the four-point bending test on corroded RC beams. They reported that a significant reduction in the flexural strength and deflection of the RC beams was due to the highly localized steel corrosion. The experimental results indicated that as the spatial variability of the steel cross-sectional area loss increases, the effect of the localized corrosion on the load-carrying capacity of RC beam tends to be more substantial than the average steel weight loss. Using the mean steel weight loss to predict the structural deterioration of RC members may not be accurate in some cases since the distribution of steel corrosion was highly non-uniform along the rebar length due to the spatial variability associated with workmanship quality, environmental exposure, and other factors [11].

The corrosion of stirrups can lead to substantial effects on the RC structures. For example, severe corrosion of stirrups can cause detrimental loss of the shear capacity of beams, as well as significant reduction of the ductility and compressive capacity of RC columns. Higgins and Farrow [33] investigated the structural capacity of RC beams with corroded stirrups and found that the corrosion of stirrups resulted in reduced shear capacity and overall deformability at failure. It was also reported that the spacing of stirrup could affect the extent of spalling and cracking of concrete cover due to the expansion of corrosion products. Experimental and numerical investigations on beam-end specimens conducted by Hanjari et al. [34] and Coronelli et al. [35] indicated that for a certain level of corrosion of the longitudinal rebar, the corrosion damage in RC members with corroded stirrups was more severe than that without corroded stirrups. Furthermore,

it was determined that the corrosion of stirrups could reduce the bond strength; nevertheless, significant bond degradation would begin only when the level of stirrup corrosion was high. However, only the effects of corrosion in tensile rebars on the structural performance of RC members were investigated in this dissertation.

2.2 Experimental Methods for Investigating Steel Corrosion in RC Structures

2.2.1 Accelerated Corrosion Methods

Since the process of reinforcement corrosion in concrete structures under natural conditions is prolonged, laboratory studies need to accelerate the corrosion process to achieve a short test period. According to the standard NT Build 492 [36], several accelerated corrosion methods have been commonly used, e.g., impressed current methods, artificial climate environmental methods, and accelerated chloride migration methods. However, the impressed current technique is the most common method used to study rebar corrosion embedded in concrete [37]. Several studies have been conducted using the impressed current method to study the corrosion effects on the cracking of concrete cover [38], bond behavior [39], and the load-bearing capacity of RC members.

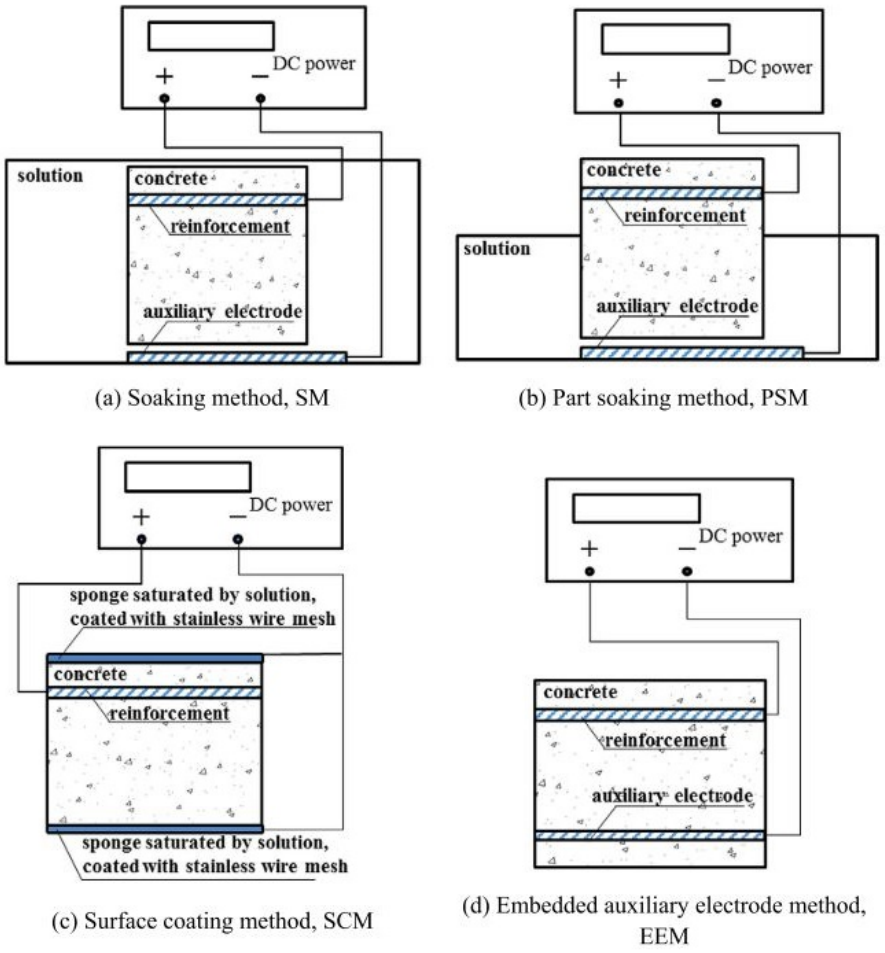

Figure 4 Typical layout of the impressed corrosion techniques [40].

The impressed current technique is performed by supplying a constant current from a direct current (DC) power supply to the reinforcing bars in concrete structures in order to provide a significant corrosion level on the rebars in a short period of time. Figure 4 shows four typical layouts of the impressed current technique [40]. The main differences among the test settings shown in Figure 4 are the position of the counter (or auxiliary) electrode (e.g., external copper plate and stainless-steel plate) and exposure condition of specimens. The embedded steel reinforcement in the concrete that functions as the anode is connected to the positive charge of the DC power supply, while the counter electrode that serves as the cathode is connected to the negative charge of DC power. The current is impressed from the counter electrode to the reinforcing bar embedded in concrete with

the aid of the electrolyte (typically 3% or 5% sodium chloride solution). Anode, cathode and electrolyte constitute a closed circuit. The impressed current is varied on the basis of the surface area of the anode such that a desired constant current density can be achieved.

2.2.2 Spatial Steel Corrosion Measurements

The study of spatial steel corrosion using experimental data obtained from the accelerated-corrosion RC members has become the focus of researchers in recent years [17, 23, 24, 41]. The statistical information of spatial steel corrosion obtained from the experimental tests in the laboratory can be applied together with the observation data from the in-situ structures in order to improve the accuracy for the evaluation of the magnitude and variability of steel corrosion in aging structures and their long-term performance. Therefore, it is essential to develop the measurement methods of non-uniform steel corrosion distributions which facilitates the understanding of how they vary in space and time.

The general approaches applied in the literature to study the non-uniformity of steel corrosion at different corrosion levels are described as follows. Initially, RC specimens are corroded up to the desired steel corrosion amounts at different corrosion levels. After that, the destructive method is generally used by severally breaking RC specimens to obtain samples of corroded rebar in order to measure the geometrical parameters and amount of corrosion of the corroded bar. Various methods, including weighing loss, vernier caliper, drainage method, 3D scanning, have been applied for the measurement [42]. Figure 5 shows a schematic diagram of methods for measuring spatial steel corrosion. Figure 6 illustrates an example of cross-sectional analysis for corroded and uncorroded rebars after 3D scanning.

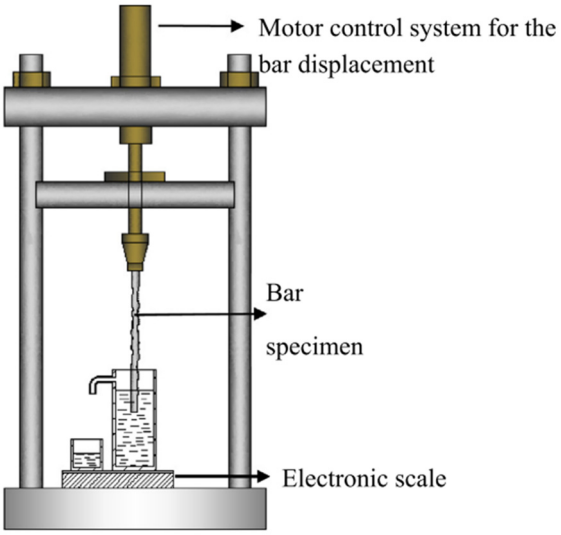

(a) Schematic diagram of drainage method

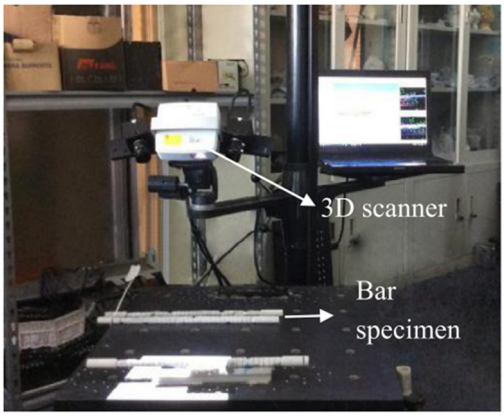

(b) Schematic diagram of 3D scanning method

Figure 5 Schematic diagram of methods for measuring the spatial steel corrosion [42].

However, these methods require certain specimens to be demolished to measure the steel corrosion evolved, and they may be error-prone owing to the difficulty in controlling the same experimental conditions and other uncertainties (e.g., different corrosion cracking patterns and locations of steel corrosion).

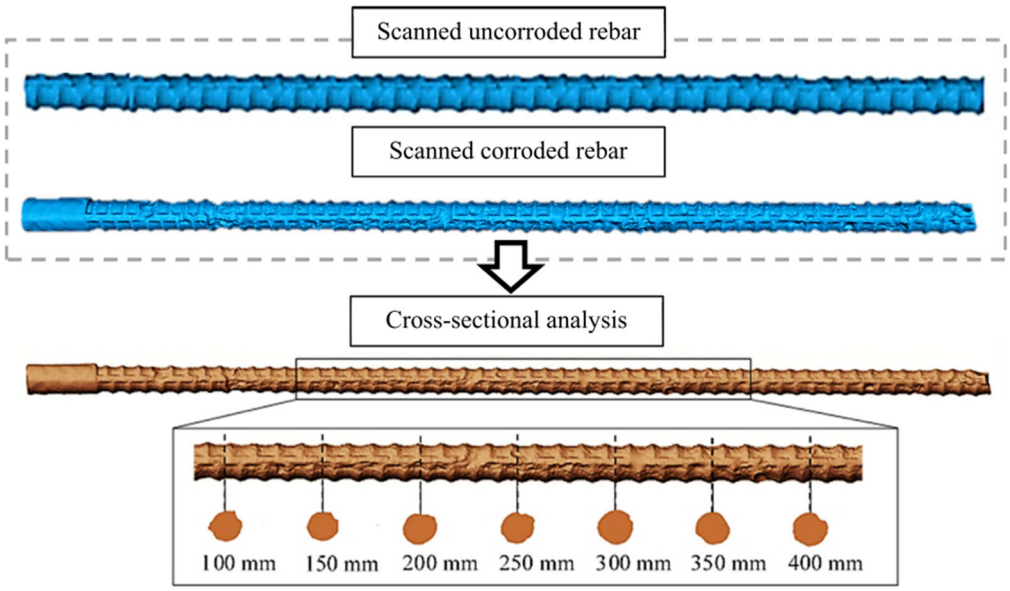

Figure 6 Cross-sectional analysis of corroded and uncorroded rebars after utilizing 3D scanning method [43].

To understand the process of steel corrosion growth and the spatial variability changed with time, continuous monitoring is necessary. Recently, Lim et al. [23, 24] and Zhang et al., [17] applied X-ray and image processing techniques to monitor the steel corrosion in RC specimens. The correlation of non-uniform steel corrosion distribution and crack width distribution along corroded rebar was also observed during the corrosion process. Figures 7(a) and (b) display an example of the X-ray image of a RC specimen and measured steel weight loss distribution of the rebar in a corroded RC specimen, respectively [24].

The experimental results of steel weight loss distribution in Lim et al., [23, 24] and Zhang et al., [17] were obtained from RC beams with a single tensile rebar. Therefore, to understand the effect of the interaction of corrosion pits among multiple rebars by observing its correlation in the transverse direction, an experimental program must be carried to investigate the growth of steel weight loss distributions of RC members with multiple rebars using the X-ray technique.

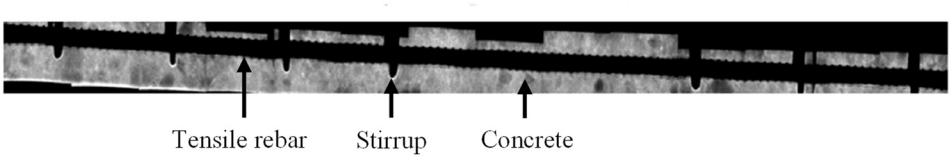

(a) X-ray image along a corroded RC specimen

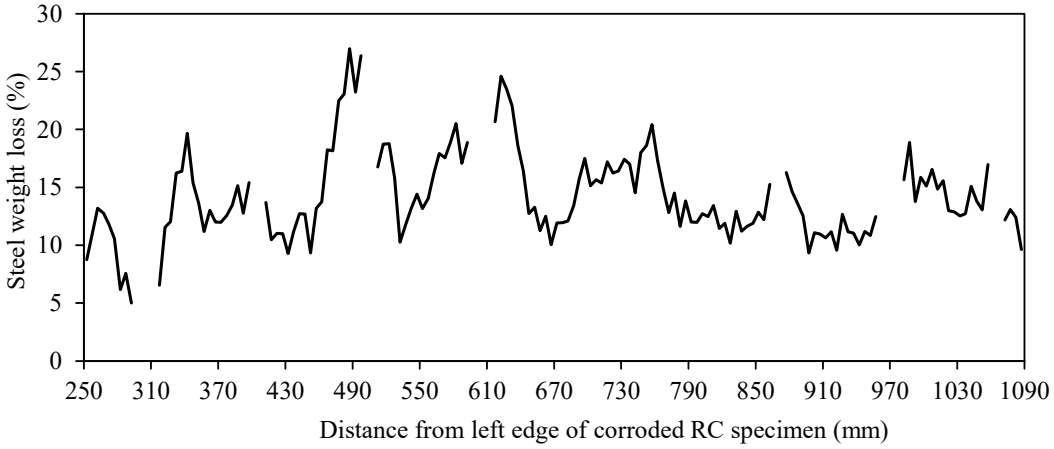

(b) Steel weight loss distribution of a corroded RC specimen

Figure 7 Example of X-ray image and measured steel weight loss distribution of a tensile rebar in corroded RC specimen [24].

2.3 Analytical Approaches for Determining the Structural Safety of Corroded RC Members

2.3.1 Structural Reliability Analysis

The structural degradation of RC structures due to corrosion attack depends strongly on several uncertain factors such as geometrical and material properties that are associated with the structural systems, mechanical and environmental stressors, and other factors involved in the deterioration processes. Therefore, reliability concepts and methods have to be adopted in estimating structural safety because they can reflect these uncertainties [4–10].

Over the past decades, several models for evaluating the reliability of corroded RC members have been proposed by many researchers. Reliability-based service life assessment of corroded concrete girder was established by Mori et al. [44]. The reliability of RC girders under the corrosion attack was proposed by Frangopol et al. [4]. The influences of steel corrosion on both flexural and shear reliabilities of RC bridge T-girder are investigated. The results showed that under the same corrosion rate, the loss of flexural reliability is generally larger than that of shear reliability. Stewart et al. [45] presented the time-dependent reliability of deteriorating reinforced concrete bridge decks. Their study presented the application of de-icing salts and atmospheric exposure in a marine environment to investigate the long-term deterioration of RC bridge desks. Enright et al. [46] proposed a reliability-based condition assessment of deteriorating concrete bridges considering load distribution. Based on the previous studies, the effect of steel corrosion on flexural capacity was assumed as a uniform distribution over the entire structures by using the reduced cross-sectional area of reinforcing bars to estimate the load-carrying capacity. However, this assumption is an oversimplification because steel corrosion and the associated corrosion cracking and spalling of cover concrete are substantially nonhomogeneous in RC structures due to the spatial variability caused by workmanship, environmental stressors and other factors [12, 47]. The inclusion of spatial variability of pitting corrosion can lead to a significant decrease in flexural reliability [12].

Several studies have conducted reliability analyses of corroded RC structures by incorporating the effect of the spatial steel corrosion distribution. These studies simulate the maximum corrosion pit depths along tensile rebars in RC members in the random field context to account for the effect of the spatial steel corrosion distribution. However, few studies have focused on the interaction of corrosion pits among tensile rebars in the transverse direction, which has a substantial effect on the reliability of RC structures. Kioumarsi et al. [21, 22] proposed to modify the total residual cross-section of corroded

tensile rebars in the analytical analysis of the load-carrying capacity in order to consider the effect of the interaction of corrosion pits on the structural reliability. However, this adjustment was made based only on an analytical approach using finite FE analysis. Therefore, more work is required to experimentally investigate the influence of the interaction of corrosion pits among tensile rebars on the reliability of RC structures.

The FE method is currently applied for the probability-based structural performance assessment of corroded RC structures [17, 48, 49]. By randomizing some of the parameters in the FE method, the uncertainties and variations that are ignored in a deterministic analysis can be considered. Therefore, it is essential to incorporate the FE method in the reliability assessment of corroded RC structures considering the spatial variability of steel corrosion.

2.3.2 Stochastic Modeling

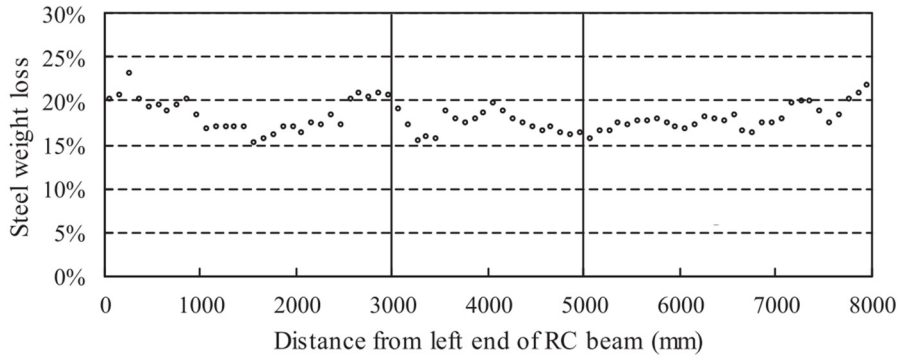

Figure 8 Example of simulated steel weight loss distribution on tensile rebar in a corroded RC beam [17].

To account for the effect of the spatial variability of steel corrosion in the estimation of structural reliability for corroded RC structures, several studies have adopted the random field concept to simulate the corrosion process in a random field context [12, 17, 19, 20, 48, 49]. Specifically, based on statistical information of the spatial steel corrosion obtained from the measurements, a random field of steel corrosion can be generated by a

sequence of random variables. Figure 8 shows a possible realization of the steel weight loss on rebar in a RC beam generated based on the random field theory [17].

Procedure for Simulating Stochastic Field

The procedure for simulating a random field is generally composed of three main steps: (1) evaluation of statistical characteristics (e.g., probabilistic distribution type, mean, standard deviation, and correlation length) for a variable based on experimental data, (2) defining random field mesh size, and (3) generating random field. A random field can be generated based on several methods, such as Covariance Matrix Decomposition (CMD) [48, 50, 51], the Spectral Representation Method (SRM) [19, 52–54], Karhunen–Loève Expansion (KLE) [55, 56], and the Local Average Subdivision (LAS) method [57, 58]. Figure 9 shows a general procedure for simulating random fields.

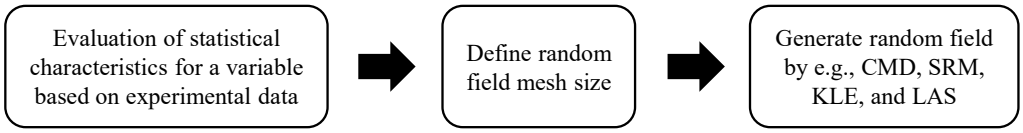

Figure 9 General procedure for simulating random fields.

Correlation Function and Correlation Length

The correlation function is a function that represents the statistical correlation between random variables according to the spatial distance between the variables. In comparison, the correlation length is a parameter in a correlation function that represents the variability in the random field. Figure 10 shows the influence of the correlation length in a random field for the compression strength in a concrete beam of 5 m long. As presented in Figure 10, the random field simulated using a shorter correlation length (i.e., 50 cm) displays a shorter correlation among the variables in a random field than that simulated by a longer

correlation length (i.e., 200 cm).

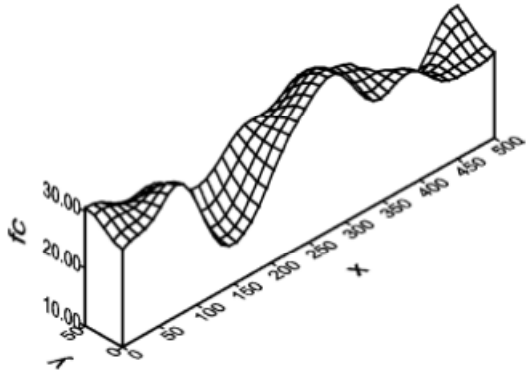

(a) Correlation length = 50 cm

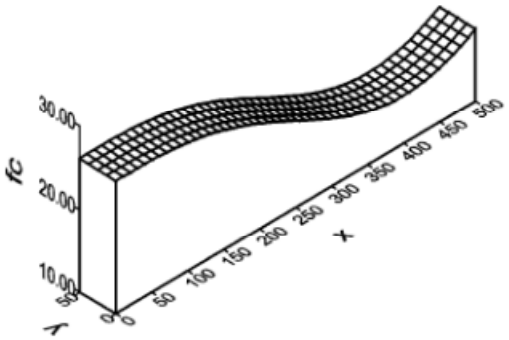

(b) Correlation length = 200 cm

Figure 10 Influence of correlation length in random fields of the compressive strength (f_c) for a RC beam [59].

Gaussian and non-Gaussian Random Field

A random field is Gaussian if the random variables are all normally distributed. When the mean, variance and correlation function of a Gaussian random field are known the random field is completely defined. In contrast, if the random variables are non-Gaussian, the random field is non-Gaussian. If a non-linear transformation is possible between the non-Gaussian and Gaussian random variables, the non-Gaussian random field can be obtained

by a non-linear transformation of a Gaussian random field. The log-normal (i.e., non-Gaussian) distributed random field is vital in the modeling of engineering problems due to its non-negative domain. This transformation is provided in more detail in part of the dissertation.

Univariate and Multivariate Random Field

The physical quantities involved in the probabilistic model of problems in mechanics are very often described by a number of correlated variables; for example, the ultimate strength and ultimate elongation of a cable wire are correlated, the various mechanical properties of a soil are correlated. In other circumstances, it is very beneficial to substitute an n-dimensional random field (or wave, meaning that one dimension is in the time domain, and the others are in the space domain) by a set of correlated $(n-1)$-dimensional univariate (UV) fields/processes/waves. For example, the wind speed is a random wave that is usually modeled as a set of random processes, each of them relative to a particular point (e.g., see [60]). In both of these cases, a multivariate (MV) random field generator is required [61]. In other words, an MV random field is a set of correlated UV random fields.

Spectral Representation of Random Field

In some cases, the second-order properties of a random field are expressed in the frequency domain with the spectral density function (SDF), which is comparable with the covariance function in the spatial domain. The simulation approach that utilizes the SDF to generate a random field is named SRM. SRM is a versatile method that can be utilized to simulate Gaussian and non-Gaussian random fields, UV and MV random fields, and multidimensional random fields. A series of papers provided herein are listed according

to types of the simulation in the order of UV Gaussian, MV Gaussian, UV non-Gaussian and, and MV non-Gaussian random fields in the following paragraphs, respectively.

SRM for the simulation of UV and MV Gaussian random fields has been introduced by Shinozuka and Jan [62]. Many further developments for the simulation of UV Gaussian random fields have been proposed over the years by Shinozuka and Deodatis [63, 64]. Meanwhile, Deodatis [65] has improved the simulation of MV Gaussian random fields taken into account for an ergodic property. The applications of UV Gaussian SRM include, for example, simulating the corrosion process in RC beams [53] and RC slabs [10, 19, 54]. In comparison, an application of MV Gaussian SRM is a simulation of wind velocity fields [52].

For the simulation of UV non-Gaussian random fields, Yamazaki and Shinozika [66] proposed the SRM-based iterative methodology according to a target non-Gaussian SDF and a target non-Gaussian marginal cumulative density function (CDF). Their method is based on Grigoriu's translation field theory [67, 68]. Since the methodology proposed by Yamazaki and Shinozika [66] was confirmed later that its accuracy is less than ideal, Deodatis and Micaletti [69] proposed some modifications using a "compatibility check" to confirm whether the target non-Gaussian SDF and the prescribed non-Gaussian marginal CDF are compatible or not. As a result, their proposed method dramatically improved the accuracy of the simulation. Simultaneously, Shi and Deodatis [70] have developed a methodology with similar accuracy to the Deodatis and Micaletti algorithm [69]. Recently, Shields, Deodatis and Bocchini [71] have developed the SRM-based iterative technique for generating UV non-Gaussian random fields. The proposed algorithm is conceptually much simpler, and at the same time, considerably more efficient computationally. The applications of UV non-Gaussian SRM have contributed to, for example, simulation of corrosion process of steel beams [72], RC beams [53], and RC slabs [19, 20], simulation of damage levels of bridges [73].

The simulation of MV non-Gaussian random fields using SRM has been introduced by Popescu, Deodatis, and Prevost [74]. The proposed methodology starts by simulating Gaussian MV random fields that is then transformed into desired non-Gaussian ones using Grigoriu's translation field theory [67, 68] in conjunction with the iterative family approach [66]. Up until lately, Shields and Deodatis [75] have introduced the conceptually simple and computationally efficient methodology for simulating UV non-Gaussian random fields proposed by Popescu, Deodatis, and Prevost [71] into the simulation of MV non-Gaussian random fields. An example of the application of MV non-Gaussian SRM is a simulation of wind fields [75].

One of the main purposes of this dissertation is to propose a procedure for simulating steel weight loss of multiple rebars RC beams in the stochastic field context by considering the effect of the interaction of corrosion pits among the rebars. Therefore, based on the above-developed methodologies, the main concerns are (1) representation of random fields for steel weight loss in multiple rebars RC members (i.e., UV or MV random fields), (2) probability distribution types of the steel weight loss (i.e., Gaussian or non-Gaussian), and (3) parameters for the simulation (i.e., mean, standard deviation, and correlation parameters). To answer these questions, the nature of steel weight loss in multiple rebars RC members is observed and discussed in Chapter 3.

Chapter 3: Estimation of Steel Weight Loss Distributions of Multiple Tensile Rebars in a Corroded RC Slab

To investigate the effect of the interaction of corrosion pits among tensile rebars in the transverse direction, an experimental procedure for a corroded RC slab specimen that contains multiple rebars was established. Based on the test results of the spatial steel weight loss distributions obtained from an RC slab specimen that contains multiple rebars, the interaction of the steel corrosion pits is observed based on the correlation of the corrosion pits in the transverse direction. To determine whether the transverse correlation of steel weight loss distributions needs to be considered in the reliability analysis, the experimental procedure is conducted on a single RC slab specimen. The effects of several factors, including the concrete properties, tensile rebar diameter, tensile rebar spacing and concrete cover, are beyond the scope of this study. However, further research is needed to investigate the effects of these parameters on the degree of steel corrosion correlation among tensile rebars.

3.1 Experimental Procedure

3.1.1 Accelerated Corrosion Test

The details of an RC slab specimen with three tensile rebars are presented in Figure 11 and the details of the concrete mixing proportions are shown in Table 1. The RC slab specimen was cured for 28 days after casting, and then accelerated steel corrosion was induced. According to the standard NT Build 492 [36], several accelerated corrosion methods have been commonly utilized, e.g., galvanostatic methods, artificial climate environmental methods, and accelerated chloride migration methods. In this study, a galvanostatic method (the so-called impressed current technique) was applied [36]. A

schematic and a photograph of the experimental setup are shown in Figures 12(a) and (b), respectively.

Table 1. Concrete mixing proportions.

G_{max} (mm)	W/C (%)	Water (kg/m^3)	Cement (kg/m^3)	Fine aggregate (kg/m^3)	Coarse aggregate (kg/m^3)	AE (mL/m^3)
20	50	181	362	754	961	2715

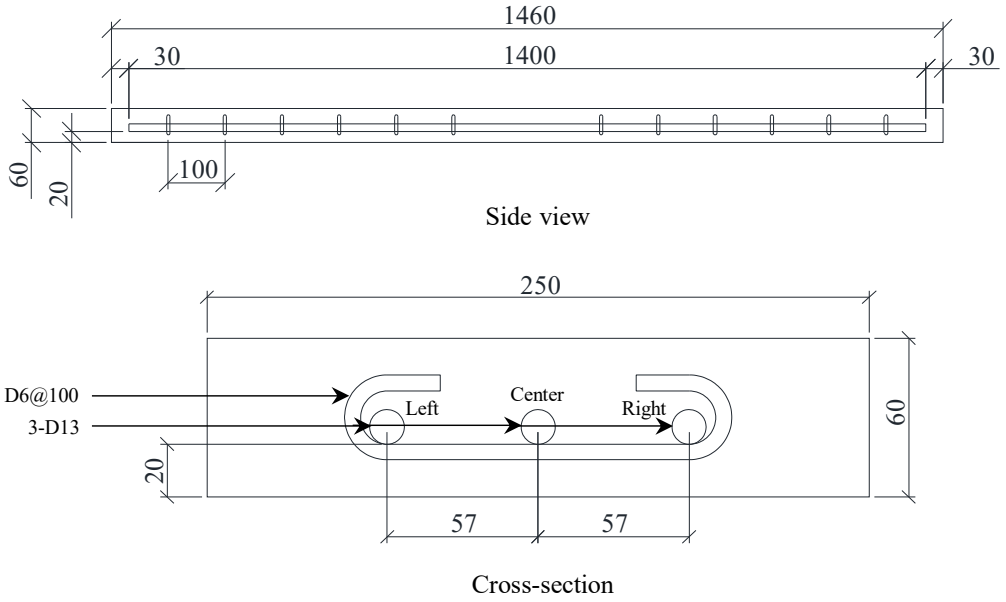

Compressive strength of concrete: 37.8 MPa (28 days)
Yield strength of longitudinal rebar: 388 MPa

Figure 11 Details of the RC slab specimen (all dimensions are in mm).

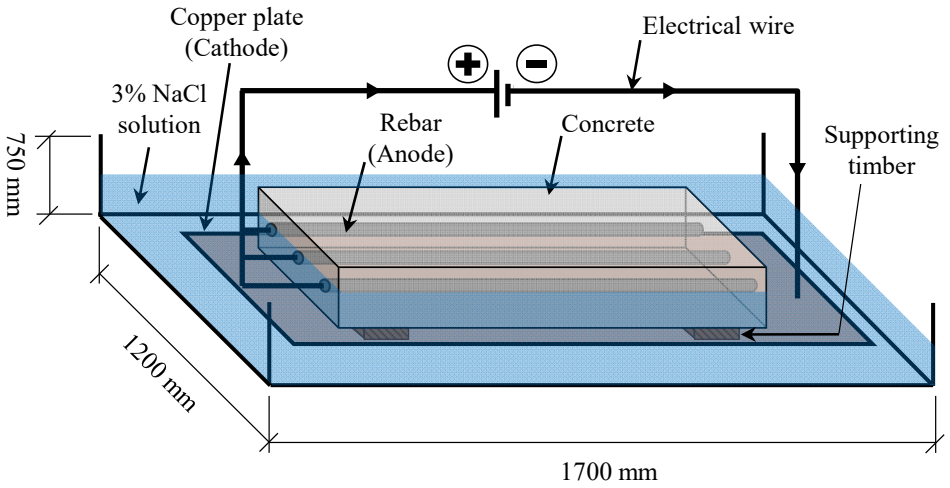

(a) Schematic diagram of the accelerated corrosion process for the RC slab specimen

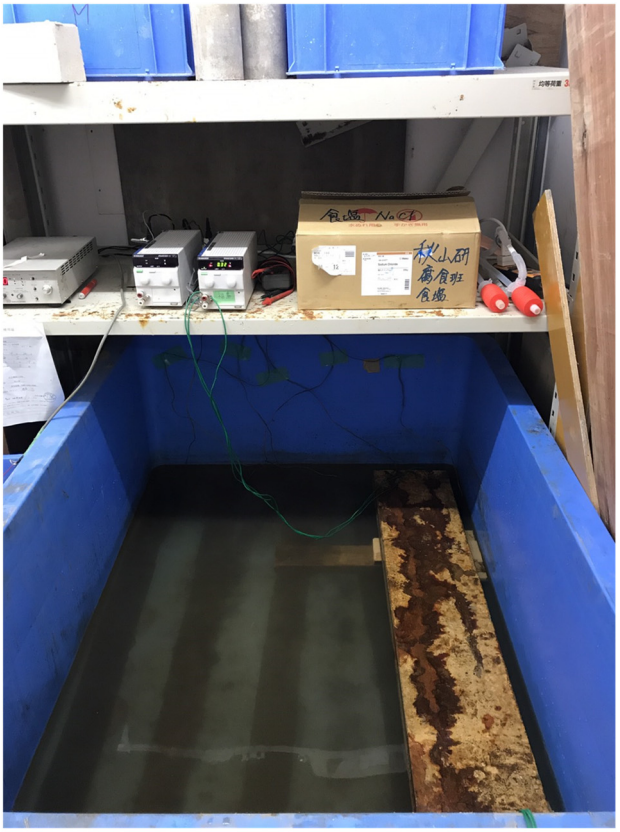

(b) Photograph of the experimental setup for the accelerated corrosion test on the RC slab specimen.

Figure 12 (a) Schematic diagram of the accelerated corrosion process for the RC slab specimen and (b) photograph of the experimental setup for the accelerated corrosion test on the RC slab specimen.

The RC slab specimen was placed on two pieces of supporting timber and partially immersed in a chloride solution with 3.0 wt.% NaCl (refer to Figures 12(a) and (b)) in the temperature range 23-25 ℃. The anode side and cathode side were connected to the rebars and the copper plate under the RC slab specimen, respectively. The power supply selected for this experiment was set to 200 μA/cm^2. An equal amount of current was applied to all the tensile rebars by connecting them in parallel with the positive electrode of the current generator [76], as shown in Figure 12(a), to obtain a similar amount of corrosion for all three rebars. The accelerated corrosion process proceeded until the accumulated current time reached approximately 3250 h (i.e., approximately five months). Notably, a low current density close to natural conditions (i.e., 100 μA/cm^2) has been found to cause highly localized corrosion in RC members [17]. However, it takes a long time to achieve such corrosion tests. Therefore, in this experimental procedure, an impressed current density of 200 μA/cm^2 was applied to corrode the rebars within a reasonable time frame. A future study is needed to address the effect of current density on the correlation of the steel corrosion pits in the transverse direction.

Noted that generally, both concrete beams and slabs are the structural element in bending. However, the depth of a concrete slab is significantly smaller compared to its span. Since the covering concrete at the top of RC slab is less than that of beams, the RC slab specimen herein was partially immersed in 3% NaCl solution in order that the chloride ions can diffuse only from the bottom of the specimen. Therefore, the steel weight loss distributions obtained from the slab in this dissertation can also be applied with the beam element.

3.1.2 Estimation of Steel Weight Loss Distributions

During the accelerated corrosion process, the amount of corrosion in the rebars was evaluated by the localized steel weight loss (*Rw*) using X-ray images [24] at four target

corrosion levels. The mean values of the localized steel weight loss for all the tensile rebars (*MRw*) were expected to be 5%, 10%, 15%, and 20%; note that the *MRw* values estimated by X-ray were 4.10%, 7.88%, 15.73% and 18.84%, respectively. *MRw* is defined as follows:

$$MRw = \frac{1}{m}\sum_{i=1}^{m}(MRw_{S,i}), \tag{8}$$

where

$$MRw_{S,i} = \frac{1}{M}\sum_{u=1}^{M}Rw_i(u), \tag{9}$$

m is the number of tensile rebars in the RC member (i.e., m = 3 for this experiment); $MRw_{S,i}$ is the mean steel weight loss over a single rebar i (i.e., i = 1, 2 and 3 represent the left rebar, center rebar and right rebar, respectively) (refer to Figure 11); $Rw_i(u)$ is the localized steel weight loss at location u (%) per length L (mm) over a single rebar i; and M is the total number of locations where the steel weight loss measurements are performed on a single rebar.

The configuration of the X-ray machine employed in this study is illustrated in Figure 13. The range for the captured X-ray images of the original and corroded rebars in the RC slab specimen is between 270 mm and 1100 mm from the left side of the slab. Note that the length of an X-ray image is 60 mm (equivalent to the length of an X-ray photogram), as illustrated in Figure 14(a). The X-ray images were obtained by an X-ray apparatus from 3 viewing angles (120°, 180°, and 240°), as shown in Figure 14(b). Example X-ray images of the original and corroded rebars after digital image processing are shown in Figure 15.

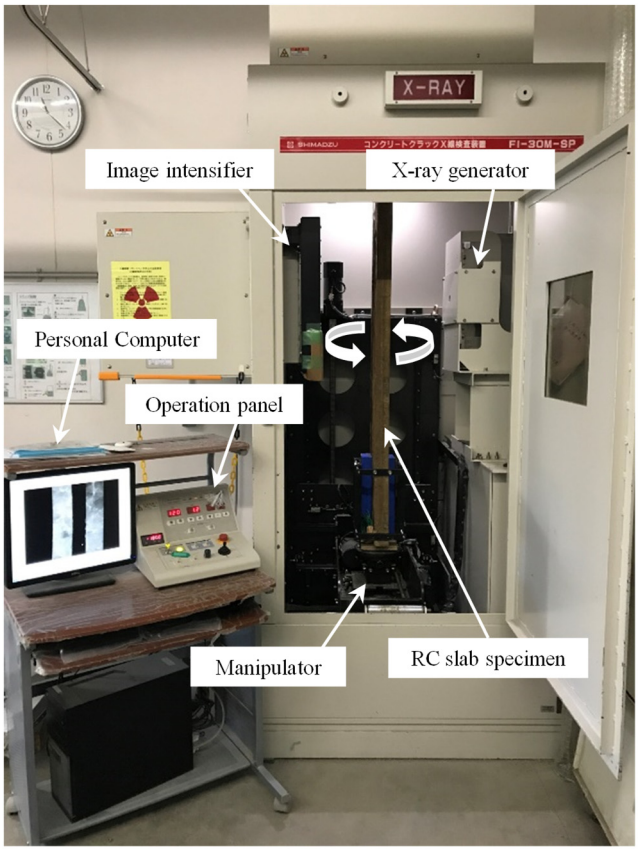

Figure 13 X-ray imaging configuration.

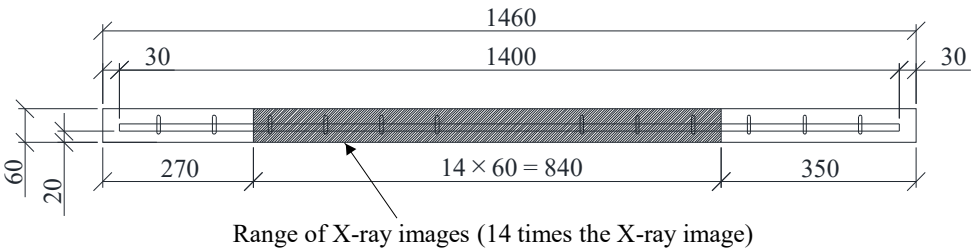

(a) Range of captured X-ray images

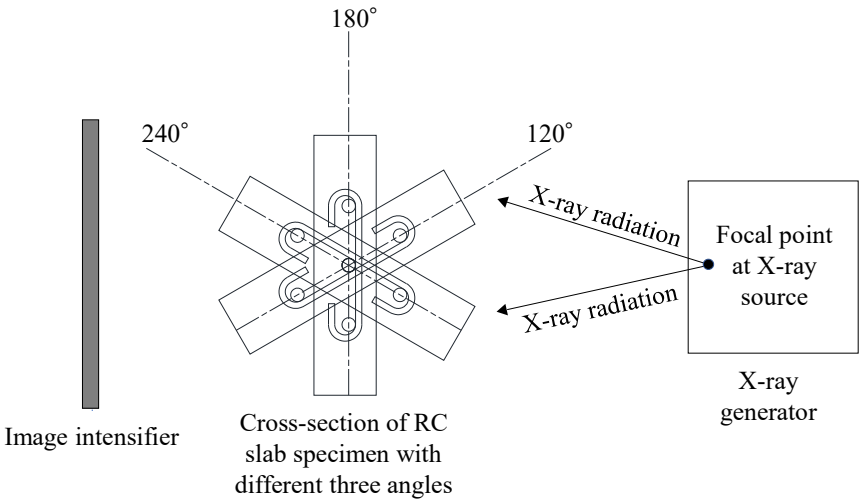

(b) Three viewing angles (120°, 180°, and 240°) for capturing the center rebar

Figure 14 X-ray imaging of the RC slab specimen: (a) range of captured X-ray images and (b) three viewing angles (120°, 180°, and 240°) for capturing the center rebar (all dimensions are in mm).

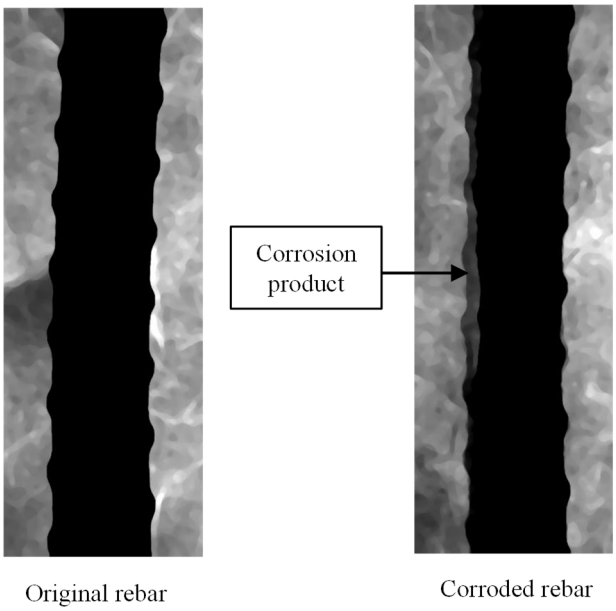

Figure 15 Example X-ray images of the original and corroded rebars after digital image processing.

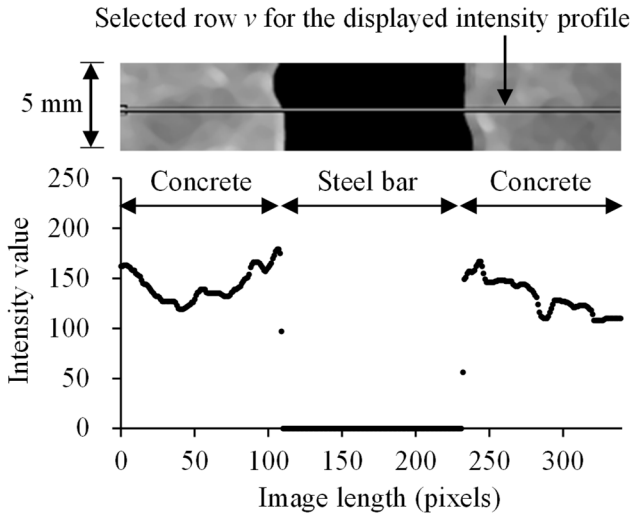

Figure 16 Example of profile for the intensity values for the row *v* of pixels in an X-ray image.

The X-ray images show the black and white indicating the X-ray intensity after penetrating through a material. Generally, the X-ray intensity after penetrating through the concrete is higher than that after penetrating through the rebar. According to the difference in the intensity of the pixel, the boundary between concrete and rebar, or between concrete and corrosion products could be detected using digital image processing. Therefore, by attuning the grey values for pixels of the steel bar, the total number of pixels under a threshold of grey value that represent the extent of the steel bar can be counted using the image processing software. Figure 16 shows an example of a profile for the intensity values for a selected row *v* of pixels in an X-ray image.

After the number of pixels of the original and corroded steel bar was estimated, the total area was acquired by multiplying the number of pixels by the unit area per pixel as follows:

$$A_{i,\theta_\psi}(v) = P_{i,\theta_\psi}(v) \times A_p \tag{10}$$

$$A'_{i,\theta_\psi}(v) = P'_{i,\theta_\psi}(v) \times A_p \tag{11}$$

where $A_{i,\theta_\psi}(v)$ and $A'_{i,\theta_n}(v)$ are the areas of the original and corroded rebar *i*, respectively at a viewing angle for the row *v* of pixels in an X-ray image, θ_ψ represents the ψ-th viewing angle, $P_{i,\theta_\psi}(v)$ and $P'_{i,\theta_\psi}(v)$ are the number of pixels for the area of the original and corroded rebar *i*, respectively at viewing angle θ_ψ of the image row *v*, and A_p is the unit area (mm^2 /pixel) for the X-ray image. Then, the volume of the rebar before and after corroding at a location *u* can be estimated by:

$$V_{i,\theta_\psi}(u) = \frac{\pi\left[A_{i,\theta_\psi}(v)\right]^2}{4L} \tag{12}$$

$$V'_{i,\theta_\psi}(u) = \frac{\pi\left[A'_{i,\theta_\psi}(v)\right]^2}{4L} \tag{13}$$

where $V_{i,\theta_\psi}(u)$ and $V'_{i,\theta_\psi}(u)$ are the volumes of the original and corroded rebar *i*, respectively, of the location *u* at viewing angle θ_ψ, and *L* is the length of the rebar, which is 5 mm herein.

Accordingly, the steel weight loss per length *L* (mm) of the rebar *i* at location *u*, $Rw_i(u)$ was obtained by taking the average of each value of the steel weight loss for each viewing angle as follows:

$$Rw_i(u) = \frac{1}{\lambda}\sum\frac{\left[V_{i,\theta_\psi}(u) - V'_{i,\theta_\psi}(u)\right]}{V_{i,\theta_\psi}(u)} \times 100 \tag{14}$$

where *Rw* is the steel weight loss in percentage (%) per length *L* (mm) of rebar and λ is the number of viewing angles (λ = 3 for the 3 different viewing angles applied herein i.e., 120°, 180°, and 240°). Note that the length for evaluating *Rw* (i.e., *L* = 5 mm) is selected to be lower than the length of the rebar element utilized in the FE model, which is described in Chapter 4.5.

3.1.3 Validation of the Steel Weight Loss Distributions Measurement

After the accelerated corrosion process, the three tensile rebars were separated from the RC slab specimen and immersed in a 10% diammonium hydrogen citrate solution for 24 h to remove the corrosion products. Gravimetric mass loss measurements were conducted to acquire the steel weight loss results along each rebar. These results were compared with the mean steel weight loss of rebar i, $MRw_{S,i}$ (i = 1, 2, and 3), which was determined with Eq. (9), for validation purposes. Table 2 shows that the absolute errors of the steel weight loss of the three rebars (i.e., left, center and right rebars) obtained from the gravimetric mass loss measurements and $MRw_{S,i}$, as estimated by the X-ray technique, are approximately 1%. A possible reason for the measurement errors was the inability of the projected 2D X-ray images to provide information about localized corrosion on the rebar surface, which is discussed in detail by Lim et al. (2017) [24].

All the verified $MRw_{S,i}$ values indicate that the application of X-ray imaging to an RC slab specimen with multiple tensile rebars is effective, as previously illustrated for an RC beam with a single tensile rebar [23, 24].

Table 2. Validation of steel weight loss estimation.

Rebar*	$MRw_{S,i}$ estimated by the X-ray technique (Eq. (9))	Steel weight loss measured by the gravimetric method	Absolute error
Left (i = 1)	22.1%	22.9%	0.77%
Center (i = 2)	19.3%	19.5%	0.19%
Right (i = 3)	15.1%	16.4%	1.38%

*

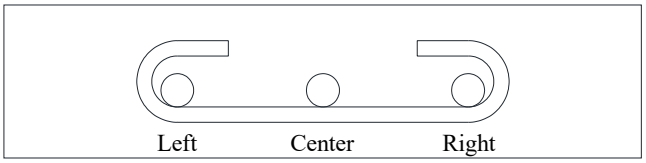

Cross section of RC slab specimen

3.2 Experimental Results and Discussion

Figure 17 shows the distributions of the localized steel weight loss *Rw*, which is estimated by the X-ray images of three tensile rebars in the RC slab specimen. The results show that the *Rw* distributions are not uniform and vary spatially. Furthermore, similar *Rw* profiles were obtained among the tensile rebars in the RC slab specimen for all the corrosion levels.

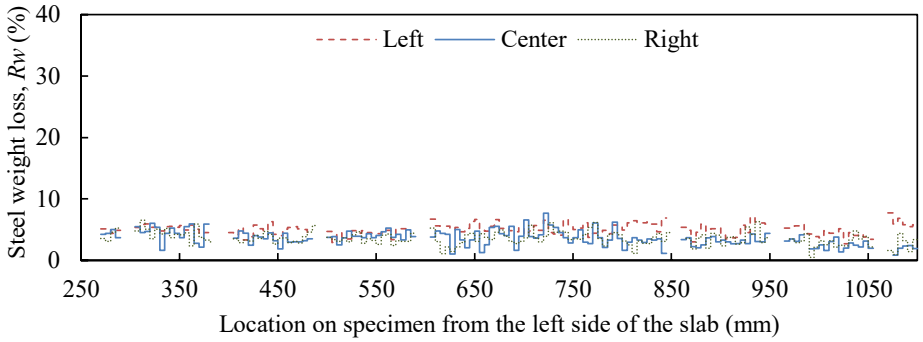

(a) Spatial steel weight loss distributions of three tensile rebars in the RC slab specimen at 1st X-ray, *MRw* = 4.10%

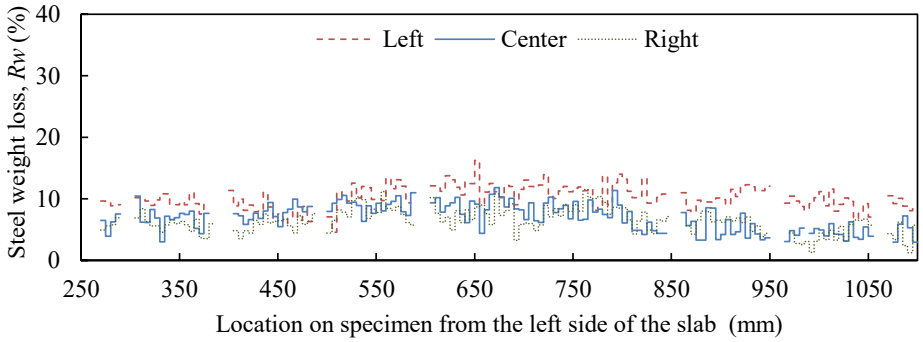

(b) Spatial steel weight loss distributions of three tensile rebars in the RC slab specimen at 2nd X-ray, *MRw* = 7.88%

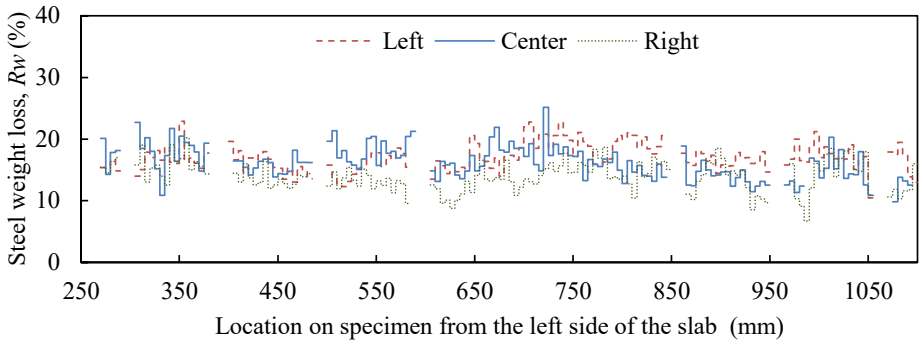

(c) Spatial steel weight loss distributions of three tensile rebars in the RC slab specimen at 3rd X-ray, MRw = 15.73%

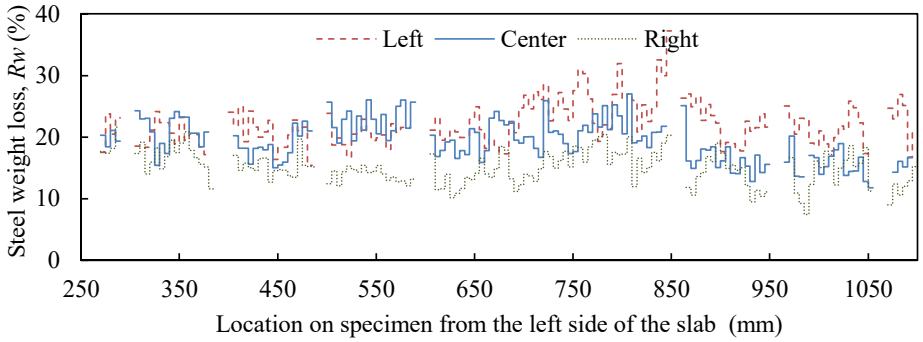

(d) Spatial steel weight loss distributions of three tensile rebars in the RC slab specimen at 4th X-ray, MRw = 18.84%

Figure 17 Spatial steel weight loss distributions of three tensile rebars in the RC slab specimen estimated by X-ray and digital image processing techniques: (a) 1st X-ray, MRw = 4.10%; (b) 2nd X-ray, MRw = 7.88%; (c) 3rd X-ray, MRw = 15.73%; and (d) 4th X-ray, MRw = 18.84%.

To estimate correlation values of the steel weight loss between a pair of rebars i and j (i.e., i, j = 1, 2, 3 in this experiment), ρ_{ij}, the Pearson correlation is adopted herein as:

$$\rho_{ij} = \frac{\sum_{u=1}^{M}\left(Rw_i(u) - MRw_{S,i}\right)\left(Rw_j(u) - MRw_{S,j}\right)}{\sqrt{\sum_{u=1}^{M}\left(Rw_i(u) - MRw_{S,i}\right)^2}\sqrt{\sum_{u=1}^{M}\left(Rw_j(u) - MRw_{S,j}\right)^2}} \quad (i \neq j) \tag{15}$$

Figure 18 presents the matrixes of ρ_{ij} for the steel weight loss distributions among the

rebars at all corrosion levels. It is confirmed that the steel weight loss distributions are correlated among the rebars. Based on these results, it demonstrates that the spatial distributions of steel weight loss in multiple tensile rebars are also correlated in the transverse directions. Therefore, both directional correlations of steel weight loss (i.e., longitudinal and transverse directions) should be considered when performing the simulation. Moreover, the correlation values of steel weight loss distributions between the pair of adjacent rebars (i.e., Left-Center and Center-Right) are likely to be higher than that of the single skipped rebars (i.e., Left-Center), as shown in Figure 18. This indicates that the spacing between the rebars might affect the correlation of steel weight loss in the transverse direction. Accordingly, this effect is comprehensively discussed in the simulation process provided in Chapter 4.

The spatial variability in steel weight loss in both the longitudinal and transverse directions is explained by the fact that the macroscopic mechanical properties of concrete are remarkably discrete due to the random distribution of coarse aggregates and pores. Due to the nonuniform distribution of pores in concrete materials, chloride ions migrate through the pore solution in the concrete by different transfer paths, leading to the difference in chloride ion accumulation on the surface of the rebar. As a result, the final distribution of the corrosion products becomes nonuniform [77]. Further experimental work should be focused on identifying factors that lead to the correlated steel weight loss distributions of rebars in both the longitudinal and transverse directions.

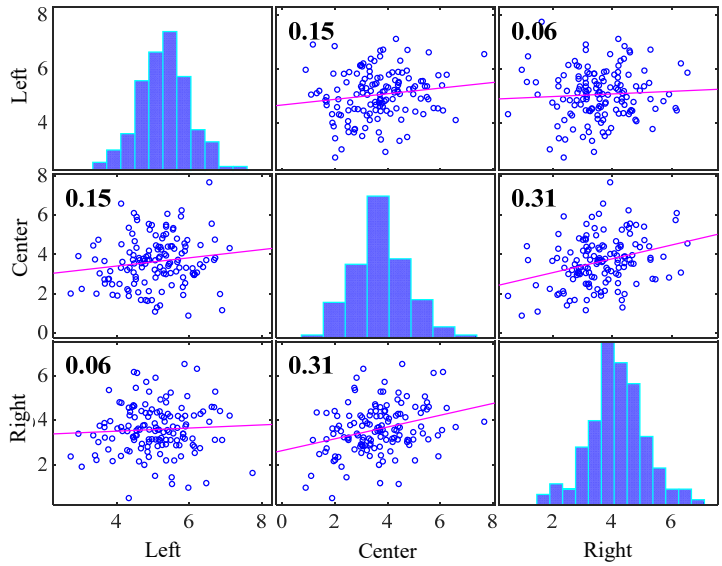

(a) Correlation matrix of steel weight loss among the three tensile rebars in the RC slab specimen at 1st X-ray, *MRw* = 4.10%

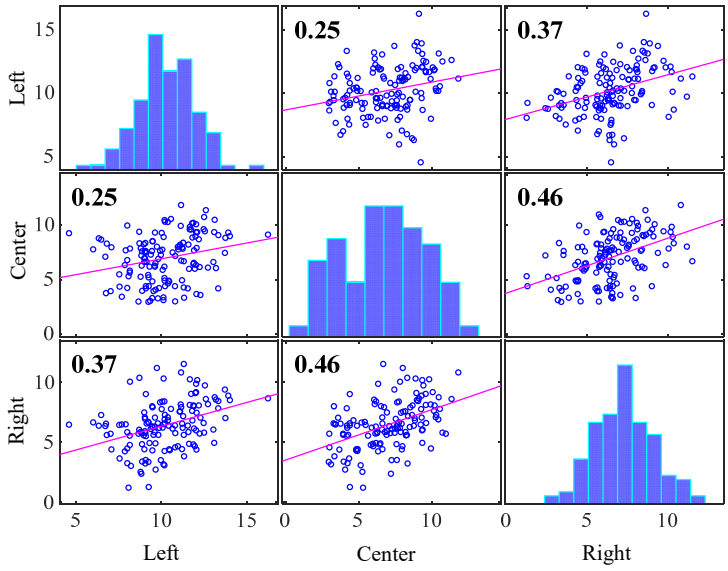

(b) Correlation matrix of steel weight loss among the three tensile rebars in the RC slab specimen at 2nd X-ray, *MRw* = 7.88%

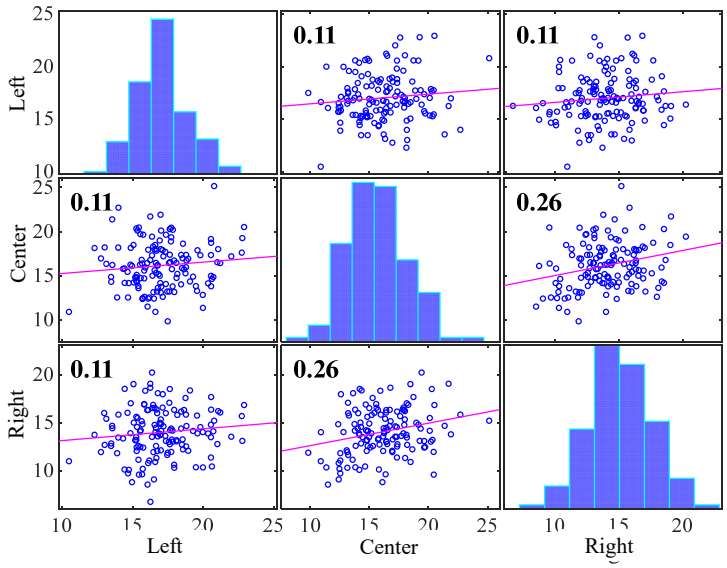

(c) Correlation matrix of steel weight loss among the three tensile rebars in the RC slab specimen at 3rd X-ray, *MRw* = 15.73%

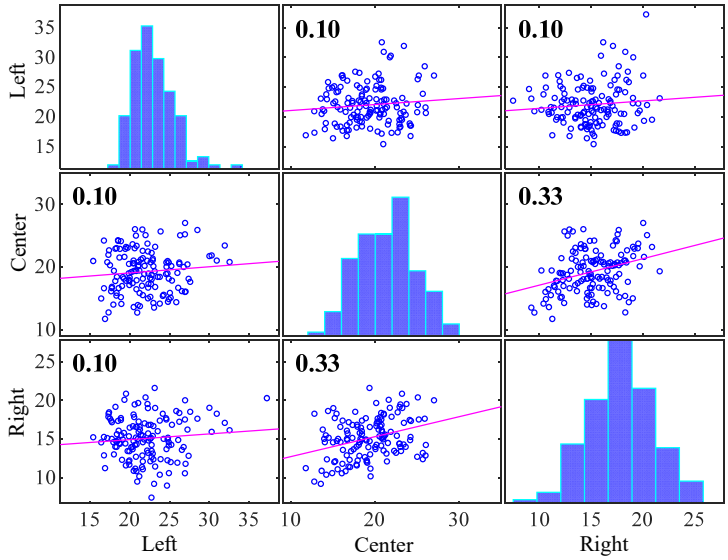

(d) Correlation matrix of steel weight loss among the three tensile rebars in the RC slab specimen 4th X-ray, *MRw* = 18.84%

Figure 18 Correlation matrix of steel weight loss among the three tensile rebars in the RC slab specimen estimated by X-ray and digital image processing techniques: (a) 1st X-ray, *MRw* = 4.10%; (b) 2nd X-ray, *MRw* = 7.88%; (c) 3rd X-ray, *MRw* = 15.73%; and (d) 4th X-ray, *MRw* = 18.84%.

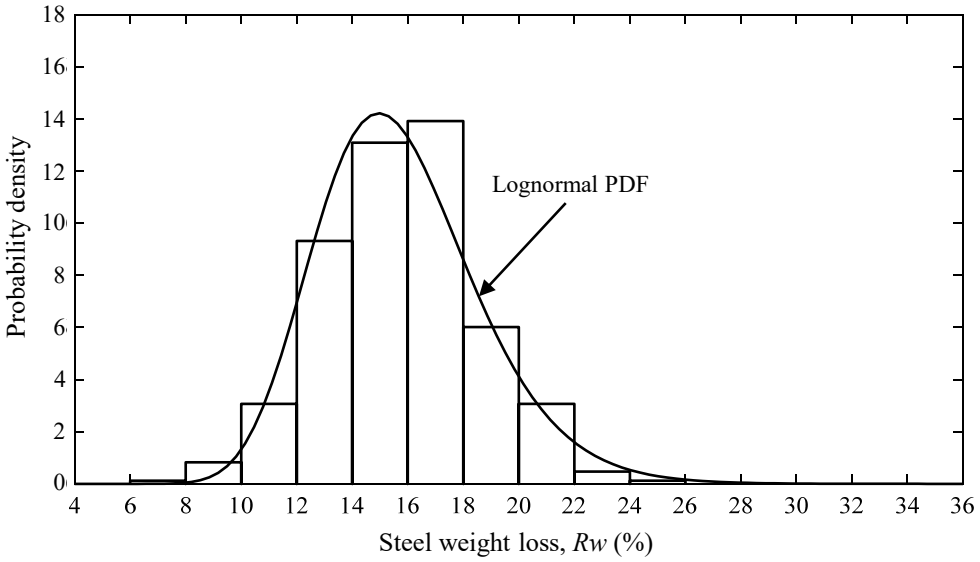

(a) Relative frequency histogram and lognormal PDF of steel weight loss, *Rw* (%), in the corroded RC slab specimen for *MRw* = 15.73% in the 3rd X-ray

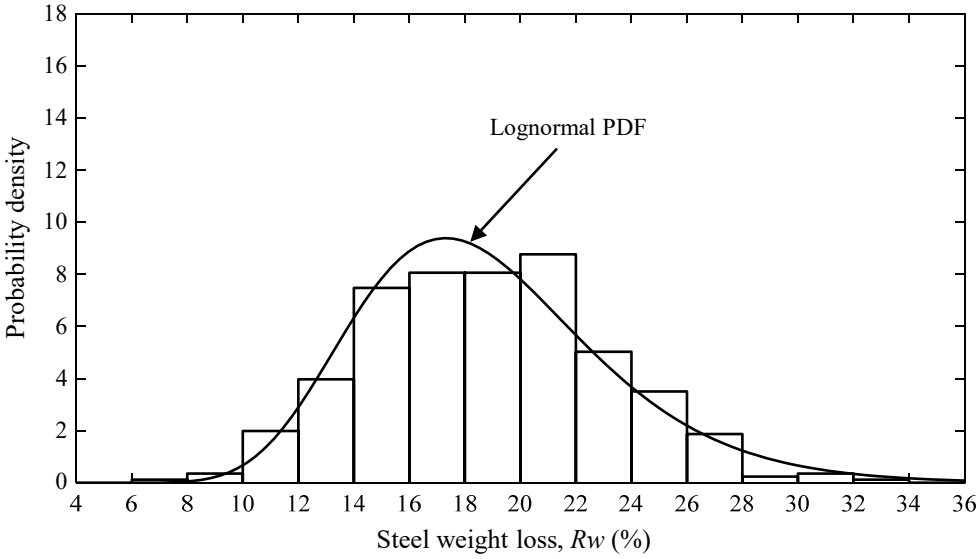

(b) Relative frequency histogram and lognormal PDF of steel weight loss, *Rw* (%), in the corroded RC slab specimen for *MRw* = 18.84% in the 4th X-ray

Figure 19 Example relative frequency histogram and lognormal PDF of steel weight loss, *Rw* (%), in the corroded RC slab specimen: (a) *MRw* = 15.73% in the 3rd X-ray and (b) *MRw* = 18.84% in the 4th X-ray.

Previous statistical analysis results have demonstrated that the distribution of the steel corrosion pattern along the length of a corroded rebar is well represented by a lognormal distribution [78, 79]. This finding was also confirmed in this experiment. Figure 19 shows that the relative frequency histograms of *Rw* for all three rebars in the RC slab specimen follow a lognormal probability density function (PDF). Hence, the spatial steel weight loss distributions that are simulated herein are assumed to be lognormally distributed.

Chapter 4: Stochastic Simulation and Structural Performance Assessment of Corroded Multiple Rebars RC Structures

4.1 Spectral Representation of MV Random Fields

The SRM is a very versatile method that can be applied to generate Gaussian and non-Gaussian random fields, UV and MV random fields, and multidimensional random fields [61, 63, 65, 66, 74]. Using SRM, previous studies have simulated steel corrosion in reinforcing bars of RC structures, which evolves over time and at continuous locations in space in UV random fields [19, 20, 72, 80]. However, based on the experimental data in Chapter 3, the *Rw* profiles and the correlation matrixes of the spatial steel weight loss distributions reveal a significant transverse correlation among the three tensile rebars. Therefore, the spatial steel weight loss distributions should not be represented by three UV (i.e., uncorrelated) random fields. Instead, the most appropriate solution is to simulate the steel weight loss distributions as MV random fields [61, 65]. With this approach, the transverse correlation of steel weight loss among the tensile rebars can be considered in the stochastic simulation. A general approach for simulating MV random fields using the SRM is introduced in this subchapter. By applying this simulation technique, a procedure is proposed to generate the spatial steel weight loss distributions of multiple rebars for RC members in Chapter 4.2.

4.1.1 Simulation of MV random fields

To model the cross-correlation of vector fields, the Gaussian cross-spectral density matrix (CSDM), $\mathbf{S}(\kappa)$, is defined as follows [65]:

$$\mathbf{S}(\kappa)=\begin{bmatrix} S_{11}(\kappa) & S_{12}(\kappa) & \cdots & S_{1m}(\kappa) \\ S_{21}(\kappa) & S_{22}(\kappa) & \cdots & S_{2m}(\kappa) \\ \vdots & \vdots & \ddots & \vdots \\ S_{m1}(\kappa) & S_{m2}(\kappa) & \cdots & S_{mm}(\kappa) \end{bmatrix} \tag{16}$$

where m is the number of components, κ is the wavenumber, and $S_{ij}(\kappa)$ represents the cross-SDF values, which are defined as follows [61]:

$$S_{ij}(\kappa)=\gamma_{ij}(\kappa)\sqrt{S_{ii}(\kappa)S_{jj}(\kappa)}, \qquad i,j=1,2,...,m, \tag{17}$$

where

$$\Delta\kappa=\frac{\kappa_u}{N}$$
$$\kappa=n\Delta\kappa,\ n=0,\ 1,\ 2,...,N-1$$

The terms $S_{ii}(\kappa)$ and $S_{jj}(\kappa)$ denote the auto-SDF of rebars i and j, respectively; $\gamma_{ij}(\kappa)$ is the coherence function; κ_u is the upper cutoff frequency beyond which the spectral density can be assumed to be zero; and N is a parameter defining the number of discretization points in the wavenumber domain. N is related to the number of discrete locations in a simulated vector (M) because of the following anti-aliasing requirement: $M \geq 2N$ [63].

With the Gaussian CSDM, $\mathbf{S}(\kappa)$, as expressed in Eq. (16), MV random fields of m components can be simulated. A general computational procedure is explained in the following six steps [61].

(I) $\mathbf{S}(\kappa)$ is decomposed to satisfy the following equation:

$$\mathbf{S}(\kappa)=\mathbf{H}(\kappa)\mathbf{H}^{*T}(\kappa) \tag{18}$$

where * denotes the complex conjugate and T denotes the transpose operator. This decomposition can be performed with several existing methods [81].

With Cholesky's decomposition, the matrix **H** can be obtained recursively as follows [82]:

$$H_{ii} = \sqrt{S_{ii} - \sum_{e=1}^{i-1} H_{ie}^2} \tag{19}$$

$$H_{ij} = \frac{1}{H_{jj}}\left(S_{ij} - \sum_{e=1}^{j-1} H_{ie} H_{je} \right), \qquad \text{for } i > j \tag{20}$$

Here define the quantities $w_{ij}(\kappa)$ as:

$$w_{ij}(\kappa) := \frac{\left|H_{ij}(\kappa)\right|^2}{S_{ii}(\kappa)} \quad \Rightarrow \quad \left|H_{ij}(\kappa)\right| = \sqrt{w_{ij}(\kappa) S_{ii}(\kappa)} \tag{21}$$

The diagonal terms of $\mathbf{H}(\kappa)$ can be described as:

$$H_{ii} = \sqrt{S_{ii} - \sum_{e=1}^{i-1} w_{ie} S_{ii}} = \sqrt{\left(1 - \sum_{e=1}^{i-1} w_{ie}\right) S_{ii}} \tag{22}$$

Comparing Eq. (22) to the definition in Eq. (21), w_{ii} is:

$$w_{ii} = 1 - \sum_{e=1}^{i-1} w_{ie} \tag{23}$$

which implies:

$$\sum_{e=1}^{i-1} w_{ie} = 1 \tag{24}$$

In turn, the cross terms w_{ij} are provided by:

$$\begin{aligned} w_{ij} &:= \frac{\left|H_{ij}\right|^2}{S_{ii}} = \\ &= \frac{1}{S_{ii}} \frac{1}{H_{jj}^2}\left(S_{ij} - \sum_{e=1}^{j-1} H_{ie} H_{je} \right)^2 = \\ &= \frac{1}{S_{ii}} \frac{1}{w_{jj} S_{jj}}\left(\sqrt{S_{ii} S_{jj}}\,\gamma_{ij} - \sum_{e=1}^{j-1} \sqrt{w_{ie} S_{ii}}\sqrt{w_{je} S_{jj}} \right)^2 = \\ &= \frac{1}{S_{ii} w_{jj} S_{jj}} S_{ii} S_{jj}\left(\gamma_{ij} - \sum_{e=1}^{j-1} \sqrt{w_{ie} w_{je}} \right)^2 = \\ &= \frac{1}{w_{jj}}\left(\gamma_{ij} - \sum_{e=1}^{j-1} \sqrt{w_{ie} w_{je}} \right)^2, \quad \text{for } i > j \end{aligned} \tag{25}$$

The recursive Eqs. (23) and (25) show that the variables $w(\kappa)$ are functions only of the coherences $\gamma(\kappa)$. So, in general,

$$\left|H_{ij}(\kappa)\right| = \sqrt{w_{ij}(\kappa) S_{ii}(\kappa)} \tag{26}$$

In this way, the Cholesky decomposition of $\mathbf{S}(\kappa)$ can be calculated knowing only the auto-SDF and coherence function. For instance, $w(\kappa)$ for the case of a vector process with three components (i.e., $m = 3$) can be obtain as:

$$\mathbf{w}(\kappa) = \begin{pmatrix} 1 & 0 & 0 \\ \gamma_{12}^2 & 1-\gamma_{12}^2 & 0 \\ \gamma_{13}^2 & \dfrac{\left(\gamma_{23}-\gamma_{12}\gamma_{13}\right)^2}{1-\gamma_{12}^2} & 1-\gamma_{13}^2-\dfrac{\left(\gamma_{23}-\gamma_{12}\gamma_{13}\right)^2}{1-\gamma_{12}^2} \end{pmatrix} \tag{27}$$

$$\mathbf{H}(\kappa) = \begin{pmatrix} \sqrt{S_{11}} & 0 & 0 \\ \gamma_{12}\sqrt{S_{22}} & \sqrt{1-\gamma_{12}^2}\sqrt{S_{22}} & 0 \\ \gamma_{13}\sqrt{S_{33}} & \dfrac{\gamma_{23}-\gamma_{12}\gamma_{13}}{\sqrt{1-\gamma_{12}^2}}\sqrt{S_{33}} & \sqrt{1-\gamma_{13}^2-\dfrac{\left(\gamma_{23}-\gamma_{12}\gamma_{13}\right)^2}{1-\gamma_{12}^2}}\sqrt{S_{33}} \end{pmatrix} \tag{28}$$

(II) The resulting lower triangular matrix $\mathbf{H}(\kappa)$ is applied to compute the functions $t_{ij}^{(s)}$ as follows:

$$t_{ij}^{(s)}(u\Delta x) = \mathrm{DFT}^{+}\left[2H_{ij}\left(n\Delta\kappa + \frac{j}{m}\Delta\kappa\right)\sqrt{\Delta\kappa}\exp\left(\mathrm{I}\varphi_{jn}^{(s)}\right)\right] \tag{29}$$

where

$n = 0,\ 1,\ldots,N-1$

$i = 1,\ 2,\ldots,m$

$j = 1,\ 2,\ldots,i$

$u = 0,\ 1,\ldots,M-1$

$\Delta x = \dfrac{2\pi}{M\Delta\kappa}$

$\varphi_{jn}^{(s)}$ are N random samples of phase angles uniformly distributed in the interval $[0,\ 2\pi]$ and associated with component j of sample s, Δx and $\Delta\kappa$ define the discretization in the space domain and wave number domain, respectively and $\mathrm{DFT}^{+}[\cdot]$ is the Discrete Fourier Transform defined as:

$$\mathrm{DFT}^{+}\left[\mathrm{Z}\right]=\sum_{\alpha=1}^{M}\mathrm{Y}\left(\kappa_{\alpha}\right)e^{\frac{2\pi}{M}\mathrm{I}(\beta-1)(\alpha-1)}=\mathrm{X}\left(x_{\beta}\right);\quad \beta=1,\ldots,M \tag{30}$$

X and Z are vectors of length M and I is the imaginary unit.

(III) Next, m copies of $t_{ij}^{(s)}$ are concatenated to generate $h_{ij}^{(s)}$ as follows:

$$h_{ij}^{(s)}\left(q\Delta x\right)=t_{ij}^{(s)}\left(\mathrm{mod}\left(q,M\right)\Delta x\right)\qquad q=0,\ 1,\ldots,mM-1 \tag{31}$$

where mod(q, M) is the remainder of the division of q by M.

(IV) Thereafter, $h_{ij}^{(s)}$ is multiplied by a shifting factor as follows:

$$\hat{h}_{ij}^{(s)}\left(q\Delta x\right)=\Re\left\{h_{ij}^{(s)}\left(q\Delta x\right)\cdot\exp\left[\mathrm{I}\frac{j}{m}\Delta\kappa\left(q\Delta x\right)\right]\right\} \tag{32}$$

where $\Re\{\cdot\}$ indicates the real part of the quantity in brackets.

(V) Each component i of the sample (s) of the MV and Gaussian random field is obtained by the following equation:

$$\hat{g}_{i}^{(s)}\left(q\Delta x\right)=\sum_{j=1}^{i}\hat{h}_{ij}^{(s)}\left(q\Delta x\right) \tag{33}$$

(VI) The standard Gaussian samples $\hat{g}_{i}^{(s)}$ are mapped to a desired non-Gaussian distribution using the translation field theory [67].

4.1.2 Underlying Gaussian CSDM by a Translation Process

In general, the underlying Gaussian CSDM in Eq. (16) can be computed based on a prescribed stationary target CSDM using an iteration-based procedure proposed by Shields et al. [75]. The details of this algorithm are explained briefly in the following five steps.

(1) The first approximation of the underlying Gaussian CSDM, $\mathbf{S}_{G}^{(0)}(\kappa)$, is set to the normalized target non-Gaussian CSDM, $\mathbf{S}_{N}^{T}(\kappa)$:

$$S_{Gij}^{(0)}(\kappa)=\frac{S_{Nij}^{T}(\kappa)}{\sigma_{Ni}\sigma_{Nj}} \tag{34}$$

where the superscript (0) in $\mathbf{S}_{G}^{(0)}(\kappa)$ represents the first iteration and σ_{Ni} is the standard

deviation of vector component *i*.

(2) The corresponding Gaussian cross-correlation matrix (CCM), $\mathbf{R}_G^{(k)}(\kappa)$, is computed from $\mathbf{S}_G^{(k)}(\kappa)$ at the *k*-th iteration using the Wiener-Khintchine transform as follows [83]:

$$R_{Gij}^{(k)}(\tau) = \int_{-\infty}^{\infty} S_{Gij}^{(k)}(\kappa) \exp(\mathrm{I}\kappa\tau)\, d\kappa \tag{35}$$

$\mathbf{R}_G^{(k)}(\kappa)$ is then transformed into the corresponding non-Gaussian CCM, $\mathbf{R}_N^{(k)}(\kappa)$, which is expressed as follows [68]:

$$R_{Nij}^{(k)}(\tau) = \int_{-\infty}^{\infty}\int_{-\infty}^{\infty} F_{Ni}^{-1}\left\{F_{Gi}(x_{i1})\right\} \cdot F_{Nj}^{-1}\left\{F_{Gj}(x_{j2})\right\} \cdot \Phi\left\{x_{i1}, x_{j2}, \rho_{ij}^{(k)}(\tau)\right\} dx_{i1} dx_{j2} \tag{36}$$

where

$$\Phi\left\{x_{i1}, x_{j2}, \rho_{ij}^{(k)}(\tau)\right\} = \frac{1}{2\pi(\sigma_{Gi}\cdot\sigma_{Gj})\sqrt{1-\rho_{ij}^{(k)2}(\tau)}} \cdot \exp\left(-\frac{x_{i1}^2 + x_{j2}^2 - 2\rho_{ij}^{(k)}(\tau)x_{i1}x_{j2}}{2(\sigma_{Gi}\cdot\sigma_{Gj})\left(1-\rho_{ij}^{(k)2}(\tau)\right)}\right) \tag{37}$$

$\Phi\left\{x_{i1}, x_{j2}, \rho_{ij}^{(k)}(\tau)\right\}$ is the joint Gaussian PDF, $\rho_{ij}^{(k)}(\tau)$ is calculated by normalizing $R_{Gij}^{(k)}(\tau)$, $F_{Ni}^{-1}(\cdot)$ is the inverse of the non-Gaussian cumulative distribution function (CDF) of the translation vector component *i* and $F_{Gi}(\cdot)$ is the Gaussian CDF of the translation vector component *i*. Subsequently, the non-Gaussian CSDM $\mathbf{S}_N^{(k)}(\kappa)$ is estimated from $\mathbf{R}_N^{(k)}(\kappa)$ using the Wiener-Khintchine transform as follows:

$$S_{Nij}^{(k)}(\kappa) = \frac{1}{2\pi}\int_{-\infty}^{\infty} R_{Nij}^{(k)}(\tau) \exp(-\mathrm{I}\kappa\tau)\, d\tau \tag{38}$$

(3) All of the CSDMs (i.e., $\mathbf{S}_N^T(\kappa)$, $\mathbf{S}_N^{(k)}(\kappa)$ and $\mathbf{S}_G^{(k)}(\kappa)$) are decomposed using the Cholesky's decomposition, as described in Eqs. (18) to (28). Based on this decomposition of the CSDMs, matrices $\mathbf{H}_N^T(\kappa)$, $\mathbf{H}_N^{(k)}(\kappa)$ and $\mathbf{H}_G^{(k)}(\kappa)$ can be obtained accordingly. Note that $\mathbf{S}_N^T(\kappa)$ is decomposed only once, whereas $\mathbf{S}_N^T(\kappa)$ and $\mathbf{S}_N^{(k)}(\kappa)$ are decomposed at every iteration.

(4) The Gaussian CSDM decomposed at the (*k* + 1)-th iteration, $\mathbf{H}_G^{(k+1)}(\kappa)$ is upgraded

as follows:

$$H_{Gij}^{(k+1)}(\kappa)=\left[\frac{H_{Nij}^{T}(\kappa)}{H_{Nij}^{(k)}(\kappa)}\right]^{\beta}H_{Gij}^{(k)}(\kappa) \tag{39}$$

where β is selected to optimize the convergence speed (i.e., the number of iterations for convergence) and the relative difference between $\mathbf{S}_N^T(\kappa)$ and $\mathbf{S}_N^{(k+1)}(\kappa)$ at the $(k+1)$-th iteration $\boldsymbol{\varepsilon}^{(k+1)}$, as defined in Equation (40). Note that $\boldsymbol{\varepsilon}^{(k+1)}$ is calculated for each iteration to confirm the convergence criterion:

$$\varepsilon_{ij}^{(k+1)}=\sqrt{\frac{\sum_{n=0}^{N-1}\left[S_{Nij}^{(k+1)}(\kappa_n)-S_{Nij}^{T}(\kappa_n)\right]^2}{\sum_{n=0}^{N-1}\left[S_{Nij}^{T}(\kappa_n)\right]^2}} \tag{40}$$

(5) Based on the upgrading using Equation (39), the new Gaussian CSDM, $\mathbf{S}_G^{(k+1)}(\kappa)$, is calculated using Equation (18). Since the upgrading will alter the variance of the underlying Gaussian from the assumed unity, $\mathbf{S}_G^{(k+1)}(\kappa)$ needs to be normalized as follows:

$$S_{Gij}^{N(i+1)}(\kappa)=\frac{S_{Gij}^{(k+1)}(\kappa)}{\sqrt{\int_{-\infty}^{\infty}S_{Gii}^{(k+1)}(\kappa)d\kappa\int_{-\infty}^{\infty}S_{Gjj}^{(k+1)}(\kappa)d\kappa}} \tag{41}$$

where the superscript *N* indicates normalization.

Steps (2) through (5) are repeated using the new estimated Gaussian CSDM, $\mathbf{S}_G^{(k+1)}(\kappa)$, until $\boldsymbol{\varepsilon}^{(k+1)}$ —computed with Equation (40)—meets the convergence criterion.

4.2 Procedure for Simulating the Spatial Steel Weight Loss Distributions of Multiple Rebars in MV Random Fields using SRM

Figure 20 presents a proposed procedure for simulating the steel weight loss of *m* corroded tensile rebars as MV random fields. The procedure is composed of four main parts. Part

1 gathers simulation parameters from a corroded RC member with multiple rebars (i.e., samples of steel weight loss distributions along the rebars, mean values and standard deviations of steel weight loss, and the distribution type), which are obtained from Chapter 3 herein. To simulate MV random fields, two essential functions, the auto-SDF and coherence function, are determined in Part 2 and Part 3, respectively. The detailed procedure to estimate these functions based on the experimental results will be described in Chapter 4.3. Accordingly, the steel weight loss of RC structures with *m* tensile rebars is represented by MV random fields in Part 4 using the method provided in Chapter 4.1.1.

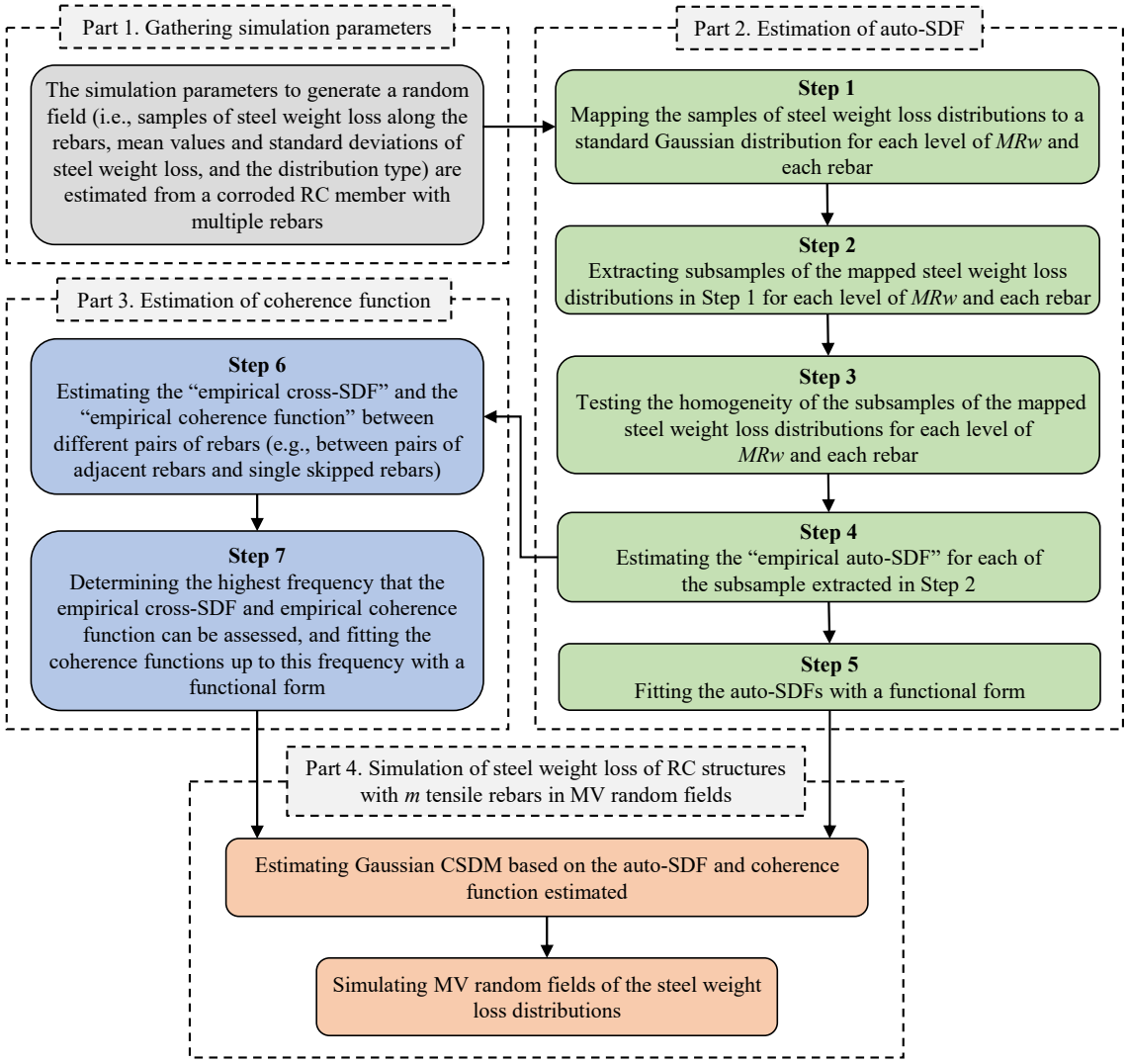

Figure 20 Flowchart for simulating spatial steel weight loss of *m* rebars in MV random fields.

According to Step (VI) of the procedure to simulate MV random fields presented in

Chapter 4.1.1 (i.e., Part 4 in Figure 20), since the experimental results of the steel weight loss distribution is well represented by a lognormal distribution, as stated in Chapter 3, the standard Gaussian samples $\hat{g}_i^{(s)}$ in Eq. (33) are mapped to the desired lognormal distribution [67]:

$$f_i^{(s)}(x) = \exp\left[MRw_{YS,i} + \sigma_{YS,i}\hat{g}_i^{(s)}(x) \right] \tag{42}$$

where

$$\sigma_{YS,i}^2 = \ln\left(1 + \frac{{\sigma_{S,i}}^2}{{MRw_{S,i}}^2} \right), \quad MRw_{YS,i} = \ln(MRw_{S,i}) - \frac{1}{2}\sigma_{YS,i}^2 \tag{43}$$

and $MRw_{S,i}$ and $\sigma_{S,i}$ are the mean value and standard deviation, respectively, of the localized steel weight loss in a single rebar i, which can be obtained from the experimental results.

4.3 Estimation of the Auto-SDF and Coherence Function

Using the experimental results of the steel weight loss in the RC slab specimen presented in Chapter 3, the auto-SDF $S_{ii}(\kappa)$ and coherence function $\gamma_{ij}(\kappa)$ in Eqs. (16) and (17) are estimated, respectively. With the results of $S_{ii}(\kappa)$ and $\gamma_{ij}(\kappa)$, the longitudinal and transverse correlation of steel weight loss can be represented. Due to the limitation in the number of specimens, it is not possible to estimate these functions entirely empirically. Instead, a functional form needs to be selected based on physical considerations, and the experimental data can be used to calibrate the functional forms of the auto-SDF and coherence function.

Steps 1 to 5 and Steps 6 and 7 shown in Figure 20 comprise the procedure for determining the auto-SDF and coherence function, respectively. The various steps of the proposed procedure are described in detail in the following (the numbers of Steps 1 to 7 in Figure 20 correspond to the numbering of the subchapters that follow).

4.3.1 Mapping Steel Weight Loss Samples $Rw_i(u)$ to Standard Gaussian Samples $Rw_{G,i}(u)$

The $Rw_i(u)$ samples from rebar *i* are mapped from a lognormal distribution to a standard Gaussian distribution for each corrosion level (i.e., *MRw* = 4.10%, 7.88%, 15.73% and 18.84%) using the classic Nataf transformation [67]:

$$Rw_{G,i}(u) = F_{Rw_{G,i}}^{-1}\left\{F_{Rw_i}\left[Rw_i(u)\right]\right\} \tag{44}$$

where $Rw_{G,i}(u)$ are the standard Gaussian mapped samples of steel weight loss, $F_{Rw_{G,i}}^{-1}$ is the inverse Gaussian cumulative distribution function (CDF) of rebar *i*, and F_{Rw_i} is the lognormal CDF with mean value $MRw_{S,i}$ and standard deviation $\sigma_{S,i}$, where $\sigma_{S,i}$ is provided by

$$\sigma_{S,i} = \sqrt{\frac{1}{M}\sum_{u=1}^{M}(Rw_i(u) - MRw_{S,i})^2} \tag{45}$$

The results of the standard Gaussian mapped samples of steel weight loss $Rw_{G,i}$ for all the corrosion levels are presented in Figure 21. To compare the distribution of $Rw_{G,i}$ with the standard Gaussian distribution, the normal probability plots of the samples $Rw_{G,i}$ for all the corrosion levels are displayed in Figure 22. As shown in Figure 22, the results indicate good fit of the samples $Rw_{G,i}$ to the theoretical distribution (i.e., standard Gaussian distribution), especially at significant corrosion levels e.g., *MRw* = 15.73% and 18.84%.

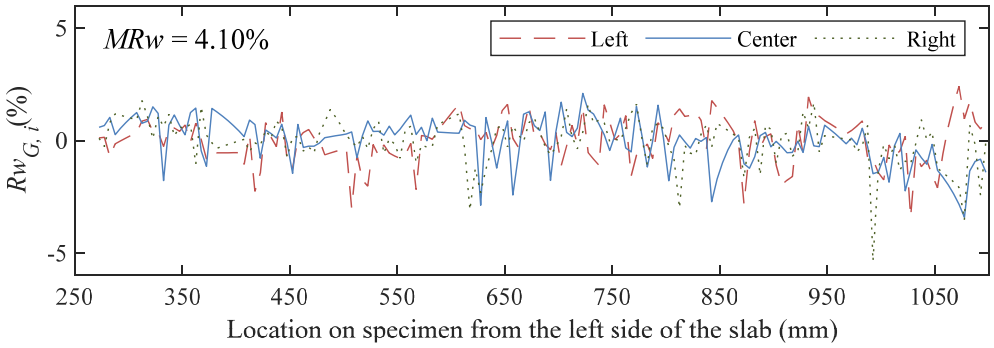

(a) Mapped samples $Rw_{G,i}$ at 1st X-ray, MRw = 4.10%

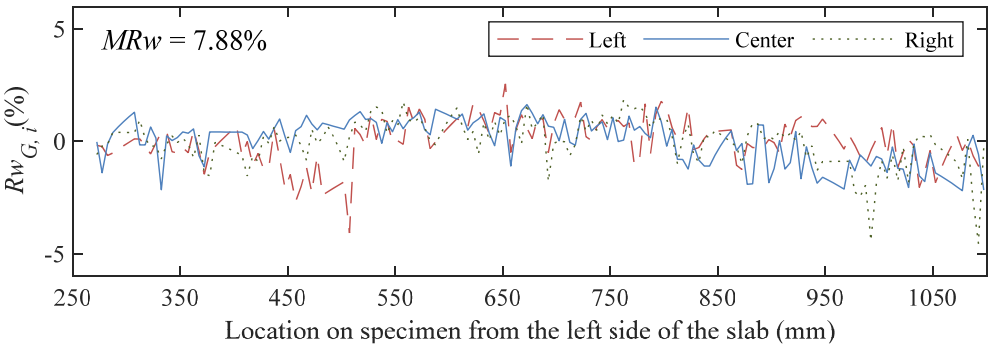

(b) Mapped samples $Rw_{G,i}$ at 2nd X-ray, MRw = 7.88%

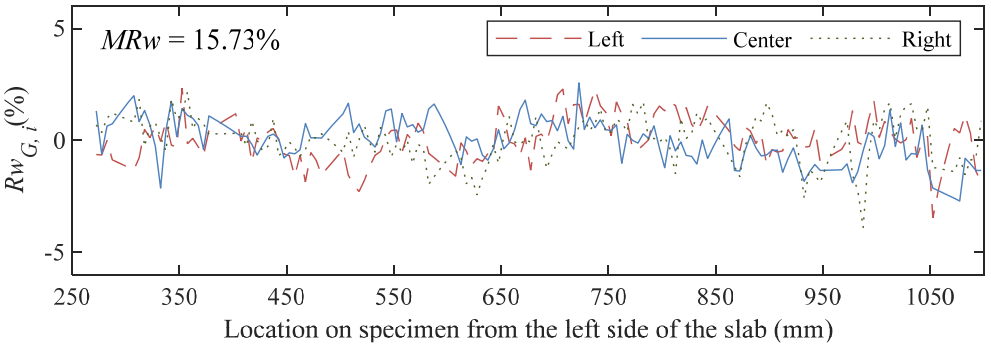

(c) Mapped samples $Rw_{G,i}$ at 3rd X-ray, MRw = 15.73%

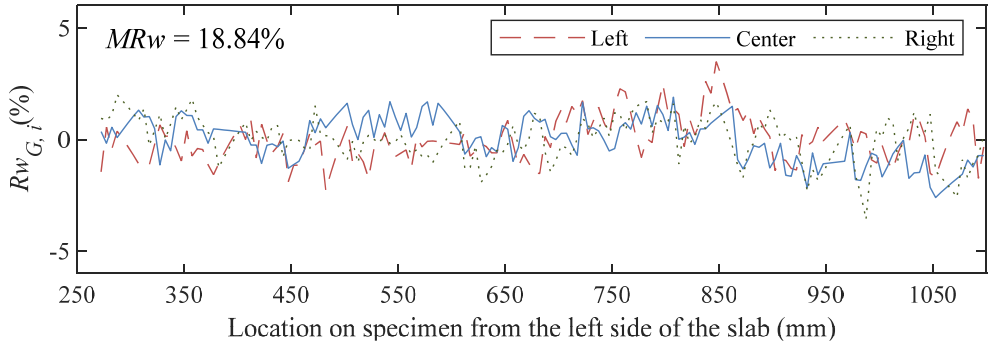

(d) Mapped samples $Rw_{G,i}$ at 4th X-ray, MRw = 18.84%

Figure 21 Mapped samples $Rw_{G,i}$ at each corrosion level: (a) 1st X-ray, MRw = 4.10%; (b) 2nd X-ray, MRw = 7.88%; (c) 3rd X-ray, MRw = 15.73%; and (d) 4th X-ray, MRw = 18.84%.

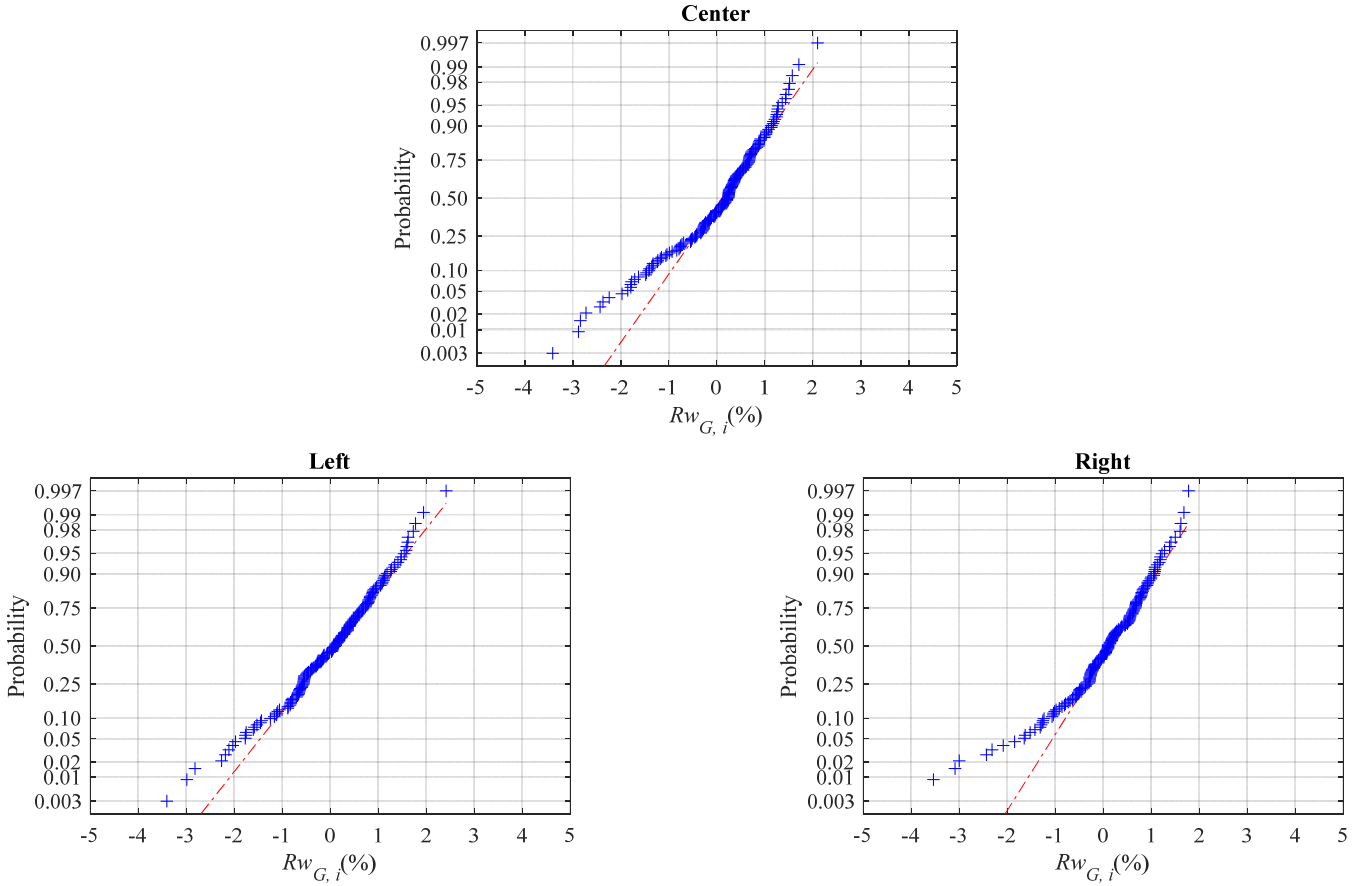

(a) Normal probability plot of samples $Rw_{G,i}$ for three tensile rebars at 1st X-ray, MRw = 4.10%

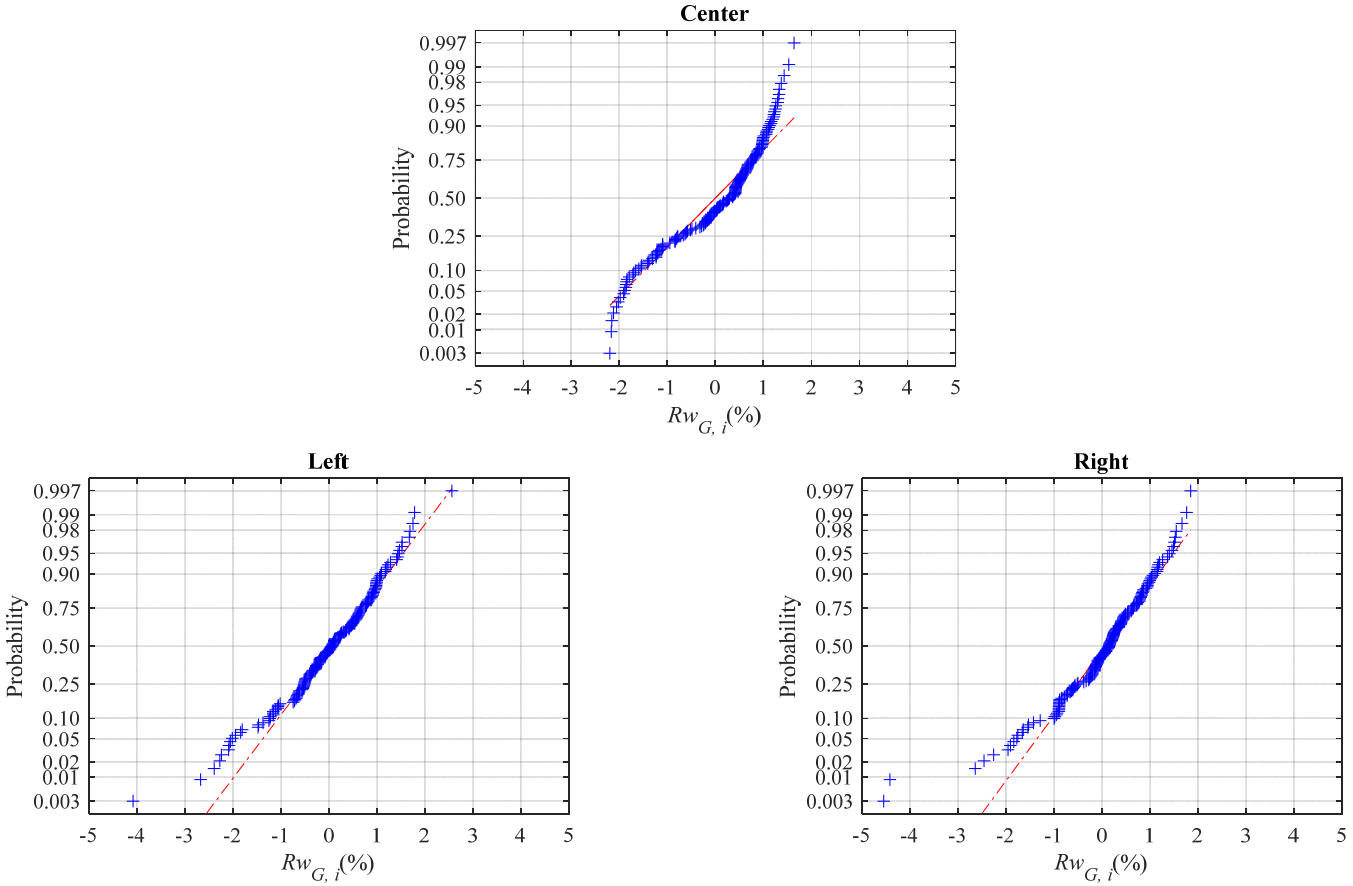

(b) Normal probability plot of samples $Rw_{G,i}$ for three tensile rebars at 2nd X-ray, MRw = 7.88%

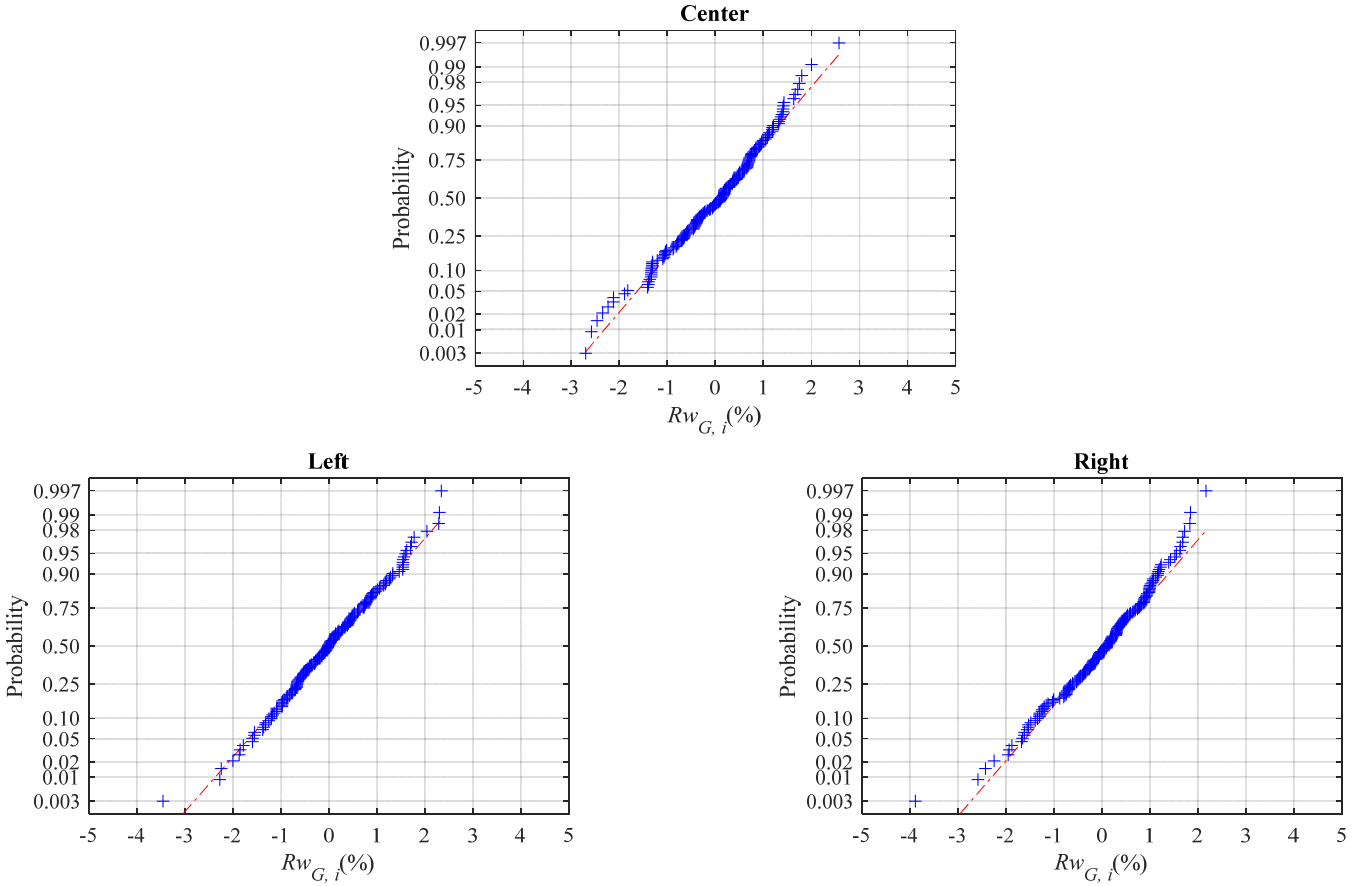

(c) Normal probability plot of samples $Rw_{G,i}$ for three tensile rebars at 3rd X-ray, MRw = 15.73%

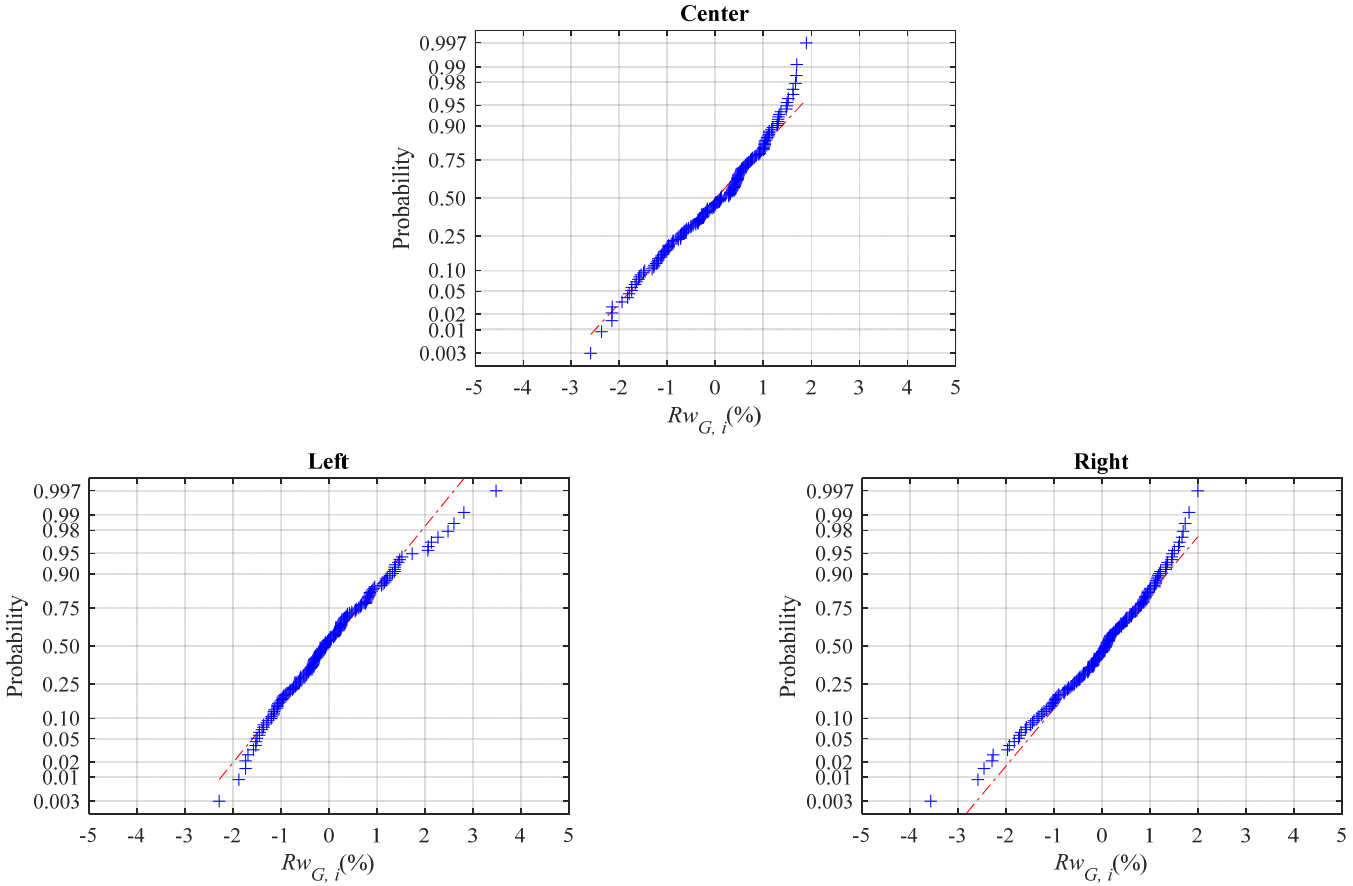

(d) Normal probability plot of samples $Rw_{G,i}$ for three tensile rebars at 4th X-ray, MRw = 18.84%

Figure 22 Normal probability plot of samples $Rw_{G,i}$ for three tensile rebars (i.e., Left, Center and Right) at each corrosion level: (a) 1st X-ray, MRw = 4.10%; (b) 2nd X-ray, MRw = 7.88%; (c) 3rd X-ray, MRw = 15.73%; and (d) 4th X-ray, MRw = 18.84%.

4.3.2 Extracting Subsamples $Rw_{G,i,k}(u)$

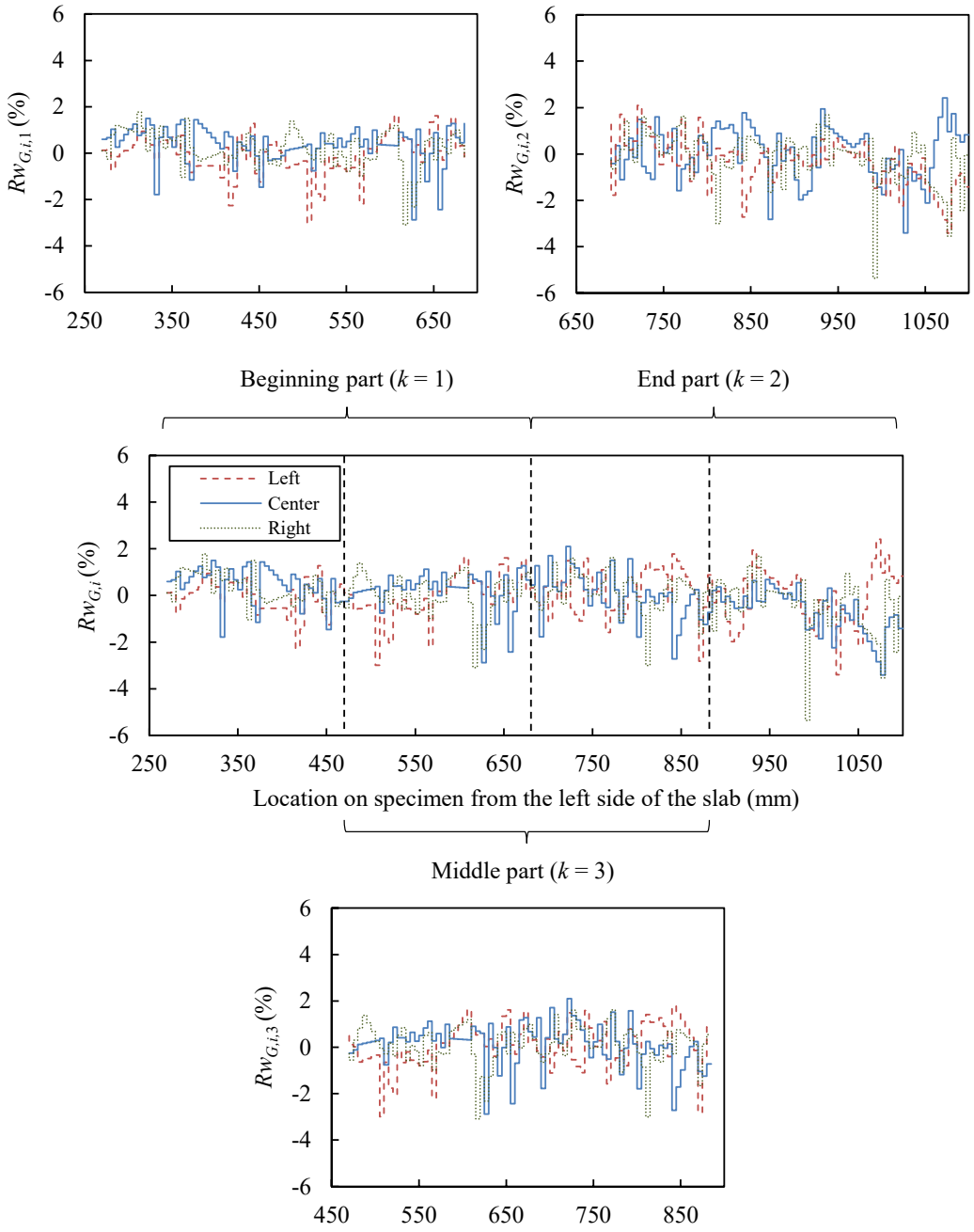

Figure 23 Example extraction of samples $Rw_{G,i,k}(u)$ from the measurement results of the 1st X-ray (MRw = 4.10%).

For each corrosion level and rebar, from the mapped samples $Rw_{G,i}(u)$, three subsamples $Rw_{G,i,k}(u)$ are extracted, where k = 1, 2 and 3 represent the beginning, end and middle of

the $Rw_{G,i}(u)$ field, respectively. Figure 23 illustrates an example of the extraction of the samples $Rw_{G,i,k}(u)$ from the measurement result of the 1st X-ray (MRw = 4.10%).

4.3.3 Homogeneity Testing of Subsamples $Rw_{G,i,k}(u)$

Before applying the mapped samples $Rw_{G,i,k}(u)$ that were extracted in the previous step to estimate the functional form of the auto-SDF, a homogeneity test is performed by considering the mean value $MRw_{G,i,k}$ and standard deviation $\sigma_{G,i,k}$ of each subsample of the mapped steel weight loss distributions $Rw_{G,i,k}(u)$ as

$$MRw_{G,i,k} = \frac{1}{Q}\sum_{u=1}^{Q} Rw_{G,i,k}(u) \tag{46}$$

$$\sigma_{G,i,k} = \sqrt{\frac{1}{Q}\sum_{u=1}^{Q}(Rw_{G,i,k}(u) - MRw_{G,i,k})^2} \tag{47}$$

where Q is the total number of discrete locations in a subsample $Rw_{G,i,k}(u)$.

Notably, the results of the homogeneity testing shown in Table 3 indicate that $MRw_{G,i,k}$ and $\sigma_{G,i,k}$ match the statistical characteristics of the standard Gaussian distribution (i.e., the mean value and standard deviation are equal to 0 and 1, respectively) and are approximately equivalent among the three subsamples for all three rebars and four corrosion levels. Thus, it is reasonable to assume that the samples extracted in Step 2 (i.e., Chapter 4.3.2) are homogeneous in the mean value and in the standard deviation. In practice, most homogeneous random fields (and stationary processes) are also ergodic; therefore, herein, it is assumed that the field is ergodic. This enables the assessment of the properties of MV random fields (e.g., auto-SDF and coherence) from the results of the

single experimental test that was performed.

Table 3. Means and standard deviations of subsamples of the mapped steel weight loss distributions.

Corrosion level	Rebar	$MRw_{G,i,k}$ (%)			$\sigma_{G,i,k}$ (%)		
		Beginning part (k = 1)	End part (k = 2)	Middle part (k = 3)	Beginning part (k = 1)	End part (k = 2)	Middle part (k = 3)
1st X-ray (MRw = 4.10%)	Left (i = 1)	-0.07	0.07	0.07	0.86	0.99	1.13
	Center (i = 2)	0.35	0.13	-0.37	0.80	0.93	1.14
	Right (i = 3)	0.20	0.08	-0.20	0.80	0.90	1.14
2nd X-ray (MRw = 7.88%)	Left (i = 1)	-0.15	0.35	0.13	1.13	1.07	0.83
	Center (i = 2)	0.52	0.47	-0.54	0.65	0.77	1.18
	Right (i = 3)	0.22	0.53	-0.25	0.69	0.70	1.18
3rd X-ray (MRw = 15.73%)	Left (i = 1)	-0.36	0.16	0.35	0.86	1.07	1.01
	Center (i = 2)	0.45	0.29	-0.47	0.76	0.77	1.12
	Right (i = 3)	-0.01	-0.11	0.00	0.87	0.87	1.12
4th X-ray (MRw = 18.84%)	Left (i = 1)	-0.43	0.29	0.44	0.65	1.13	1.09
	Center (i = 2)	0.41	0.51	-0.43	0.73	0.73	1.15
	Right (i = 3)	0.10	0.03	-0.11	0.81	0.84	1.15

4.3.4 Estimating Empirical Gaussian Auto-SDFs $S_{EG,ii,k}(\kappa)$

For each subfield obtained from Step 2 (i.e., Chapter 4.3.2), the "empirical auto-SDF" is estimated by [83]:

$$S_{EG,ii,\mathrm{k}}(\kappa) = \frac{1}{2\pi T}\overline{Rw_{G,i,k}(u)}^{*} \cdot \overline{Rw_{G,i,k}(u)} \tag{48}$$

where

$T = Q\Delta x$,

$\overline{Rw_{G,i,k}(u)}$ is the Fourier transform of $Rw_{G,i,k}(u)$, and Q is the total number of locations in a subsample of $Rw_{G,i,k}(u)$.

Figure 24 shows the empirical auto-SDF for the subfields obtained from Step 2, $S_{EG,ii,k}(\kappa)$ at all the corrosion levels. Figure 25 presents the results of the average $S_{EG,ii,k}(\kappa)$ calculated for each corrosion level. These results reveal that there is no distinct relationship between $S_{EG,ii,k}(\kappa)$ and the corrosion level. Therefore, it is assumed that a single auto-SDF is analyzed and applied for any single rebar using the total average $S_{EG,ii,k}(\kappa)$ calculated from all the corrosion levels. Note that this is possible because the effects of the different mean and standard deviation associated with each corrosion level are accounted for by the mapping in Eq. (42).

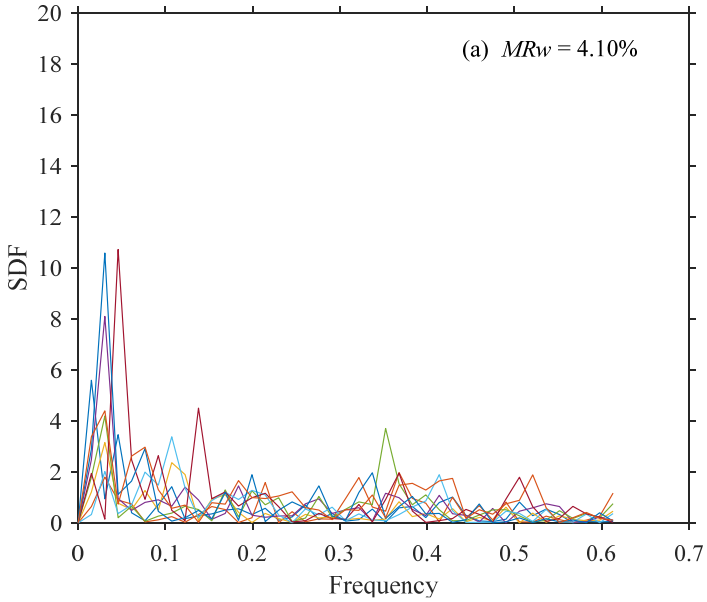

(a) Empirical auto-SDF for subfields, $S_{EG,ii,k}(\kappa)$ at 1st X-ray, $MRw = 4.10\%$

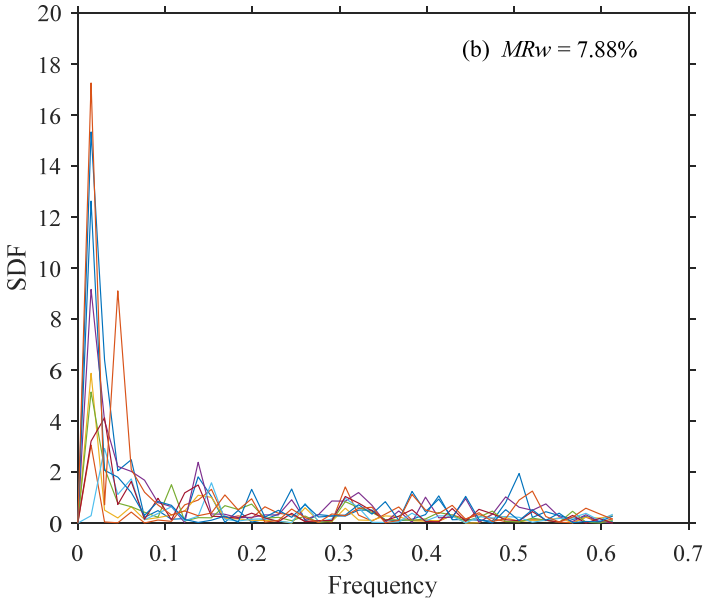

(b) Empirical auto-SDF for subfields, $S_{EG,ii,k}(\kappa)$ at 2nd X-ray, $MRw = 7.88\%$

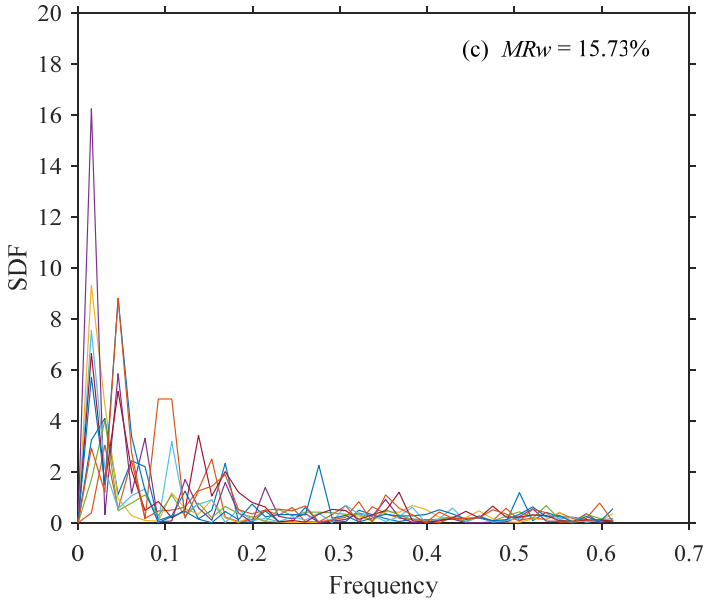

(c) Empirical auto-SDF for subfields, $S_{EG,ii,k}(\kappa)$ at 3rd X-ray, MRw = 15.73%

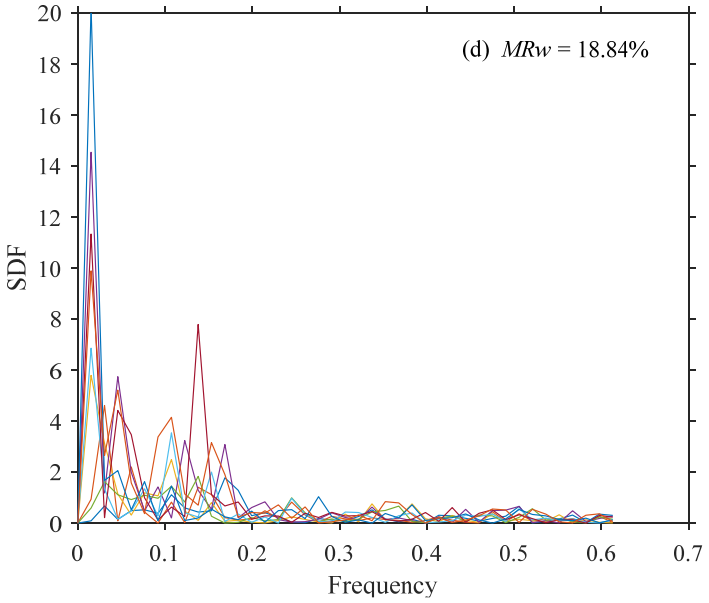

(d) Empirical auto-SDF for subfields, $S_{EG,ii,k}(\kappa)$ at 4th X-ray, MRw = 18.84%

Figure 24 Empirical auto-SDF for the subfields obtained from Step 2, $S_{EG,ii,k}(\kappa)$ at each corrosion level: (a) 1st X-ray, MRw = 4.10%; (b) 2nd X-ray, MRw = 7.88%; (c) 3rd X-ray, MRw = 15.73%; and (d) 4th X-ray, MRw = 18.84%.

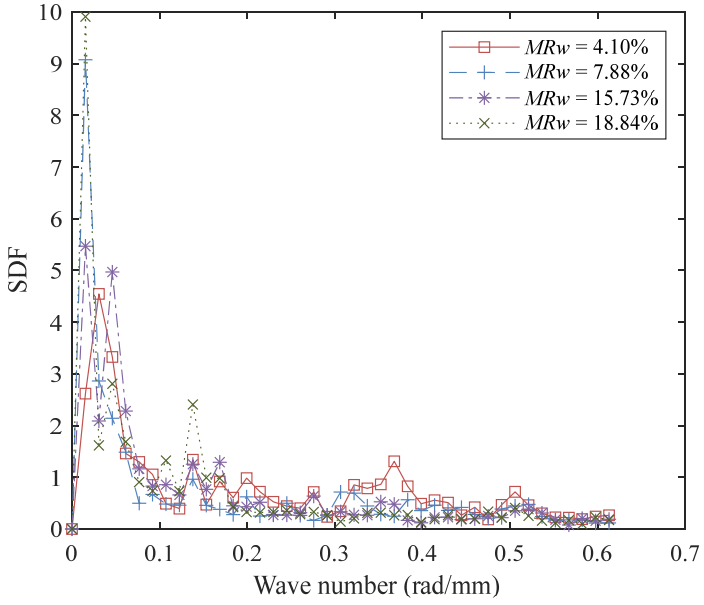

Figure 25 Average $S_{EG,ii,k}(\kappa)$ at each corrosion level.

4.3.5 Fitting $S_{EG,ii,k}(\kappa)$ with a Functional Form

An array of functional forms is tested to capture the auto-SDF of the steel weight loss. According to the general tendency of the average $S_{EG,ii,k}(\kappa)$ shown in Figure 25, three possible functional forms presented in Table 4 are tested to capture the spectrum. Notably, when selecting the functional form, special emphasis is given to the ability to capture the spectrum at low wavenumbers because the fluctuations at high wavenumbers (i.e., short periods) in the experimental results may be generated by measurement errors and are less reliable than the fluctuations at small wavenumbers (i.e., long periods).

The fitted parameters for each functional form (i.e., C_1 and/or C_2) are estimated using a least square regression on the experimental data. The results of the coefficient of determination (R^2) indicate that functional form No. 3 in Table 4 best captures the spectrum with the parameters $C_1 = 0.0063$ and $C_2 = 5.7$ for the longitudinal correlation. Figure 26 shows a comparison of the total average $S_{EG,ii,k}(\kappa)$ and the fitted function

$S_{FG}(\kappa)$ using the parameters C_1 and C_2. As shown, these two results yield good characterizations between the measured and functional spectra at low wavenumbers, where $R^2 = 0.85$. Even though the fitting is inconsistent at high wavenumber (> 0.1 rad/mm), the results at the low wavenumber (0 – 0.1 rad/mm), which is important parts for representing the longitudinal correlation, are satisfactory fitted with the functional form. Therefore, $S_{ii}(\kappa)$ of a single rebar *i* in Eqs. (16) and (17) can be well represented by the functional auto-SDF, $S_{FG}(\kappa)$, with $C_1 = 0.0063$ and $C_2 = 5.7$ to consider the longitudinal correlation of a steel weight loss distribution.

Table 4. List of functional forms utilized to capture the auto-SDF of the steel weight loss.

No.	Functional form S_{FG}	Fitted parameters	Coefficient of determination R^2
1	$S_{FG}(\kappa) = \frac{1}{4} C_1^3 \kappa^2 \exp(-C_1 \lvert\kappa\rvert)$	$C_1 = 45.12$	−0.25
2	$S_{FG}(\kappa) = C_1 C_2 (C_1 + C_2)\left[\pi (C_1^2 + \kappa^2)(C_2^2 + \kappa^2)\right]^{-1}$	$C_1 = 9094$, $C_2 = 0.0991$	0.48
3	$S_{FG}(\kappa) = \frac{\left[1 + 40000 C_2^2 (\kappa / C_1)^2\right](\kappa / C_1)^4}{\left[(1 - \lvert\kappa\rvert / C_1)^4 + 4 C_2 (\kappa / C_1)^2\right]\left[(1 - 10\lvert\kappa\rvert / C_1)^4 + 400 C_2 (\kappa / C_1)^2\right]}$	$C_1 = 0.0063$, $C_2 = 5.7$	0.85

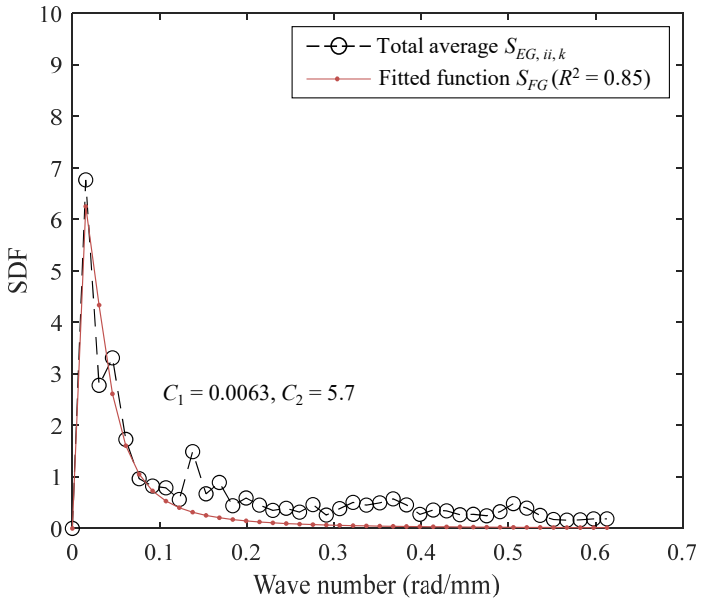

Figure 26 Fitting the total average $S_{EG,ii,k}(\kappa)$ calculated from all the corrosion levels.

4.3.6 Estimating Empirical Coherence Functions $\gamma_{EG,ij,k}(\kappa)$

At the beginning of the procedure to determine the coherence function $\gamma_{ij}(\kappa)$ used in Eq. (17) based on the experimental results in Chapter 3, the "empirical coherence functions" $\gamma_{EG,ij,k}$ between two pairs of adjacent rebars (i.e., $\gamma_{EG,12,k}$ and $\gamma_{EG,23,k}$ for the pair of rebars 1 and 2 and pair of rebars 2 and 3, respectively) and a pair of single skipped rebars (i.e., $\gamma_{EG,13,k}$ for the pair of rebars 1 and 3) are estimated for each subfield k and each corrosion level.

In particular, $\gamma_{EG,ij,k}$ can be calculated by inverting Eq. (17) and using the empirical auto- and cross-SDF as

$$\gamma_{EG,ij,k}(\kappa) = \frac{S_{EG,ij,k}(\kappa)}{\sqrt{S_{EG,ii,k}(\kappa) S_{EG,jj,k}(\kappa)}} \tag{49}$$

where $S_{EG,ii,k}(\kappa)$ is the empirical auto-SDF estimated by Eq. (48), and the "empirical cross-SDF", $S_{EG,ij,k}(\kappa)$ can be estimated as follows [83]:

$$S_{EG,ij,k}(\kappa)=\frac{1}{2\pi T}\left|\overline{Rw_{G,i,k}(u)}^{*}\cdot\overline{Rw_{G,j,k}(u)}\right| \tag{50}$$

Figure 27 shows the results of the average $\gamma_{EG,ij,k}$ that is calculated from the three subsamples (i.e., k = 1, 2 and 3) at each corrosion level. Additionally, in this case, the values associated with large wavenumbers (i.e., larger than 0.05 rad/mm) and short periods are affected by potential aliasing and measurement errors and can be disregarded to focus on the first part of the data (i.e., wavenumbers smaller than 0.05 rad/mm). The initial decay and its speed are similar for all corrosion levels, with only a couple of exceptions. Therefore, as for the auto-SDF, a single functional form is assessed for the coherence at all corrosion levels.

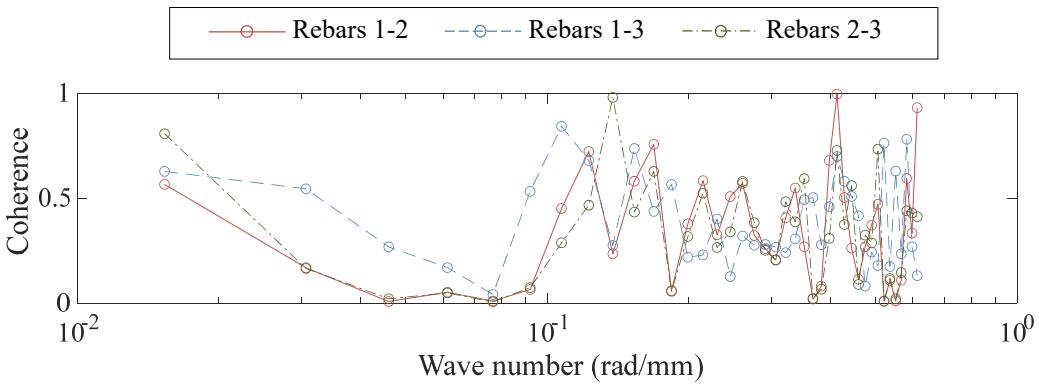

(a) Average empirical coherence functions, $\gamma_{EG,ij,k}$ at 1st X-ray, MRw = 4.10%

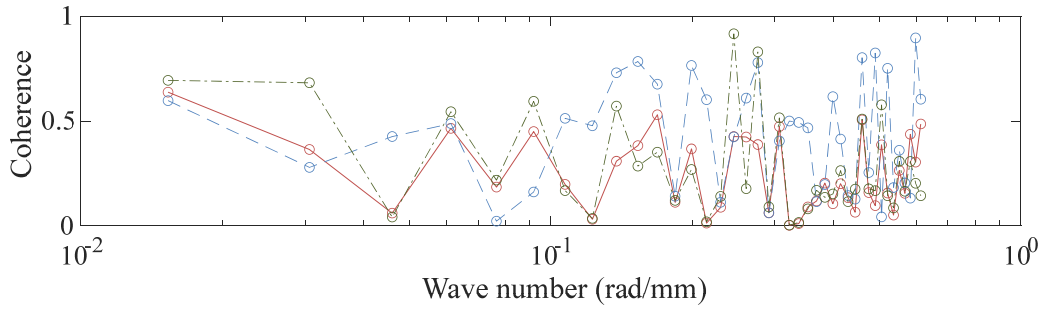

(b) Average empirical coherence functions, $\gamma_{EG,ij,k}$ at 2nd X-ray, MRw = 7.88%

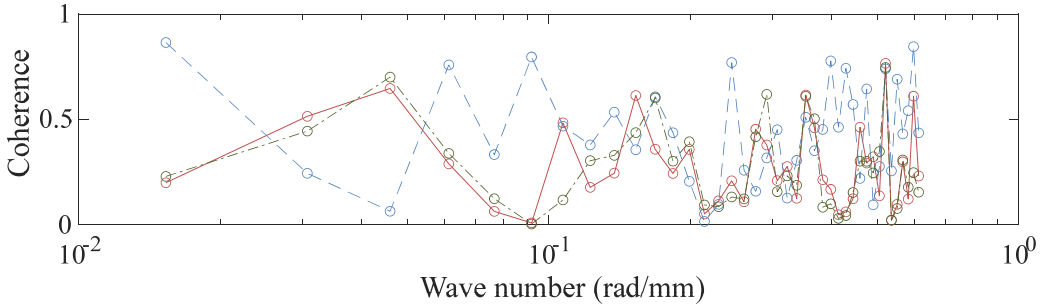

(c) Average empirical coherence functions, $\gamma_{EG,ij,k}$ at 3rd X-ray, MRw = 15.73%

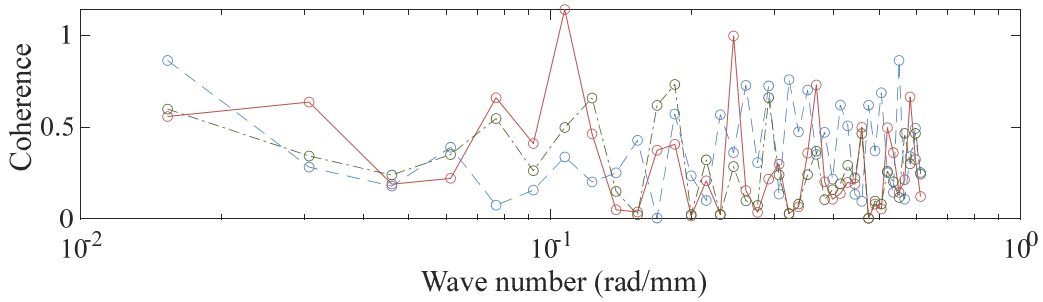

(d) Average empirical coherence functions, $\gamma_{EG,ij,k}$ at 4th X-ray, MRw = 18.84%

Figure 27 Average empirical coherence functions, $\gamma_{EG,ij,k}$, calculated from the three subsamples (i.e., k = 1, 2 and 3) at each corrosion level: (a) 1st X-ray, MRw = 4.10%; (b) 2nd X-ray, MRw = 7.88%; (c) 3rd X-ray, MRw = 15.73%; and (d) 4th X-ray, MRw = 18.84%.

4.3.7 Fitting $\gamma_{EG,ij,k}(\kappa)$ with a Functional Form

Based on the coherence functions in Figure 27, a negative exponential functional form is

selected:

$$\gamma_{FG,ij}(\kappa) = \exp\left(-\frac{\kappa\sqrt{d_{ij}}}{2\pi C_3}\right) \tag{51}$$

where $\gamma_{FG,ij}(\kappa)$ represents the functional coherence function between rebars i and j, d_{ij} represents the distance between rebars i and j, and C_3 is an estimated parameter that tunes the initial decay. This functional form can describe the coherence for all pairs of rebars considering the different distances between the rebars in the RC slab specimens.

With regard to relevant points of the coherence functions, which can be utilized to fit the functional form, the smallest distance between two measured points in two different rebars across the RC slab specimen determines the highest wavenumber with which the empirical cross-SDF and empirical coherence function can be assessed. Based on Nyquist's theorem, these highest frequencies can be estimated by [83]

$$\kappa_{\text{max cross-SDF}} = \frac{\pi}{\Delta x} \tag{52}$$

Using Eq. (52), the highest frequencies that can be assessed for the pairs of adjacent rebars (i.e., rebars 1 and 2 and rebars 2 and 3) and the pair of single skipped rebars (i.e., rebars 1 and 3) are $\pi/57 = 0.055$ rad/mm and $\pi/114 = 0.028$ rad/mm, respectively. The empirical values of the coherences in Figure 27 beyond these wavenumbers are essentially noise and should be discarded. Figure 28 presents the fitting of the average $\gamma_{EG,ij,k}$ based on the remaining points, with the functional coherence function in Eq. (51). Note that for fitting the coherence functions of the adjacent rebars, the average $(\gamma_{EG,12,k} + \gamma_{EG,23,k})/2$ is used, assuming the coherence function between the pairs of rebars

1 and 2 is equal to that between the pairs of rebars 2 and 3. As confirmed in Figure 28, all the fitted parameters C_3 are similar and thus are independent of the corrosion level. It should be noted that only the average coherence function for adjacent rebars at the 3rd X-ray in Figure 28(c) reveals a different trend from that of the corresponding fitted curve. This difference could occur due to the uncertainties associated with the corrosion process. Therefore, the mean value of all the fitted parameters C_3 shown in Figure 28, which is 0.05, is applied for the simulation. While this value is a good estimate for this study and is recommended for practical applications, additional experiments are needed to confirm or refine this assessment.

Figure 29 shows an example of the functional coherence functions $\gamma_{FG,ij}$ of the RC slab specimen using $d_{12} = d_{23} = 57$ mm for $\gamma_{FG,12}$ and $\gamma_{FG,23}$ and $d_{13} = 114$ mm for $\gamma_{FG,13}$, given $C_3 = 0.05$. Assuming $\gamma_{ij} = \gamma_{FG,ij}$ ($C_3 = 0.05$), the transverse correlation of steel weight loss among the rebars can be taken into account in the simulation.

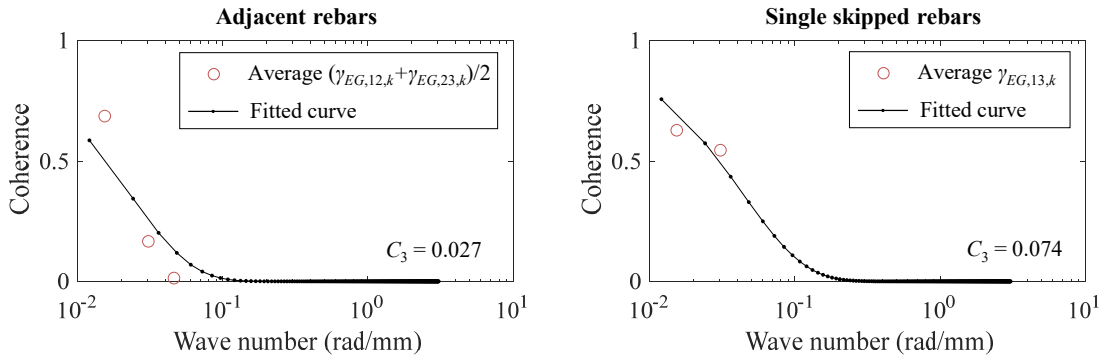

(a) Fitting the average empirical coherence functions, $\gamma_{EG,ij,k}$ at 1st X-ray, $MRw = 4.10\%$

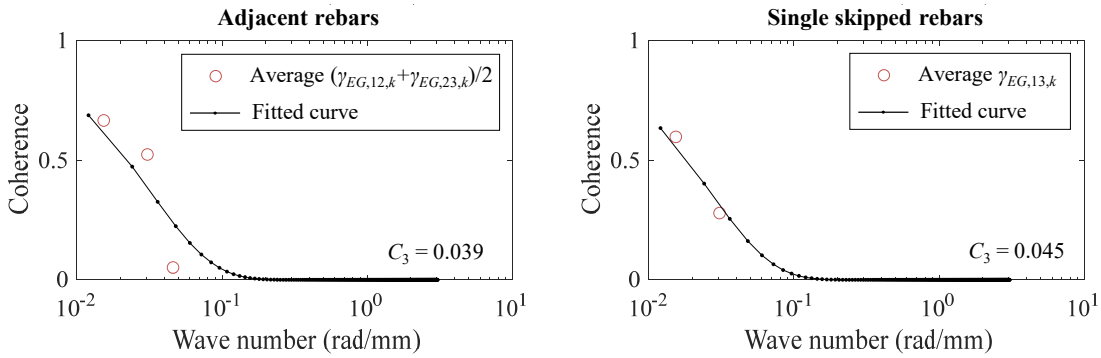

(b) Fitting the average empirical coherence functions, $\gamma_{EG,ij,k}$ at 2nd X-ray, MRw = 7.88%

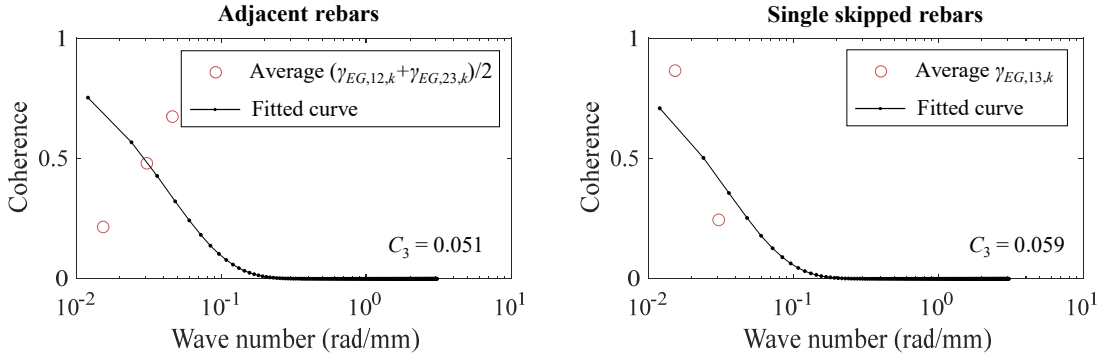

(c) Fitting the average empirical coherence functions, $\gamma_{EG,ij,k}$ at 3rd X-ray, MRw = 15.73%

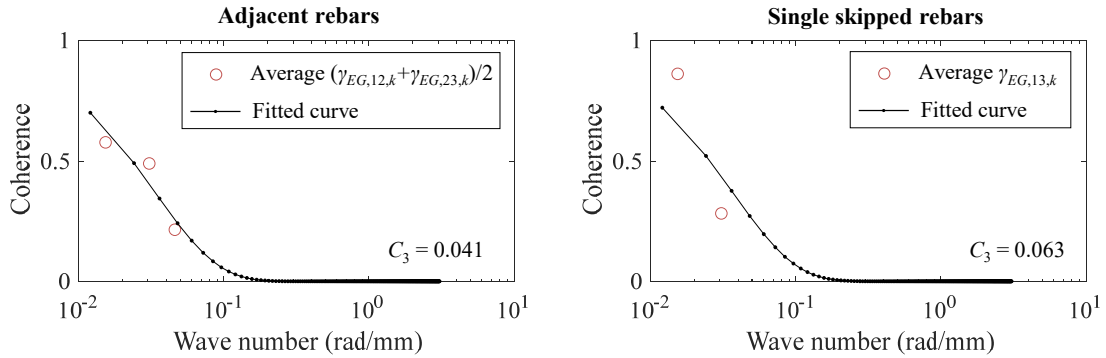

(d) Fitting the average empirical coherence functions, $\gamma_{EG,ij,k}$ at 4th X-ray, MRw = 18.84%

Figure 28 Fitting the average empirical coherence functions, $\gamma_{EG,ij,k}$, calculated from the three subsamples at each corrosion level: (a) 1st X-ray, MRw = 4.10%; (b) 2nd X-ray, MRw = 7.88%; (c) 3rd X-ray, MRw = 15.73%; and (d) 4th X-ray, MRw = 18.84%.

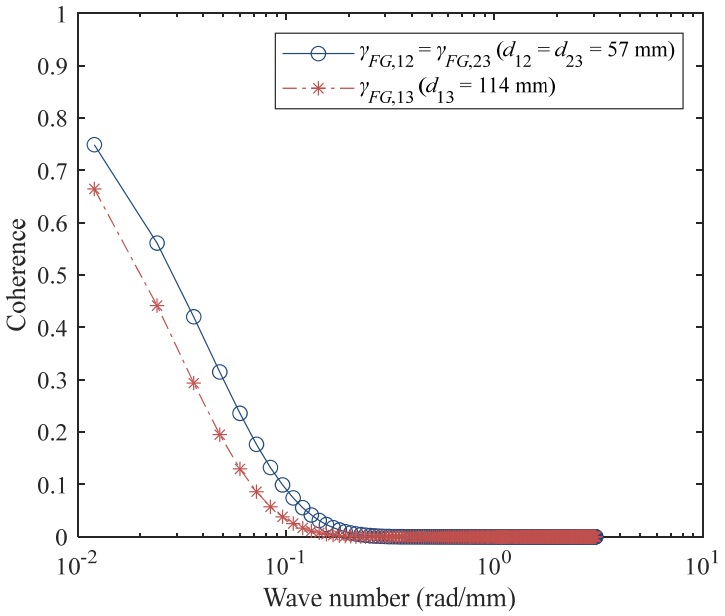

Figure 29 Example of functional coherence functions, $\gamma_{FG,ij}$, of the RC slab specimen between the two pairs of adjacent rebars and the pair of single skipped rebars using the parameter $C_3 = 0.05$.

The auto-SDF and the coherence estimated based on the procedure proposed herein are associated with the so-called "underlying Gaussian field" [71] because a preliminary mapping of the experimental results to a standard Gaussian field was performed. This is important because it prevents the need to identify the underlying Gaussian CSDM, as described in Chapter 4.1.2, and makes the simulation more straightforward.

4.4 Example of Simulated Spatial Steel Weight Loss Distributions for the RC Slab Specimen

Using the functional auto-SDF and functional coherence function, a numerical example of the simulation of spatial steel weight loss distributions in the RC specimen is presented. Since the experimental results of steel weight loss distributions presented in Figure 17 indicate that the locations of rebars i.e., outside rebars (left and right rebars) and inside

rebar (center rebar) have no effect on the corrosion level, the steel weight loss distributions are simulated herein assuming that the steel weight loss distribution for each rebar has the same $MRw_{S,i}$, i.e., $MRw_{S,i}$ (i = 1, 2,…, m) = MRw. With this assumption, $\sigma_{S,i}$ of the steel weight loss distribution of a single rebar in Eq. (43) can be estimated by Eq. (45) for any specific MRw. To determine the relationship between MRw and $\sigma_{S,i}$, steel weight loss distributions of nine RC specimens reported in [17] are utilized. Figure 30 shows that MRw increases with $\sigma_{S,i}$. In the following example, $\sigma_{S,i}$ is estimated by the linear regression shown in Figure 30. Note that only a few steel weight loss distributions with an MRw value greater than 20% were obtained from the experimental data. Further research is needed to understand the steel corrosion phenomena of RC members with higher MRw values.

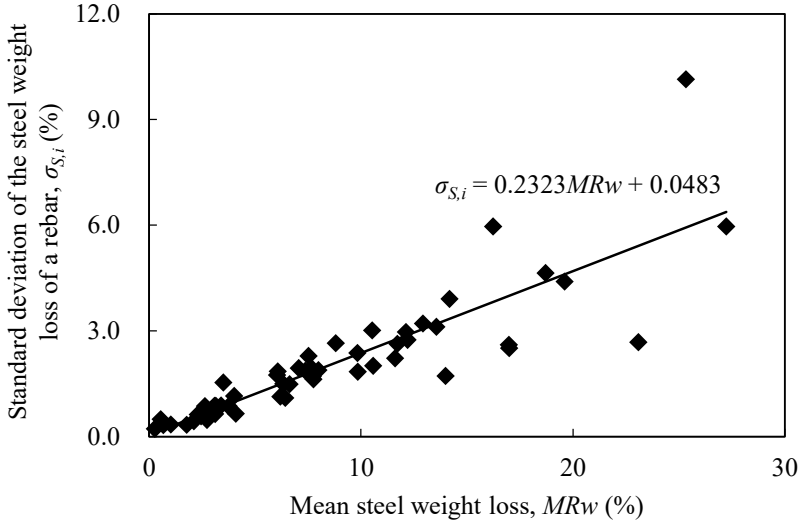

Figure 30 Relationship between MRw and $\sigma_{S,i}$.

Since the RC slab has three tensile rebars (i.e., m = 3), the Gaussian CSDM in Eq. (16) can be provided by

$$\mathbf{S}(\kappa)=\begin{bmatrix} S_{FG}(\kappa) & \gamma_{FG,12}(\kappa)\cdot S_{FG}(\kappa) & \gamma_{FG,13}(\kappa)\cdot S_{FG}(\kappa) \\ \gamma_{FG,21}(\kappa)\cdot S_{FG}(\kappa) & S_{FG}(\kappa) & \gamma_{FG,23}(\kappa)\cdot S_{FG}(\kappa) \\ \gamma_{FG,31}(\kappa)\cdot S_{FG}(\kappa) & \gamma_{FG,32}(\kappa)\cdot S_{FG}(\kappa) & S_{FG}(\kappa) \end{bmatrix} \tag{53}$$

Figures 31(a) and (b) show the effect of the transverse correlation parameter C_3 on the spatial steel weight loss distributions in the RC specimen, assuming $MRw = 10\%$. Two degrees of parameter C_3 are applied in the simulation as follows:

1) Low transverse correlation (i.e., $C_3 = 0.005$) (refer to Figure 31(a)).

2) Experimental transverse correlation (i.e., $C_3 = 0.05$) (refer to Figure 31(b)).

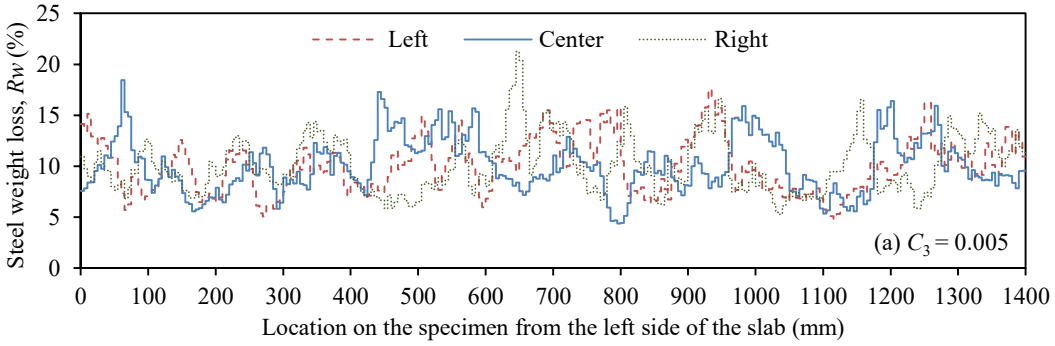

(a)

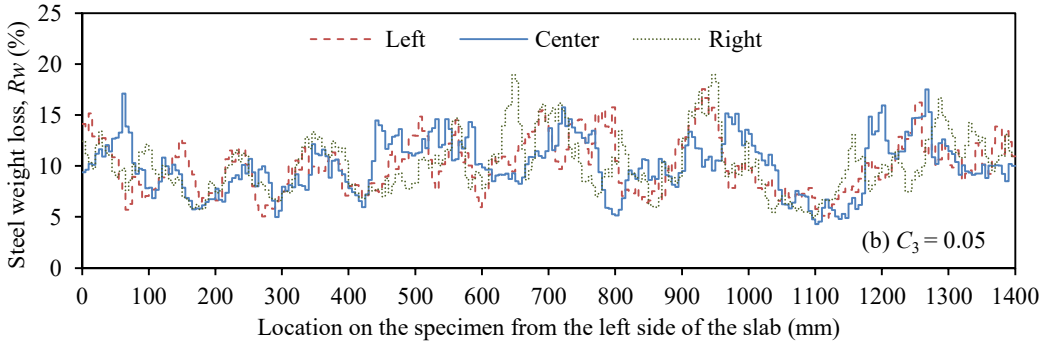

(b)

Figure 31 Effect of the transverse correlation parameter C_3 on the spatial steel weight loss distributions in the RC slab shown in Figure 11, assuming $MRw = 10\%$.

As expected, the transverse correlation among the steel weight loss distributions of

the three tensile rebars depends on the transverse correlation parameter C_3. By applying the SRM to simulate the spatial steel weight loss distributions in MV random fields, the effect of the interaction of corrosion pits among tensile rebars can be considered.

4.5 Structural Performance Assessment Using 3D Nonlinear FE Analysis and the Response Surface Method

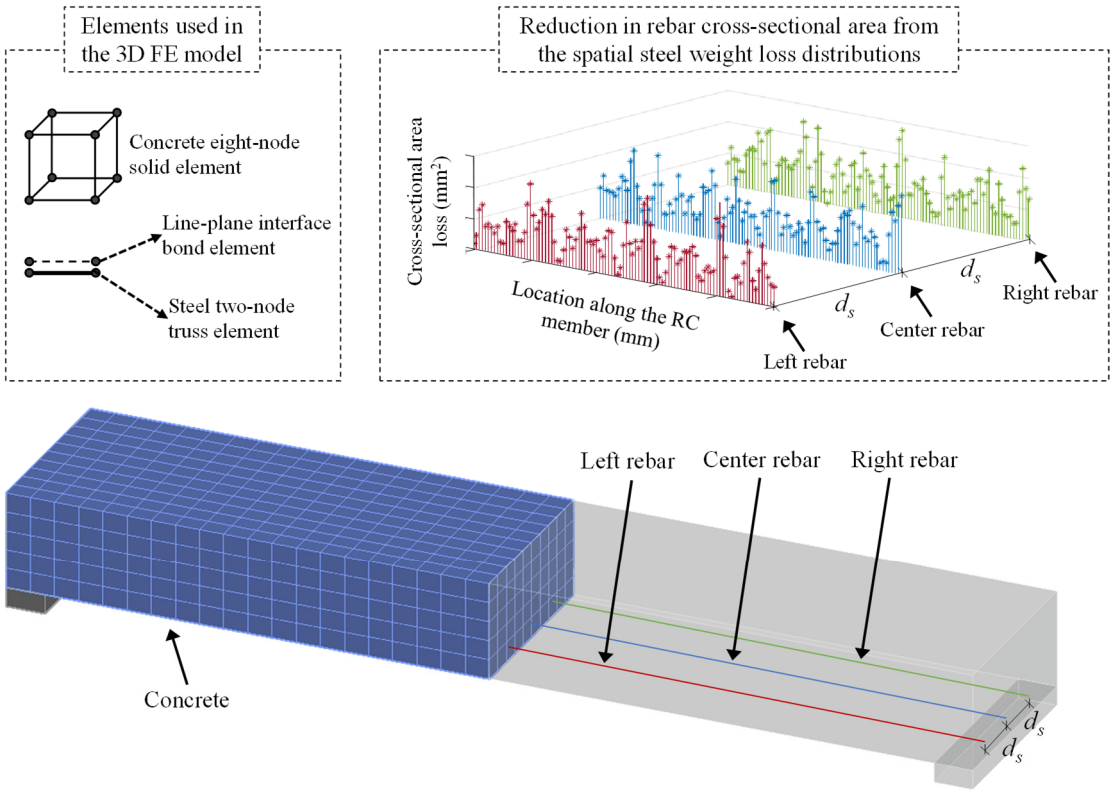

Figure 32 3D FE model considering the reduction in rebar cross-sectional area based on the simulated spatial steel weight loss distributions.

After simulating the spatial steel weight loss distributions of tensile rebars with the SRM, the structural performance of RC structures with the simulated spatial steel weight loss distributions is evaluated using 3D nonlinear FE analysis. Assuming m = 3, the 3D FE

model utilized herein is illustrated in Figure 32. Each tensile rebar is modeled by two-node truss elements with a length of 100 mm, and the spatial steel weight loss distributions simulated in the previous subsection are employed to calculate the average cross-sectional area loss within each tensile rebar element in the FE model.

Eight-node solid elements with dimensions of 100 mm × 100 mm × 100 mm are used for the concrete. The constitutive model of concrete is shown in Figure 33(a), in which the tension-softening and compressive behavior are modeled based on Hordijk [84] and Feenstra [85], respectively. The corrosion-induced damage to the concrete cover is taken into account by modifying the stress-strain relation of the concrete based on the method suggested by Coronelli and Gambarova [86]. For the tensile rebars, the stress-strain relation is modeled based on Shima et al. [87], as shown in Figure 33(b).

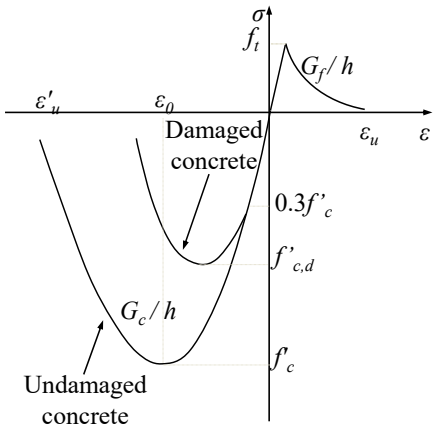

(a) Material constitutive models of concrete

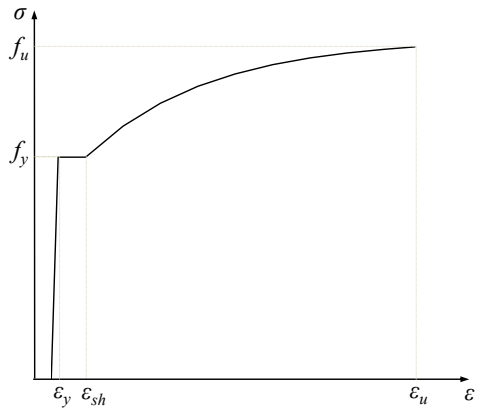

(b) Material constitutive models of tensile rebar

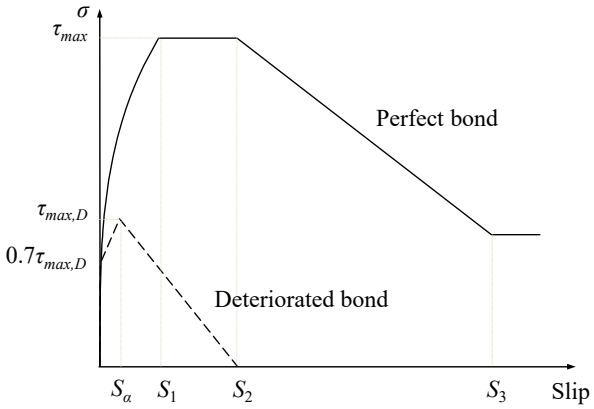

(c) Material constitutive models of bond-slip between concrete and rebar

Figure 33 Material constitutive models in FE analysis: stress-strain relationship of (a) concrete, (b) tensile rebar, and (c) bond-slip between concrete and rebar.

The perfect and deteriorated bond-slip relationships between the concrete and the rebars are modeled using the interface elements proposed by CEB [88] and Kallias and Rafiq [89], respectively, as shown in Figure 33(c). The residual bond-slip relationship can be described as:

$$U = U_1 \left(S/S_1 \right)^{0.3} \tag{54}$$

$$S_{\alpha} = S_1 \left(\alpha' U_{\max} / U_1 \right)^{1/0.3} \tag{55}$$

$$S_{\max} = S_1 \exp\left[(1/0.3) \ln\left(U_{\max,D} / U_1 \right) \right] + S_o \ln\left(U_1 / U_{\max,D} \right) \tag{56}$$

where α'= 0.7, $U_1 = 2.57(f'_c)^{0.5}$, $S_1 = 0.15c_o$ where c_o is the spacing between the ribs of the rebar, $S_2 = 0.35c_o$, and S_o = 0.15 or 0.4 mm for plain concrete or steel confined concrete, respectively. $U_{max,D}$ is the residual bond strength, which can be obtained as [90]:

$$U_{\max,D} = R\left[0.55 + 0.24\left(c / d_b \right) \right] \sqrt{f'_c} + 0.191\left(A_{st} f_{yt} / S_s d_b \right) \tag{57}$$

$$R = A_1 + A_2 m_L \tag{58}$$

where c is the concrete cover, d_b is the diameter of the tensile bar, A_{st} is the cross-sectional area of the stirrup, f_{yt} is the yield strength of the stirrup, S_s is the stirrup spacing; R is the factor accountable for the residual contribution of concrete towards the bond strength, which depends on the corrosion current applied in the accelerated corrosion test and the amount of steel weight loss in percentage (i.e., *MRw* herein) [90]. Eq. (57) composes of two separate terms, which are attributed to the concrete and stirrup contributions to the bond strength, respectively. It is worth noting that the deteriorated bond-slip model for each interface element is calculated based on *MRw* of a corroded RC structure.

Applying 3D nonlinear FE analysis to Monte Carlo simulation (MCS)-based reliability estimation is impractical due to the high computational cost. Hence, to eliminate this limitation, the response surface method (RSM) is incorporated by approximating the relation between the desired output of the FE analysis and the main influencing variables [9, 91, 92]. In the following chapter, the structural reliability estimation of corroded RC girders using a 3D FE model, the RSM and MCS is illustrated as a case study.

Chapter 5: Illustrative Case Study

The effect of the transverse correlation on the simulated steel weight loss distributions of the RC slab specimen has been presented in the previous chapter. Accordingly, to understand how the structural safety is influenced by this parameter, in this chapter the reliability analysis is applied with assumed RC structures in which their steel weight loss distributions are simulated considering the effect of parameters related to the transverse correlation (e.g., the transverse correlation C_3). Then, the results of the failure probabilities for the analyzed RC girders considering the effect of the interaction of corrosion pits among the tensile rebars are compared and discussed comprehensively.

5.1 Description of RC Girders Analyzed

The details of RC girders that contain three and seven tensile rebars are illustrated in Figure 34. Table 5 shows a list of considered cases to investigate the effect of the transverse correlation C_3 among the spatial steel weight loss distributions, the number of tensile rebars m, and spacing between tensile rebars d_s on the reliability of RC girders. The RC girders in Cases A to F have the same total rebar cross-sectional area of 6.16×102 mm2, concrete compressive strength of 40 MPa, and rebar yield strength of 369 MPa. The concrete cover is assumed to be 20 mm.

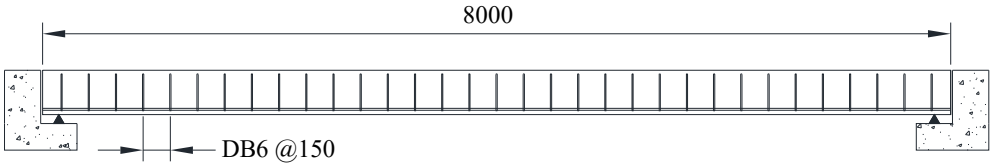

(a) Longitudinal elevation of the analyzed RC girders

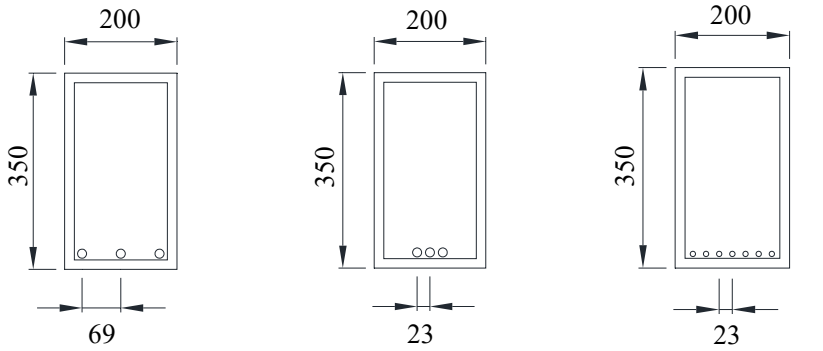

$m = 3$, $d_s = 69$ mm $m = 3$, $d_s = 23$ mm $m = 7$, $d_s = 23$ mm

Total cross-sectional area of tensile rebars in both RC girders: 6.16×10^2 mm^2

(b) Cross-sections of the analyzed RC girders

Figure 34 Details of the analyzed RC girders: (a) longitudinal elevation and (b) cross-sections with different numbers and spacings of tensile rebars (all dimensions are in mm).

Table 5. List of assumed cases.

Case	Number of rebars (= m)	Transverse correlation parameter, C_3	Spacing of tensile rebars, d_s (mm)
A	3	0.005$^+$	69
B	3	0.05*	69
C	3	0.005$^+$	23
D	3	0.05*	23
E	7	0.005$^+$	23
F	7	0.05*	23

$^+$ low transverse correlation

* experimental transverse correlation

5.2 Performance Function

To estimate the structural reliability of the RC girders, the spatial steel weight loss distributions of tensile rebars are simulated using the SRM from *MRw* = 0% to 45%. Additionally, the number of sample realizations is set to 10000 for the simulation. The simulated spatial steel weight loss distributions are then applied in the 3D FE analysis and RSM to estimate the ultimate flexural capacities of the RC girders for each level of *MRw*. The reliability of the RC girders is calculated in the MCS by comparing the ultimate load capacity and load demand:

$$g = P_u - P_s \tag{59}$$

where P_u is the ultimate flexural capacity of corroded RC girders that are subjected to a flexural moment when the concrete ultimate strain reach to 0.0035 and P_s is the load demand, which is assumed herein by Gumbel distribution with the location and scale parameters of 55kN and 4kN, respectively.

The probability of failure $P_f(w)$ at *MRw* = *w* is estimated as follows:

$$P_f(w) = \Pr(g < 0 \,|\, MRw = w) \tag{60}$$

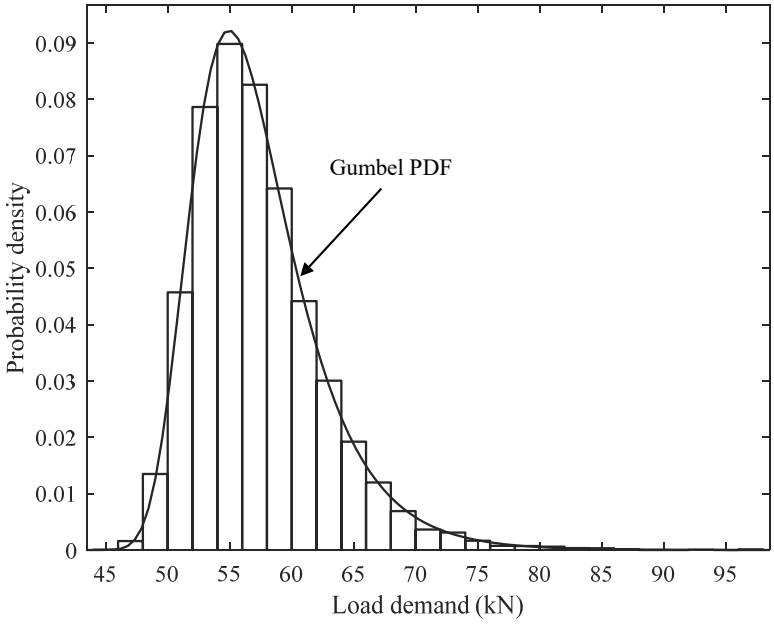

Figure 35 Relative frequency histogram and Gumbel PDF of load demand.

5.3 Validation of the Response Surface Method

To verify the accuracy of the RSM, a 3D FE analysis of the RC girder with seven tensile rebars is performed using a reduced cross-sectional area of the longitudinal rebars based on a series of simulated spatial steel weight loss distributions with *MRw* = 40%. An approximation of the FE analysis output is obtained by a quadratic polynomial function with two-factor interactions as follows:

$$P_u = \alpha_0 + \alpha_1 X_1 + \alpha_2 X_2 + \alpha_3 X_1^2 + \alpha_4 X_2^2 + \alpha_5 X_1 X_2 \tag{61}$$

where P_u is a set of the monitored responses of the ultimate load capacities estimated by the FE analysis, X_1 is the distance from the middle of the RC girder to the location of the concrete ultimate strain, $\varepsilon_{cu}^{'} = 0.0035$; X_2 is the mean value of the local steel weight

losses, $Rw_i(u)$, among all the m rebars at the location of the concrete ultimate strain; and α_ξ ($\xi = 0, 1, 2, \ldots, 5$) are the regression coefficients calculated by the multiple regression analysis.

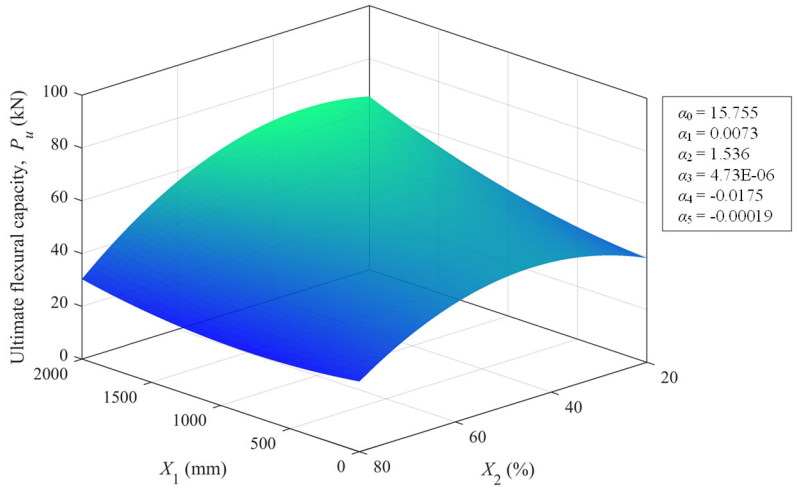

(a) 25 FE models

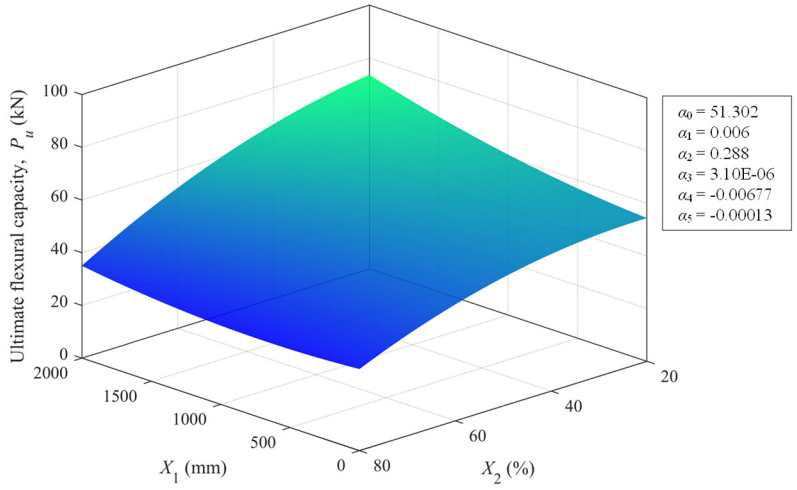

(b) 50 FE models

Figure 36 Effect of the parameters X_1 and X_2 on the ultimate flexural capacity, P_u with the corresponding regression coefficients obtained from (a) 25 FE models and (b) 50 FE models.

Figures 36(a) and (b) present the effect of the parameters X_1 and X_2 on the ultimate flexural capacity, P_u with the corresponding regression coefficients obtained from 25 FE and 50 FE models, respectively. As displayed in Figure 36, the response surfaces of the ultimate flexural capacity, P_u are consistent between both cases (i.e., the RSM with 25 and 50 FE models). Figure 37 presents the relationship between the ultimate flexural capacity obtained directly from 100 FE models and that predicted by the response surface created from 25 and 50 FE models (see Figures 36(a) and (b), respectively). Note that the FE model has a different sample realization of the spatial steel weight loss distributions. As shown in Figure 37, since the results of both cases have similar coefficients of determination ($R^2 \approx 0.65$), the RSM that was previously described with the response surface obtained from 25 FE models (i.e., the 25 sample realizations of the spatial steel weight loss distributions) is utilized to reduce the computational cost.

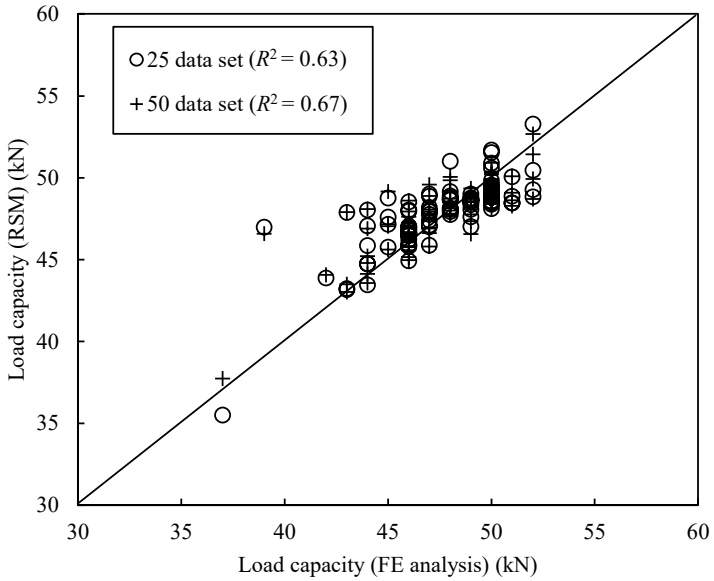

Figure 37 Relationship between the ultimate flexural capacity obtained directly from 100 FE models and that predicted by the response surface created from 25 and 50 FE models.

5.4 Results and Discussion

Figure 38 shows a comparison of the failure probabilities of the analyzed RC girders with three and seven tensile rebars. The failure probabilities of the RC girders with three rebars and seven rebars increase as the transverse correlation parameter C_3 increases (i.e., as the degree of the transverse correlation increases). Moreover, although all the girders analyzed in this case study have the same total cross-sectional area of the tensile rebars, the failure probability of the RC girders increases as the spacing and number of rebars decrease. However, this tendency becomes less obvious as the transverse correlation degree increases.

This finding can be explained by the fact that when the transverse correlation increases and the spacing and number of rebars decrease, the probability of having localized steel weight loss, which generates a particularly weak cross-section for the flexural load capacity of the RC beams, increases, and consequently, the flexural load capacity decreases. As confirmed by the effect of C_3, m and d_s on the histogram of the ultimate flexural capacity P_u with MRw = 35%, as shown in Figures 39, 23, and 41, respectively. The probability densities in the left tail of the histogram for the RC girder with a higher transverse correlation parameter, smaller rebar spacing, and fewer tensile rebars are higher than those for the RC girder with a lower transverse correlation parameter, larger rebar spacing, and more tensile rebars, as shown in Figures 39, 23, and 41, respectively, which leads to a higher failure probability. However, as illustrated in Figures 40 and 41, the left tails in the histograms of P_u for the RC girders with different rebar spacings and different numbers of rebars become likely as the transverse correlation degree increases. Thus, it is important to consider the correlation of steel corrosion not

only in the longitudinal direction but also in the transverse direction when estimating the reliability of corroded RC structures.

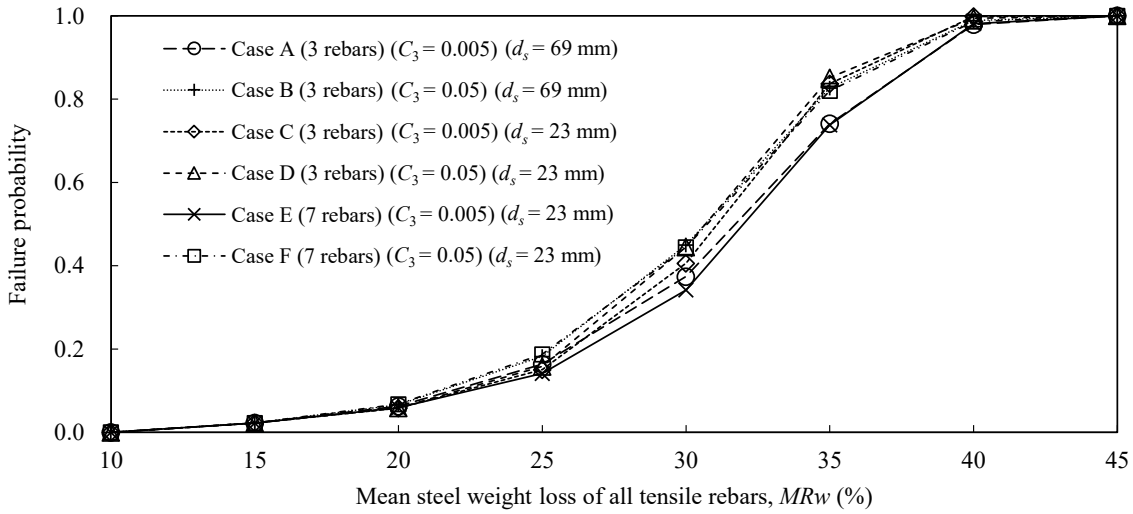

Figure 38 Comparison of the failure probabilities of RC girders with a different number and spacing of tensile rebars.

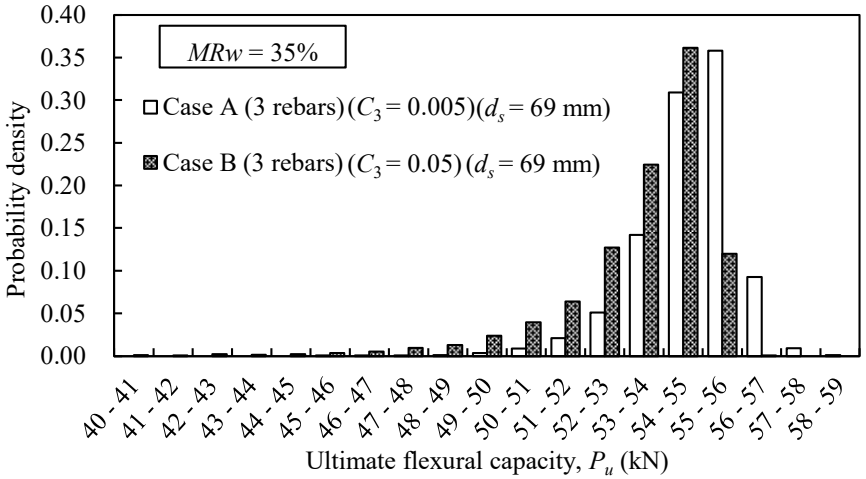

(a) Three rebars and a spacing of 69 mm

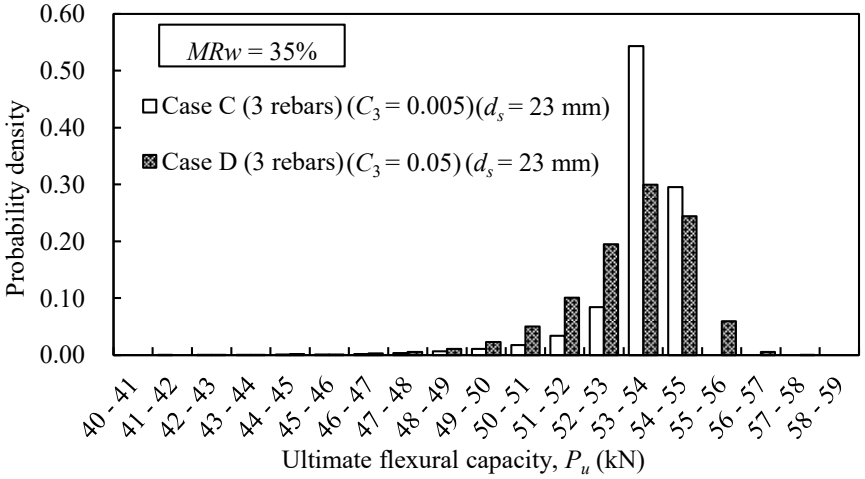

(b) Three rebars and a spacing of 23 mm

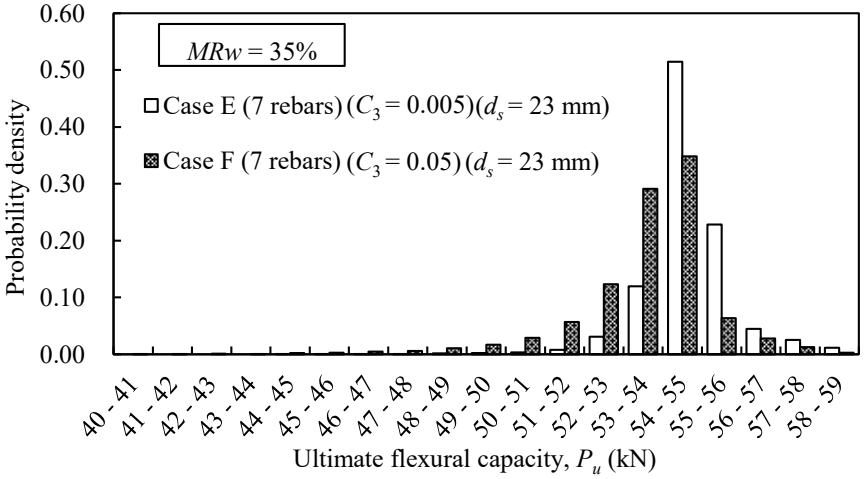

(c) Seven rebars and a spacing of 23 mm

Figure 39 Effect of the transverse correlation parameter C_3 on the histogram of the ultimate flexural capacity P_u for the RC girders when MRw = 35%: (a) three rebars with a spacing of 69 mm, (b) three rebars with a spacing of 23 mm, and (c) seven rebars with a spacing of 23 mm.

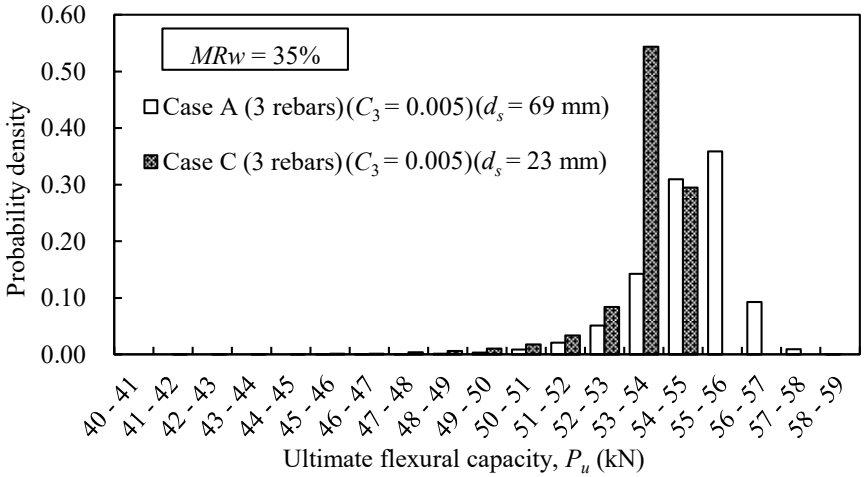

(a) Low transverse correlation (C_3 = 0.005)

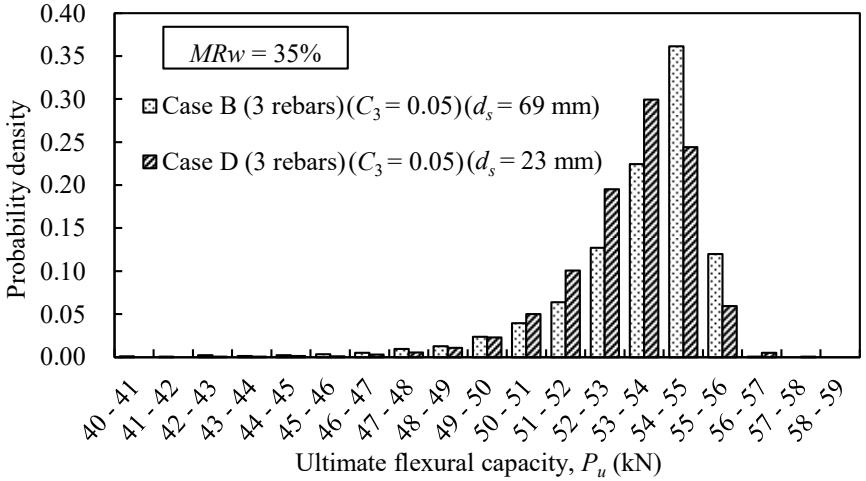

(b) Experimental transverse correlation (C3 = 0.05).

Figure 40 Effect of the spacing of tensile rebars d_s on the histogram of ultimate flexural capacity P_u for the RC girders when MRw = 35%: (a) low transverse correlation (C_3 = 0.005) and (b) experimental transverse correlation (C_3 = 0.05).

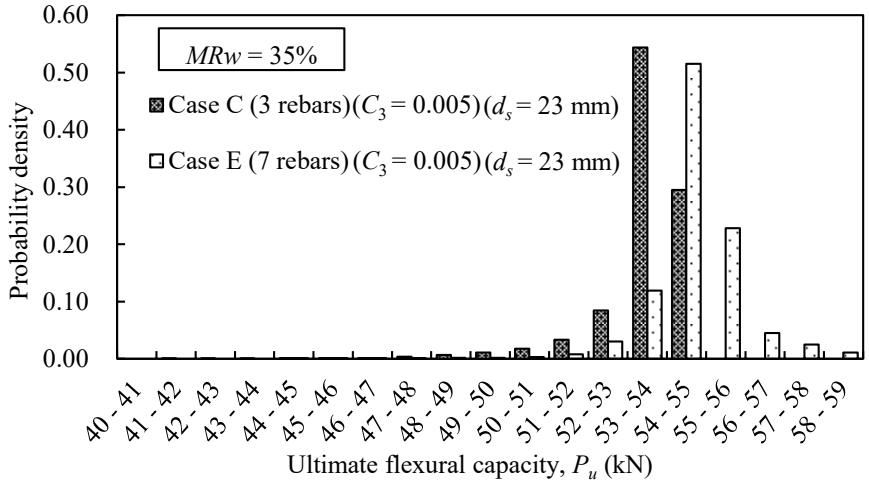

(a) Low transverse correlation (C_3 = 0.005)

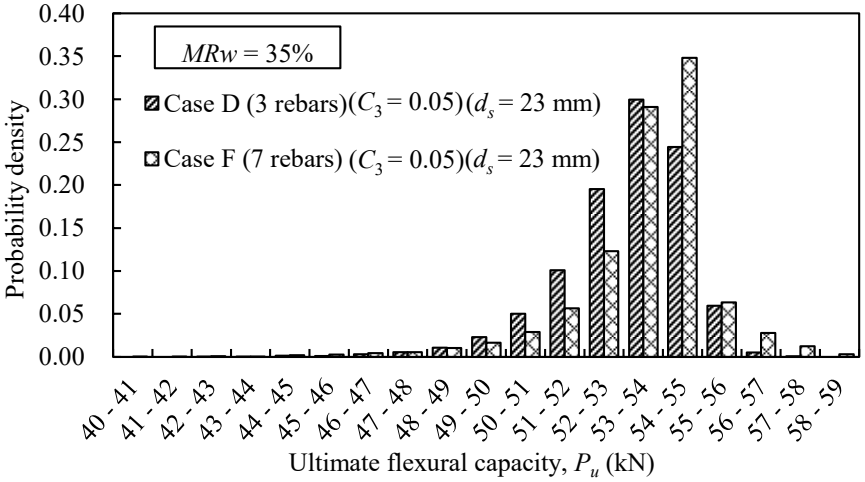

(b) Experimental transverse correlation (C_3 = 0.05)

Figure 41 Effect of the number of tensile rebars on the histogram of ultimate flexural capacity P_u for the RC girders when *MRw* = 35%: (a) low transverse correlation (C_3 = 0.005) and (b) experimental transverse correlation (C_3 = 0.05).

Chapter 6: Conclusions and Future Works

6.1 Conclusions

(1) The results of the spatial steel weight losses in the multiple tensile rebars of the corroded RC slab specimen measured with the X-ray and digital image processing techniques reveal that similar *Rw* profiles were obtained among the tensile rebars for all the corrosion levels; therefore, the effect of the correlation of steel weight loss among the rebars in the transverse direction should be considered when performing simulations.

(2) A procedure for simulating the spatial steel weight loss distributions of multiple tensile rebars in MV random fields was proposed. In this procedure, the functional auto-SDF and functional coherence function are estimated from measured results to consider the correlation of steel weight loss in the longitudinal direction and transverse direction, respectively. In this dissertation, the longitudinal correlation parameters $C_1 = 0.0063$ and $C_2 = 5.7$ and the transverse correlation parameter $C_3 = 0.05$ were obtained. In the numerical example, the *Rw* profiles of the spatial steel weight loss distributions simulated by the proposed procedure show how the strength of the transverse correlation depends on the value of parameter C_3.

(3) The simulated spatial steel weight loss distributions were simultaneously applied in MCS that incorporates 3D FE analysis and the RSM to estimate the reliability of corroded RC structures considering the effect of the interaction of corrosion pits among tensile rebars.

(4) The results of the case study show that the failure probabilities of the RC girders

increase as the transverse correlation degree increases and the number and spacing of the tensile rebars decrease. This is because when the transverse correlation increases and the spacing and number of rebars decrease, the probability of having localized steel weight loss, which generates a particularly weak cross section for the flexural load capacity of RC beams, increases, and consequently, the flexural load capacity decreases (i.e., higher failure probability). However, the effect of the number and spacing of tensile rebars on the failure probability likely becomes less significant as the transverse correlation strengthens. These results suggest that the transverse correlation among the spatial steel weight loss distributions of multiple tensile rebars must be considered when estimating the failure probabilities of RC girders.

6.2 Recommendations for Future Works

This dissertation is the first to propose a procedure for simulating spatial steel weight loss distributions of multiple tensile rebars RC members considering the effect of the spatial variability not only in the longitudinal direction but also in the transverse direction. Thus, it is possible to improve the efficiency of synthesizing the dataset of steel corrosion distributions used for building a machine learning model to predict the deterioration state of corroded RC members [49].

Since it has been reported that the steel corrosion in RC members is both non-uniformly distributed along a rebar length [23] and around rebar cross-sections [93]. However, the effect of non-uniform corrosion around any cross-sections for a rebar on the structural safety of RC members is not addressed herein. In the future, therefore, more works should contribute to this issue experimentally and numerically.

Since the effects of the transverse correlation among the tensile rebars must be

considered in structural performance assessment, further experimental research is needed to investigate the spatial distributions of the steel corrosion of RC members with different concrete qualities, rebar diameters, and distances between the rebars and concrete cover and observe how they depend on the corrosion level. The key technology for understanding the correlation of steel corrosion among longitudinal rebars is X-ray imaging because it enables the continuous observation of the steel corrosion in RC members nondestructively. In addition, life-cycle maintenance and optimization of RC structures must be performed by considering the longitudinal and transverse correlations associated with material deterioration [94–96].

References

[1] Herrmann, A.W., Asce 2013 report card for america's infrastructure, IABSE Symp. Rep. 99 (2013) 9–10.

[2] Koch, G.H., Brongers, M.P.H., Thompson, N.G., Virmani, Y.P. and Payer, J.H., Corrosion cost and preventive strategies in the United States, (2002).

[3] Zhu, W., François, R., Zhang, C. and Zhang, D., Propagation of corrosion-induced cracks of the RC beam exposed to marine environment under sustained load for a period of 26 years, Cem. Concr. Res. 103 (2018) 66–76. doi:10.1016/J.CEMCONRES.2017.09.014.

[4] Frangopol, D.M., Lin, K.-Y. and Estes, A.C., Reliability of Reinforced Concrete Girders under Corrosion Attack, J. Struct. Eng. 123 (1997) 286–297. doi:10.1061/(ASCE)0733-9445(1997)123:3(286).

[5] Enright, M.P. and Frangopol, D.M., Probabilistic analysis of resistance degradation of reinforced concrete bridge beams under corrosion, Eng. Struct. 20 (1998) 960–971. doi:10.1016/S0141-0296(97)00190-9.

[6] Matsuzaki, H., Akiyama, M., Ohki, F., Nakajima, K. and Suzuki, M., A method for structural reliability analysis of concrete beams under marine environment over lifetime and its application to pre tensioned PC beams, J. JSCE. 66 (2010) 147–165. doi:10.2208/jsceje.66.147.

[7] Akiyama, M., Frangopol, D.M. and Suzuki, M., Integration of the effects of airborne chlorides into reliability-based durability design of reinforced concrete structures in a marine environment, Struct. Infrastruct. Eng. 8 (2012) 125–134. doi:10.1080/15732470903363313.

[8] Frangopol, D.M. and Soliman, M., Life-cycle of structural systems: recent achievements and future directions, Struct. Infrastruct. Eng. 12 (2016) 1–20. doi:10.1080/15732479.2014.999794.

[9] Frangopol, D.M., Dong, Y. and Sabatino, S., Bridge life-cycle performance and cost: analysis, prediction, optimisation and decision-making, Struct. Infrastruct. Eng. 13 (2017) 1239–1257. doi:10.1080/15732479.2016.1267772.

[10] Akiyama, M., Frangopol, D.M. and Ishibashi, H., Toward life-cycle reliability-, risk- and resilience-based design and assessment of bridges and bridge networks under independent and interacting hazards: emphasis on earthquake, tsunami and corrosion, Struct. Infrastruct. Eng. 16 (2020) 26–50. doi:10.1080/15732479.2019.1604770.

[11] Marsh, P.S. and Frangopol, D.M., Reinforced concrete bridge deck reliability model incorporating temporal and spatial variations of probabilistic corrosion rate sensor data, Reliab. Eng. Syst. Saf. 93 (2008) 394–409. doi:10.1016/j.ress.2006.12.011.

[12] Stewart, M.G., Spatial variability of pitting corrosion and its influence on structural fragility and reliability of RC beams in flexure, Struct. Saf. 26 (2004) 453–470. doi:10.1016/J.STRUSAFE.2004.03.002.

[13] Zhu, W. and François, R., Corrosion of the reinforcement and its influence on the residual structural performance of a 26-year-old corroded RC beam, Constr. Build. Mater. 51 (2014) 461–472. doi:10.1016/j.conbuildmat.2013.11.015.

[14] Castel, A., François, R. and Arliguie, G., Mechanical behaviour of corroded reinforced concrete beams - Part 1: experimental study of corroded beams, Mater. Struct. Constr. 33 (2000) 539–544. doi:10.1007/bf02480533.

[15] Castel, A., François, R. and Arliguie, G., Mechanical behaviour of corroded reinforced concrete beams - Part 2: bond and notch effects, Mater. Struct. Constr. 33 (2000) 545–551. doi:10.1007/bf02480534.

[16] Stewart, M.G. and Al-Harthy, A., Pitting corrosion and structural reliability of corroding RC structures: Experimental data and probabilistic analysis, Reliab. Eng. Syst. Saf. 93 (2008) 373–382. doi:10.1016/J.RESS.2006.12.013.

[17] Zhang, M., Song, H., Lim, S., Akiyama, M. and Frangopol, D.M., Reliability estimation of corroded RC structures based on spatial variability using experimental evidence, probabilistic analysis and finite element method, Eng. Struct. 192 (2019) 30–52. doi:10.1016/J.ENGSTRUCT.2019.04.085.

[18] Vu, K.A. and Stewart, M.G., Predicting the likelihood and extent of reinforced concrete corrosion-induced cracking, J. Struct. Eng. 131 (2005) 1681–1689. doi:10.1061/(ASCE)0733-9445(2005)131:11(1681).

[19] Papakonstantinou, K.G. and Shinozuka, M., Probabilistic model for steel corrosion in reinforced concrete structures of large dimensions considering crack effects, Eng. Struct. 57 (2013) 306–326. doi:10.1016/J.ENGSTRUCT.2013.06.038.

[20] Na, U.J., Kwon, S.-J., Chaudhuri, R. and Shinozuka, M., Stochastic Model for Service Life Prediction of RC Structures Exposed to Carbonation using Random Field Simulation, KSCE J. Civ. Eng. 16 (2012) 133–143. doi:10.1007/s12205-012-1248-7.

[21] Kioumarsi, M., Hendriks, M. and Geiker, M.R., Quantification of the interference of localised corrosion on adjacent reinforcement bars in a concrete beam in bending, Nord. Concr. Res. 49 (2014) 39–57. https://www.researchgate.net/publication/283123508 (accessed November 7,

2019).

[22] Kioumarsi, M.M., Hendriks, M.A.N., Kohler, J. and Geiker, M.R., The effect of interference of corrosion pits on the failure probability of a reinforced concrete beam, Eng. Struct. 114 (2016) 113–121. doi:10.1016/j.engstruct.2016.01.058.

[23] Lim, S., Akiyama, M. and Frangopol, D.M., Assessment of the structural performance of corrosion-affected RC members based on experimental study and probabilistic modeling, Eng. Struct. 127 (2016) 189–205. doi:10.1016/J.ENGSTRUCT.2016.08.040.

[24] Lim, S., Akiyama, M., Frangopol, D.M. and Jiang, H., Experimental investigation of the spatial variability of the steel weight loss and corrosion cracking of reinforced concrete members: novel X-ray and digital image processing techniques, Struct. Infrastruct. Eng. 13 (2017) 118–134. doi:10.1080/15732479.2016.1198397.

[25] Bertolini, L., Steel corrosion and service life of reinforced concrete structures, Struct. Infrastruct. Eng. 4 (2008) 123–137. doi:10.1080/15732470601155490.

[26] Jaffer, S.J. and Hansson, C.M., Chloride-induced corrosion products of steel in cracked-concrete subjected to different loading conditions, Cem. Concr. Res. 39 (2009) 116–125. doi:10.1016/J.CEMCONRES.2008.11.001.

[27] Lin, H., Zhao, Y., Feng, P., Ye, H., Ozbolt, J., Jiang, C. and Yang, J.Q., State-of-the-art review on the bond properties of corroded reinforcing steel bar, Constr. Build. Mater. 213 (2019) 216–233. doi:10.1016/J.CONBUILDMAT.2019.04.077.

[28] Mangat, P.S. and Elgarf, M.S., Flexural Strength of Concrete Beams with Corroding Reinforcement, Struct. J. 96 (1999) 149–158. doi:10.14359/606.

[29] Torres-Acosta, A.A. and Martı´nez-Madrid, M., Residual Life of Corroding Reinforced Concrete Structures in Marine Environment, J. Mater. Civ. Eng. 15

(2003) 344–353. doi:10.1061/(ASCE)0899-1561(2003)15:4(344).

[30] Castel, A., François, R. and Arliguie, G., Mechanical behaviour of corroded reinforced concrete beams—Part 1: Experimental study of corroded beams, Mater. Struct. 2000 339. 33 (2000) 539–544. doi:10.1007/BF02480533.

[31] El Maaddawy, T., Soudki, K. and Topper, T., Long-term performance of corrosion-damaged reinforced concrete beams, ACI Struct. J. 102 (2005) 649.

[32] Kashani, M.M., Maddocks, J. and Dizaj, E.A., Residual Capacity of Corroded Reinforced Concrete Bridge Components: State-of-the-Art Review, J. Bridg. Eng. 24 (2019) 03119001. doi:10.1061/(ASCE)BE.1943-5592.0001429.

[33] Higgins, C. and Farrow III, W.C., Tests of reinforced concrete beams with corrosion-damaged stirrups, ACI Mater. J. 103 (2006) 133.

[34] Hanjari, K.Z., Coronelli, D. and Lundgren, K., Bond capacity of severely corroded bars with corroded stirrups, Mag. Concr. Res. 63 (2011) 953–968. doi:10.1680/MACR.10.00200.

[35] Coronelli, D., Hanjari, K.Z. and Lundgren, K., Severely corroded RC with cover cracking, J. Struct. Eng. 139 (2013) 221–232. doi:10.1061/(ASCE)ST.1943-541X.0000633.

[36] N.T. Build., 492. Concrete, mortar and cement-based repair materials: Chloride migration coefficient from non-steady-state migration experiments, Nord. Method. (1999).

[37] Feng, W., Tarakbay, A., Ali Memon, S., Tang, W. and Cui, H., Methods of accelerating chloride-induced corrosion in steel-reinforced concrete: A comparative review, Constr. Build. Mater. 289 (2021) 123165. doi:10.1016/J.CONBUILDMAT.2021.123165.

[38] Alonso, C., Andrade, C., Rodriguez, J. and Diez, J.M., Factors controlling cracking of concrete affected by reinforcement corrosion, Mater. Struct. Constr. 31 (1996) 435–441. https://link.springer.com/article/10.1007/BF02480466 (accessed May 13, 2020).

[39] Al-Sulaimani, G.J., Kaleemullah, M., Basunbul, I.A. and Rasheeduzzafar, Influence of Corrosion and Cracking on Bond Behavior and Strength of Reinforced Concrete Members, Struct. J. 87 (1990) 220–231. doi:10.14359/2732.

[40] Chen, J., Fu, C., Ye, H. and Jin, X., Corrosion of steel embedded in mortar and concrete under different electrolytic accelerated corrosion methods, Constr. Build. Mater. 241 (2020) 117971. doi:10.1016/J.CONBUILDMAT.2019.117971.

[41] Gu, X., Guo, H., Zhou, B., Zhang, W. and Jiang, C., Corrosion non-uniformity of steel bars and reliability of corroded RC beams, Eng. Struct. 167 (2018) 188–202. doi:10.1016/j.engstruct.2018.04.020.

[42] Li, D., Wei, R., Du, Y., Guan, X. and Zhou, M., Measurement methods of geometrical parameters and amount of corrosion of steel bar, Constr. Build. Mater. 154 (2017) 921–927. doi:10.1016/j.conbuildmat.2017.08.018.

[43] Zahid, H.F., Jiradilok, P., Singh Kuntal, V. and Nagai, K., Investigation of the effects of multiple and multi-directional reinforcement on corrosion-induced concrete cracking pattern, Constr. Build. Mater. 283 (2021) 122594. doi:10.1016/j.conbuildmat.2021.122594.

[44] Mori, Y., Ellingwood, B.R., Yasuhiro MorP, B., Ellingwood, B.R., Mori, Y. and Ellingwood, B.R., Reliability-based service-life assessment of aging concrete structures, J. Struct. Eng. 119 (1993) 1600–1621. doi:10.1061/(ASCE)0733-9445(1993)119:5(1600).

[45] Stewart, M.G. and Rosowsky, D. V., Time-dependent reliability of deteriorating reinforced concrete bridge decks, Struct. Saf. 20 (1998) 91–109. doi:10.1016/S0167-4730(97)00021-0.

[46] Enright, M.P. and Frangopol, D.M., Reliability-based condition assessment of deteriorating concrete bridges considering load redistribution, Struct. Saf. 21 (1999) 159–195. doi:10.1016/S0167-4730(99)00015-6.

[47] Stewart, M.G. and Mullard, J.A., Spatial time-dependent reliability analysis of corrosion damage and the timing of first repair for RC structures, Eng. Struct. 29 (2007) 1457–1464. doi:10.1016/J.ENGSTRUCT.2006.09.004.

[48] Zhang, M., Nishiya, N., Akiyama, M., Lim, S. and Masuda, K., Effect of the correlation of steel corrosion in the transverse direction between tensile rebars on the structural performance of RC beams, Constr. Build. Mater. 264 (2020) 120678. doi:10.1016/j.conbuildmat.2020.120678.

[49] Zhang, M., Akiyama, M., Shintani, M., Xin, J. and Frangopol, D.M., Probabilistic estimation of flexural loading capacity of existing RC structures based on observational corrosion-induced crack width distribution using machine learning, Struct. Saf. 91 (2021) 102098. doi:10.1016/j.strusafe.2021.102098.

[50] Ali, A., Lyamin, A. V., Huang, J., Sloan, S.W. and Cassidy, M.J., Undrained stability of a single circular tunnel in spatially variable soil subjected to surcharge loading, Comput. Geotech. 84 (2017) 16–27. doi:10.1016/j.compgeo.2016.11.013.

[51] Tran, T.T. and Kim, D., Uncertainty quantification for nonlinear seismic analysis of cabinet facility in nuclear power plants, Nucl. Eng. Des. 355 (2019) 110309. doi:10.1016/j.nucengdes.2019.110309.

[52] Ma, L., Bocchini, P. and Christou, V., Fragility models of electrical conductors in

power transmission networks subjected to hurricanes, Struct. Saf. 82 (2020) 101890. doi:10.1016/j.strusafe.2019.101890.

[53] Nishiya, N., Fukushima, H., Sakurai, A., Akiyama, M., Bocchini, P. and Frangopol, D.M., Effect of different steel weight loss distributions on the life-cycle reliability of PC girders, in: Maintenance, Safety, Risk, Manag. Life-Cycle Perform. Bridg., CRC Press, 2018: pp. 1001–1006.

[54] Srivaranun, S., Masuda, K., Akiyama, M. and Frangopol, D.M., Time-Dependent Structural Performance Analysis of RC Slab Exposed to Chloride Attack by Incorporating Spatial Variability, in: 13th Int. Conf. Appl. Stat. Probab. Civ. Eng., Seoul, South Korea, 2019.

[55] Chen, E.J., Ding, L., Liu, Y., Ma, X. and Skibniewski, M.J., On spectral representation method and Karhunen–Loève expansion in modelling construction material properties, Arch. Civ. Mech. Eng. 18 (2018) 768–783. doi:10.1016/j.acme.2017.12.008.

[56] Wu, Y.C. and Zhi, P., Reliability assessment of RAC chloride concentration using Karhunen–Loève expansion with digital-image kernels, Constr. Build. Mater. 245 (2020) 118352. doi:10.1016/j.conbuildmat.2020.118352.

[57] Fan, H. and Liang, R., Reliability-based design of axially loaded drilled shafts using Monte Carlo method, Int. J. Numer. Anal. Methods Geomech. 37 (2013) 2223–2238. doi:10.1002/nag.2131.

[58] Fenton, G.A. and Vanmarcke, E.H., Simulation of Random Fields via Local Average Subdivision, J. Eng. Mech. 116 (1990) 1733–1749. doi:10.1061/(asce)0733-9399(1990)116:8(1733).

[59] De Vasconcellos Real, M., Campos Filho, A. and Maestrini, S.R., Response

variability in reinforced concrete structures with uncertain geometrical and material properties, Nucl. Eng. Des. (2003). doi:10.1016/S0029-5493(03)00110-9.

[60] Gioffrè, M., Gusella, V. and Grigoriu, M., Simulation of non-Gaussian field applied to wind pressure fluctuations, Probabilistic Eng. Mech. 15 (2000) 339–345. doi:10.1016/S0266-8920(99)00035-1.

[61] Bocchini, P., Probabilistic approaches in civil engineering: generation of random fields and structural identification with genetic algorithms, alma, 2008.

[62] Shinozuka, M. and Jan, C.M., Digital simulation of random processes and its applications, J. Sound Vib. 25 (1972) 111–128. doi:10.1016/0022-460X(72)90600-1.

[63] Shinozuka, M. and Deodatis, G., Simulation of stochastic processes by spectral representation, Appl. Mech. Rev. 44 (1991) 191–204. doi:10.1115/1.3119501.

[64] Shinozuka, M. and Deodatis, G., Simulation of Multi-Dimensional Gaussian Stochastic Fields by Spectral Representation, Appl. Mech. Rev. 49 (1996) 29. doi:10.1115/1.3101883.

[65] Deodatis, G., Simulation of ergodic multivariate stochastic processes, J. Eng. Mech. 122 (1996) 778–787. doi:10.1061/(ASCE)0733-9399(1996)122:8(778).

[66] Yamazaki, F. and Shinozuka, M., Digital generation of non-Gaussian stochastic fields, J. Eng. Mech. 114 (1988) 1183–1197. doi:10.1061/(ASCE)0733-9399(1988)114:7(1183).

[67] Grigoriu, M., Crossings of non-Gaussian translation processes, J. Eng. Mech. 110 (1984) 610–620. doi:10.1061/(ASCE)0733-9399(1984)110:4(610).

[68] Grigoriu, M. and Harper, E., Applied non-Gaussian processes: Examples, theory, simulation, linear random vibration, and MATLAB solutions, (1995).

[69] Deodatis, G. and Micaletti, R.C., Simulation of highly skewed non-Gaussian stochastic processes, J. Eng. Mech. 127 (2001) 1284–1295. doi:10.1061/(ASCE)0733-9399(2001)127:12(1284).

[70] Shi, Y., Deodatis, G. and Koutsourelakis, P., A novel approach for simulation of non-Gaussian fields: application in estimating wire strengths from experimental data, (2004).

[71] Shields, M.D.D., Deodatis, G. and Bocchini, P., A simple and efficient methodology to approximate a general non-Gaussian stationary stochastic process by a translation process, Probabilistic Eng. Mech. 26 (2011) 511–519. doi:10.1016/J.PROBENGMECH.2011.04.003.

[72] Christou, V. and Bocchini, P., An Efficient Methodology That Simulates a Multi-Dimensional Non-Gaussian Field to Evaluate the Effect of the Spatial Distribution of Corrosion in a Steel Beam, in: Struct. Congr. 2014, American Society of Civil Engineers, Reston, VA, 2014: pp. 1059–1069. doi:10.1061/9780784413357.094.

[73] Bocchini, P. and Frangopol, D.M., A stochastic computational framework for the joint transportation network fragility analysis and traffic flow distribution under extreme events, Probabilistic Eng. Mech. 26 (2011) 182–193. doi:10.1016/j.probengmech.2010.11.007.

[74] Popescu, R., Deodatis, G. and Prevost, J.H., Simulation of homogeneous nonGaussian stochastic vector fields, Probabilistic Eng. Mech. 13 (1998) 1–13. doi:10.1016/s0266-8920(97)00001-5.

[75] Shields, M.D. and Deodatis, G., A simple and efficient methodology to approximate a general non-Gaussian stationary stochastic vector process by a translation process with applications in wind velocity simulation, Probabilistic Eng.

Mech. 31 (2013) 19–29. doi:10.1016/j.probengmech.2012.10.003.

[76] Zhang, W., Zhou, B., Gu, X. and Dai, H., Probability distribution model for cross-sectional area of corroded reinforcing steel bars, J. Mater. Civ. Eng. 26 (2014) 822–832. doi:10.1061/(ASCE)MT.1943-5533.0000888.

[77] Jiang, H., Ji, H., Jin, N., Tian, Y., Jin, X., Ye, H., Yan, D. and Tian, Z., Simulation and experimental verification of the non-uniform corrosion cracking process of reinforced mortar specimen, Constr. Build. Mater. 265 (2020) 120522. doi:10.1016/j.conbuildmat.2020.120522.

[78] Gao, X., Pan, Y. and Ren, X., Probabilistic model of the minimum effective cross-section area of non-uniform corroded steel bars, Constr. Build. Mater. 216 (2019) 227–238. doi:10.1016/j.conbuildmat.2019.05.012.

[79] Kashani, M.M., Crewe, A.J. and Alexander, N.A., Use of a 3D optical measurement technique for stochastic corrosion pattern analysis of reinforcing bars subjected to accelerated corrosion, Corros. Sci. 73 (2013) 208–221. doi:10.1016/j.corsci.2013.03.037.

[80] Shafei, B. and Alipour, A., Application of large-scale non-Gaussian stochastic fields for the study of corrosion-induced structural deterioration, Eng. Struct. 88 (2015) 262–276. doi:10.1016/j.engstruct.2014.12.024.

[81] Agarwal, M. and Mehra, R., Review of matrix decomposition techniques for signal processing applications, Int. J. Eng. Res. Appl. 4 (2014) 90–93.

[82] Yang, D., Peterson, G.D., Li, H. and Sun, J., An FPGA implementation for solving least square problem, in: Proc. - IEEE Symp. F. Program. Cust. Comput. Mach. FCCM 2009, 2009: pp. 303–306. doi:10.1109/FCCM.2009.47.

[83] Bendat, J.S. and Piersol, A.G., Random data: analysis and measurement procedures,

729 (2011).

[84] Hordijk, D.A., Local Approach to Fatigue of Concrete, Doctor dissertation, Delft Univ. Technol. (1991).

[85] Feenstra, P.H., Computational aspects of biaxial stress in plain and reinforced concrete, 1993.

[86] Coronelli, D. and Gambarova, P., Structural assessment of corroded reinforced concrete beams: modeling guidelines, J. Struct. Eng. 130 (2004) 1214–1224. doi:10.1061/(ASCE)0733-9445(2004)130:8(1214).

[87] Shima, H., Chou, L.-L. and Okamura, H., Micro and macro models for bond in reinforced concrete, J. Fac. Eng. Univ. Tokyo. 39 (1987) 133–194.

[88] CEB, CEB-FIP Model Code 1990, CEB Bull. d'Information. 213 (1993).

[89] Kallias, A.N. and Rafiq, M.I., Finite element investigation of the structural response of corroded RC beams, Eng. Struct. 32 (2010) 2984–2994. doi:10.1016/j.engstruct.2010.05.017.

[90] El Maaddawy, T., Soudki, K. and Topper, T., Analytical model to predict nonlinear flexural behavior of corroded reinforced concrete beams, ACI Struct. J. 102 (2005) 550. https://www.researchgate.net/publication/256484211 (accessed January 28, 2022).

[91] Liu, W.D., Neuenhoffer, A., Ghosn, M., Moses, F., TRB, Liu, W.D., Neuenhoffer, A., Ghosn, M. and Moses, F., Redundancy in highway bridge substructures, Washington D.C., 2000.

[92] Kallias, A.N. and Imran Rafiq, M., Performance assessment of corroding RC beams using response surface methodology, Eng. Struct. 49 (2013) 671–685. doi:10.1016/j.engstruct.2012.11.015.

[93] Yuan, Y. and Ji, Y., Modeling corroded section configuration of steel bar in concrete structure, Constr. Build. Mater. 23 (2009) 2461–2466.

[94] Akiyama, M., Frangopol, D.M. and Yoshida, I., Time-dependent reliability analysis of existing RC structures in a marine environment using hazard associated with airborne chlorides, Eng. Struct. 32 (2010) 3768–3779. doi:10.1016/J.ENGSTRUCT.2010.08.021.

[95] Frangopol, D.M. and Liu, M., Maintenance and management of civil infrastructure based on condition, safety, optimization, and life-cycle cost, Struct. Infrastruct. Eng. 3 (2007) 29–41. doi:10.1080/15732470500253164.

[96] Marsh, P.S. and Frangopol, D.M., Lifetime Multiobjective Optimization of Cost and Spacing of Corrosion Rate Sensors Embedded in a Deteriorating Reinforced Concrete Bridge Deck, J. Struct. Eng. 133 (2007) 777–787. doi:10.1061/(asce)0733-9445(2007)133:6(777).

List of Published Papers

Academic Journals:

Supasit Srivaranun, Mitsuyoshi Akiyama, Paolo Bocchini, Vasileios Christou, Dan M. Frangopol, Hiroyuki Fukushima, and Keisuke Masuda, Effect of the interaction of corrosion pits among multiple tensile rebars on the reliability of RC structures: Experimental and numerical investigation, Structural Safety, Vol. 93, 102115, 2021, doi:10.1016/j.strusafe.2021.102115

Supasit Srivaranun, Mitsuyoshi Akiyama, Keisuke Masuda, Dan M. Frangopol, and Osamu Maruyama, Random field-based reliability updating framework for existing RC structures incorporating the effect of spatial steel corrosion distribution, Structure and Infrastructure Engineering, 2021, doi:10.1080/15732479.2021.1995445

Zheng-Shu He, **Supasit Srivaranun**, Mitsuyoshi Akiyama, and Dan M. Frangopol, Life-cycle reliability-based design and reliability updating of reinforced concrete shield tunnels in coastal regions, Structure and Infrastructure Engineering, Vol. 16, No. 4, pp. 726-737, 2020, doi:10.1080/15732479.2021.1887291

Conference Papers:

Supasit Srivaranun, Mitsuyoshi Akiyama, Paolo Bocchini, Vasileios Christou and Dan M. Frangopol, Probabilistic Load-Carrying Capacity Estimation of RC Structures Considering the Interaction of Corrosion Pits among Tensile Rebars, Proceeding of the 13th International Conference on Structural Safety & Reliability (ICOSSAR 2021-2022), Shanghai, China, 2022. (in application)

Supasit Srivaranun, Keisuke Masuda, Mitsuyoshi Akiyama, Dan M. Frangopol, and Osamu Maruyama, Life-cycle reliability estimation of deteriorating RC structures by stochastic interpolation of spatial random fields, Proceeding of the 7th

International Symposium on Life-Cycle Civil Engineering (IALCCE2020), pp.140-145, Shanghai, China, 2021.

Supasit Srivaranun, Keisuke Masuda, Sopokhem Lim, Mitsuyoshi Akiyama, Dan M. Frangopol, Osamu Maruyama, Application of observational data in reliability estimation of aging RC bridge structures considering spatial steel corrosion distribution. 10th International Conference on Bridge Maintenance, Safety and Management (IABMAS 2020), pp.1044-1049, Hokkaido, Japan, 2021.

Keisuke Masuda, **Supasit Srivaranun**, Mitsuyoshi Akiyama, Updating the reliability of existing RC structures in a marine environment incorporating spatial variations. Proceeding of the 16th East Asia-Pacific Conference on Structural Engineering & Construction (EASEC16), pp 1283-1288, Brisbane, Australia, 2021.

Supasit Srivaranun, Keisuke Masuda, Mitsuyoshi Akiyama, Nonlinear finite element analysis of aging RC slabs represented by the stochastic field, The Ninth Japan Conference on Structural Safety and Reliability (JCOSSAR 2019), pp.29-30, Tokyo, Japan, 2019.

Supasit Srivaranun, Keisuke Masuda, Mitsuyoshi Akiyama, and Dan M. Frangopol, Time-dependent structural performance analysis of RC slab exposed to chloride attack by incorporating spatial variability, 13th International Conference on Applications of Statistics and Probability in Civil Engineering (ICASP13), Seoul, South Korea, 2019.